Development of novel oxidation responsive T_2 MRI contrast agents based on molecular magnets encapsulated in a polysulfide nanocarrier

A thesis submitted to the University of Manchester for the degree of

Doctor of Philosophy

in the Faculty of Medical and Human Sciences

Damien Jeanmaire

Manchester Pharmacy School

2014

Contents

Word Count: 34,277

5 List of figures

6 List of Schemes

7 List of tables

8 List of abbreviations

^{1}H	proton
β-CD	b-cyclodextrin
CA	contrast agent
CMC	critical micelle concentration
CPMG	Carr-Purcell-Meilboom-Gill
D	diffusion coefficient
DBU	1,8-diazabicyclo[5,4,0]undec-7-ene
DCM	dichloromethane
DLS	dynamic light scattering
DOSY	diffusion ordered spectroscopy
DOTA	1,4,7,10-tetraazacyclododecane-1,4,7,10-tetraacetic acid
DP	degree of polymerisation
DTPA	Gadopentetic acid
EH	2-ethylhexanoic acid
emf	electromotive force
EPR	electron paramagnetic resonance
EPR	enhanced permeability and retention effect
FBS	foetal bovine serum
fid	free induction decay

FT-IR	Fourier transform infra-red
γ	gyromagnetic ratio
Γ	decay rate
GPC	gel permeation chromatography
GSH	glutathione
GSSG	glutathione disulfide
$\hbar$	reduced Plank's constant
H_2O_2	hydrogen peroxide
HAS	human serum albunin
k_B	Boltzmann's constant
MRI	magnetic resonance imaging
MWCO	molecular weight cut-off
NAD	nicotinamide adenine dinucleotide
NMR	nuclear magnetic resonance
NSF	nephrogenic systemic fibrosis
OCl^-	hypochlorite
PA_4	pentaerythritol tetraacrylate
PBS	phosphate buffer saline
PEG	polyethylene glycol
piv	pivalic acid
PPG	polypropylene glycol
PPS	poly(propylene sulfide)

PS	propylene sulfide
r.f.	radio frequency
r_2	transverse relaxivity
RES	reticuloendothelian system
R_h	hydrodynamic radius
ROS	reactive oxygen species
Sal	3,5-diisopropylsalicylic acid
SMM	single molecule magnet
SPION	superparamagnetic iron oxide nanoparticles
T_1	longitudinal relaxation time
T_2	Transverse relaxation time
TE	echo time
TEA	triethylamine
TEM	transmission electron microscopy
THF	tetrahydrofuran
UV	ultra-violet
Vis	visible

9 Abstract

Development of novel oxidation responsive T_2 MRI contrast agents based on molecular magnets encapsulated in a polysulfide nanocarrier

The University of Manchester
Damien Jeanmaire
Doctor of Philosophy
2014

In this thesis, we propose the development of an oxidation responsive T_2 contrast agent based on oxidation sensitive poly(propylene sulfide) (PPS) nanoparticles and molecular magnet heterometallic rings. PPS nanoparticles show an oxidation responsive character in the presence of Reactive Oxygen Species (ROS), typically found in inflammatory conditions in the body.

We have shown that PPS nanoparticles can be synthesised with a controlled hydrodynamic size and degree of polymerisation. Upon oxidation with different ROS, in particular hydrogen peroxide (H_2O_2) and hypochlorite (OCl^-), the hydrophobic polysulfide network experiences oxidation to poly-sulfoxides/-sulfones, causing a shift in polarity and ingress of water, resulting in particle swelling. The oxidation of the nanoparticles was monitored by dynamic light scattering (DLS) as well as diffusion ordered spectroscopy (DOSY).

The polysulfide nanoparticles were then loaded with molecular magnets (heterometallic rings Cr_7Ni and $Cr_{12}Gd_4$) using a co-solvent method. It was found that the loading did not significantly change the physical or chemical properties of either the PPS nanoparticles or the molecular magnets. However the composition and outer functionalization of the molecular magnets has an effect on both their loading efficiency and their T_2 relaxivity. The nanoparticles' effect on water proton transvers relaxation was measured before and after oxidation with small amounts of H_2O_2. The loaded nanoparticles exhibit a binary 'off/on' switch effect when exposed to small amounts of hydrogen peroxide. Independent of oxidant concentration, the oxidised nanoparticles increase the relaxivity rate of water protons when compared to their reduced state.

10 Declaration and copyright statement

No portion of the work referred to in the thesis has been submitted in support of an application for another degree or qualification of this or any other university or other institute of learning.

Note on copyright and the ownership of intellectual property right:

i. The author of this thesis (including any appendices and/or schedules to this thesis) owns certain copyright or related rights in it (the “Copyright”) and s/he has given The University of Manchester certain rights to use such Copyright, including for administrative purposes.

ii. Copies of this thesis, either in full or in extracts and whether in hard or electronic copy, may be made only in accordance with the Copyright, Designs and Patents Act 1988 (as amended) and regulations issued under it or, where appropriate, in accordance with licensing agreements which the University has from time to time. This page must form part of any such copies made.

iii. The ownership of certain Copyright, patents, designs, trademarks and other intellectual property (the “Intellectual Property”) and any reproductions of copyright works in the thesis, for example graphs and tables (“Reproductions”), which may be described in this thesis, may not be owned by the author and may be owned by third parties. Such Intellectual Property and Reproductions cannot and must not be made available for use without the prior written permission of the owner(s) of the relevant Intellectual Property and/or Reproductions.

iv. Further information on the conditions under which disclosure, publication and commercialisation of this thesis, the Copyright and any Intellectual Property and/or Reproductions described in it may take place is available in the University IP Policy (see http://documents.manchester.ac.uk/DocuInfo.aspx?DocID=487), in any relevant Thesis restriction declarations deposited in the University Library, The University Library’s regulations (see http://www.manchester.ac.uk/library/aboutus/regulations) and in The University’s policy on Presentation of Theses.

1 Introduction

1.1 Magnetic resonance imaging (MRI)

Magnetic resonance imaging (MRI) is a modern imaging technique which provides powerful diagnosis tools for medical diagnosis and treatment as well as biomedical research[1]. MRI is primarily used for imaging the body as it can obtain high quality, sub-millimeter resolution images of tissue deep inside the body.

MRI is based on the phenomenon of nuclear magnetic resonance (NMR). This is the mechanism by which the magnetic moments of nuclei can interact with radio frequency (r.f.) magnetic pulses, when in a static magnetic field. This interaction is dependent on both the magnetic properties of the nuclei as well as the magnetic field in which the nuclei are placed. In MRI, it is the ^{1}H nucleus which is usually observed. The ^{1}H nucleus contains only one proton and has a spin of I=1/2. This, along with its high abundance in the body in the form of fat and water makes it the ideal element in the body to image via MRI.

MRI provides images based on the spatial distribution of water protons or contrast agents throughout the body. The signal intensity depends both on the concentration of the water molecules and their relaxivity. To understand how this works, the basic theory of NMR must be covered.

1.1.1 Theory of nuclear magnetic resonance (NMR)

The quantum mechanical property which is utilised for NMR is spin. Nucleon (protons and neutrons) have an intrinsic property called spin, noted I. Spin is an important parameter which characterises the energy state of the particle. In nuclei, particles with like spins pair against each other to create an average spin of I=0. For magnetic resonance to occur in a nucleus it must have a non-zero spin, therefore it must have an odd mass number. In this case, the ^{1}H nucleus is of interest. This contains one proton, hence has an intrinsic spin I=1/2.

Using quantum mechanics theory, a nucleus with spin I has 2I+1 possible energy states. In the case of the hydrogen nucleus, two different states are possible. When no magnetic field is applied to the system, the nuclei will be evenly split between the two different states which have the same energy. When a magnetic field is applied, there is a splitting of the two states into two energy levels. Each level is described by a magnetic quantum number, m. In the case of the ^{1}H nucleus, these states will be m=+1/2, which is parallel to the applied magnetic field and has a lower energy, and m=-1/2 which is anti-parallel to the applied magnetic field and has a higher energy (Figure 1.1-1).

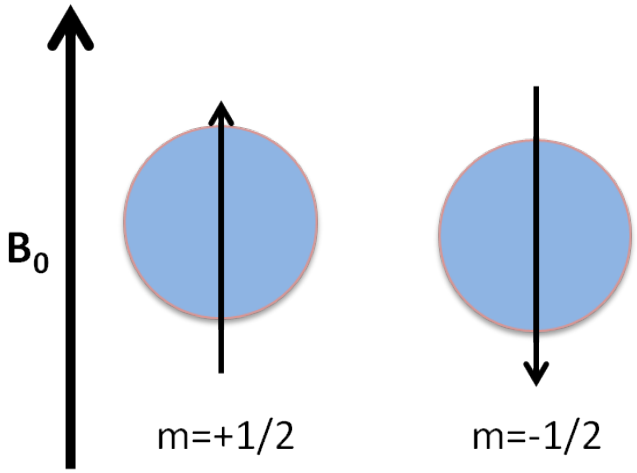

Figure 1.1-1 The two lowest energy states of nuclei in a static external magnetic field.

When a magnetic field is applied, the nuclei are split between the two possible energy states following the Boltzmann distribution.

$$\frac{n_{upper}}{n_{lower}} = e^{-\frac{\Delta E}{k_B T}} \qquad \textbf{Equation 1.1-1}$$

Where n_{upper} and n_{lower} are the number of nuclei in the upper or lower state respectively, k_B is the Boltzmann constant, T is the temperature and ΔE is the energy difference between the two states.

$$\Delta E = \mathrm{E_{m1}} - \mathrm{E_{m2}} = -\gamma\hbar\left(+\frac{1}{2}\right)\mathrm{B} + \gamma\hbar\left(-\frac{1}{2}\right)\mathrm{B} \qquad \textbf{Equation 1.1-2}$$

$$\Delta E = \gamma\hbar B \qquad \textbf{Equation 1.1-3}$$

Where B is the applied magnetic field and γ is the gyromagnetic ratio, a fundamental magnetic constant which is dependent on the nucleus. In the case where B = 3.0 T, the ratio n_{upper} / n_{lower} = 0.999, this shows that there are slightly more nuclei in the lower level than in the upper level leading to a net magnetisation in the direction of the applied magnetic field (+z direction). However, as the excess is very small, a pulse of electromagnetic radiation is able to flip the excess spins and alter the net magnetization.

In order to interact with the nuclei, the pulse must be at the resonant frequency of the nuclei. This resonance frequency, ω, is defined as,

$$\omega = \frac{|E_1 - E_2|}{\hbar} = \frac{\Delta E}{\hbar}$$ **Equation 1.1-4**

where E_1 and E_2 are the lower and upper energy states respectively. Combining Equation 1.1-3 and Equation 1.1-4 **,** gives,

$$\omega = \frac{\Delta E}{\hbar} = \gamma B$$ **Equation 1.1-5**

With typical magnetic fields of between 1-3 T, the resonant frequency is usually located in the radio frequency part of the electromagnetic spectrum.

In the case of ^{1}H, the gyromagnetic ratio, γ, is 2.675×10^{8} $s^{-1}T^{-1}$, and the corresponding resonant frequency at a magnetic field of 1T is 42.573 MHz.

1.1.2 Movement of magnetic moments

When an external static magnetic field B_0, is applied to the system along the +z-axis, the magnetic moments μ will precess about B_0 with a net magnetisation in the +z direction. They precess on the surface of a cone at the Larmor Frequency, $\omega_0 = \gamma B_0$ (Figure 1.1-1).

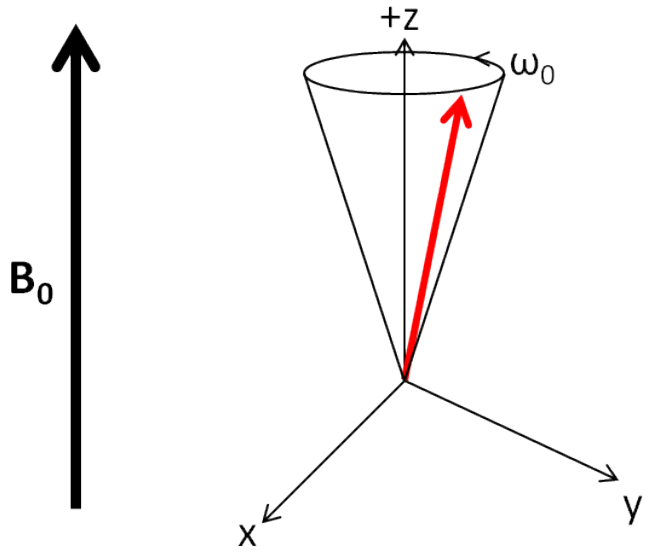

Figure 1.1-2 Precession of magnetic moments around the +z axis at the Larmor frequency.

When an r.f. field B_1, perpendicular to B_0 generated by an oscillating magnetic field, is applied to the system, the net magnetisation moves to the x-y plane. The magnetic moments will then start to precess about B_0 in the transverse x-y plane; this is known as a 90 degree pulse. In the case where B_1 is along the -z axis, the magnetic moments will precess about $-B_0$ this is a 180° pulse (Figure 1.1-3).

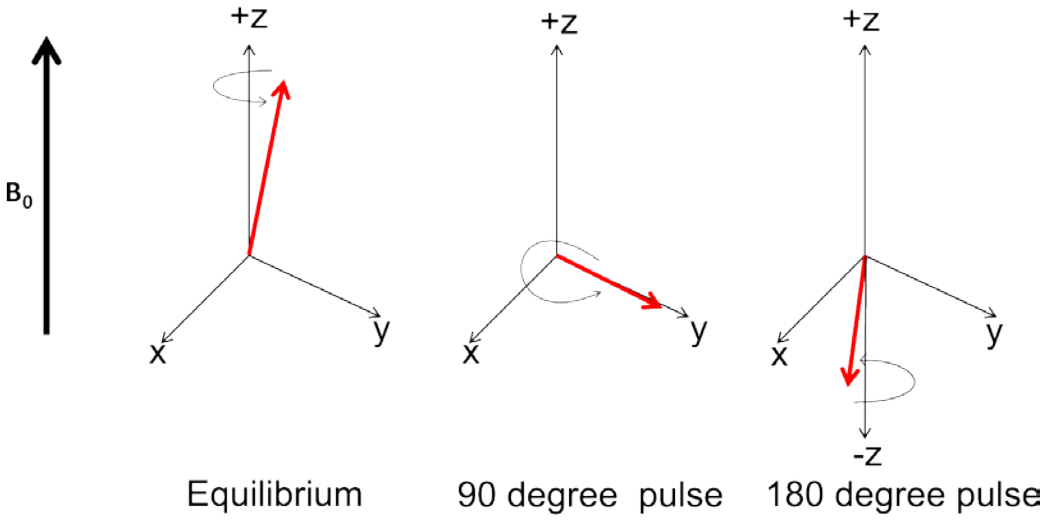

Figure 1.1-3 Nuclear magnetic moments precessing: in equilibrium (left), after a 90° pulse (middle), and after a 180° pulse (right).

Following this excitation from the r.f. pulse, the magnetisation of the sample will relax back to its original state where the net magnetisation is aligned with the external static magnetic field B_0. This relaxation process follows two different paths, one is controlled by thermal interactions the other with internuclear interactions, called spin-lattice and spin-spin relaxation respectively. These relaxations can be described independently by the Bloch model[2].

1.1.3 Spin-lattice relaxation

Spin-lattice (T_1) relaxation describes the relaxation which occurs as the nuclear spins re-align themselves with the static magnetic field B_0 along the +z axis. When the r.f. field is removed, energy from the excited spins is dissipated into the surrounding lattice causing the relaxation of the longitudinal magnetisation M_z, and reducing the energy of the system back to its minimum energy equilibrium state (Figure 1.1-4).

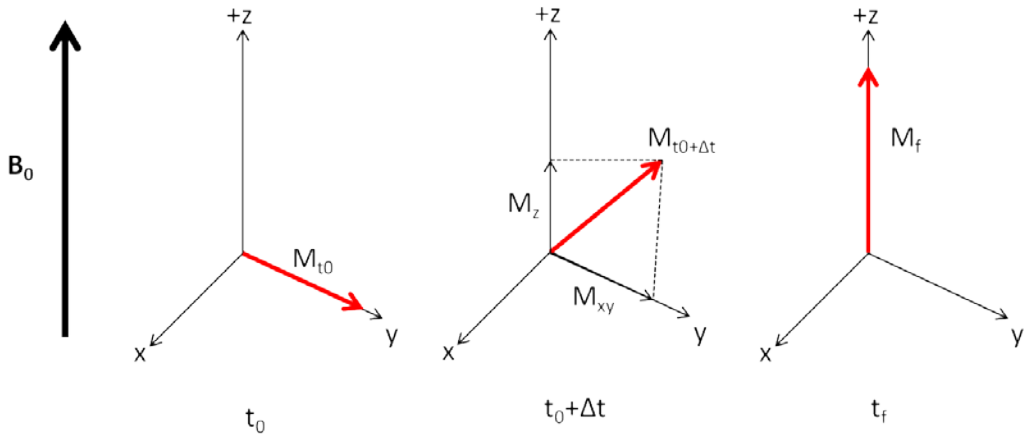

Figure 1.1-4 Spin-lattice relaxation of magnetic moments after a 90° pulse.

The relaxation of M_z is governed by the following equation,

$$\frac{dM_z}{dt} = \frac{M_0 - M_z}{T_1} \qquad \textbf{Equation 1.1-6}$$

Where M_0 is the initial magnetization after the r.f. pulse and T_1 is the spin-lattice relaxation time. A solution to this equation is an exponential with time constant T_1, which describes the recovery of M back to its equilibrium state (Figure 1.1-5). T_1 represents the time it takes for 63% of the magnetisation signal to be recovered. This relaxation process is also known as T_1 relaxation[2].

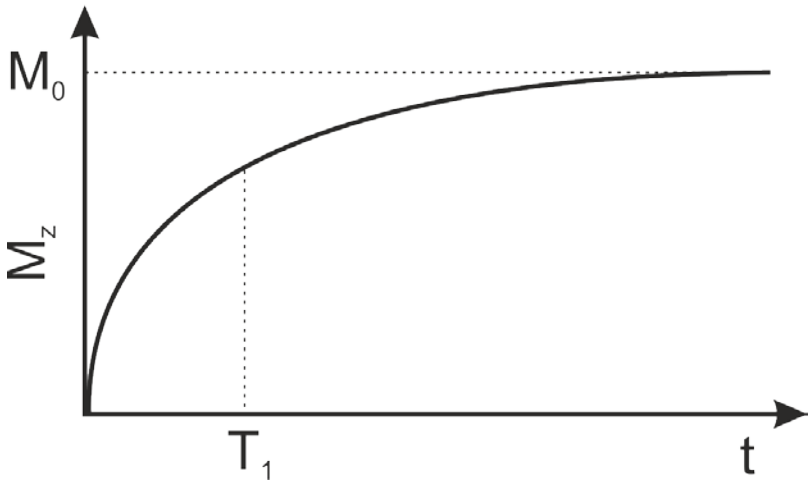

Figure 1.1-5 Exponential T_1 relaxation of the M_z component of the magnetic moment.

1.1.4 Spin-spin relaxation

In a system where a uniform static magnetic field is applied and nuclear spins are precessing, it would be expected that these magnetic moments would all precess with identical Larmor frequencies as only one magnetic field is being applied. However, this is not the case; interactions between nuclei create very small magnetic fields which locally perturb the magnetic fields around individual nuclei. This causes a change in the Larmor frequency of each nucleus and causes a dephasing of the magnetic moments. This results in a net transverse magnetisation (M_{xy}) of zero.

When a 90 degree pulse is applied to a system of nuclei, the nuclear spins find themselves precessing about the z axis in the x-y plane. When the external field is removed, the inter nuclei interactions immediately begin to dephase the transverse magnetisation(Figure 1.1-6). Simultaneously, T_1 relaxation is also occuring, realigning the spins in the direction of the static magnetic field B_0. The relaxation times T_1 and T_2 are a function of the nuclei properties, the experimental environment and the strength of the external magnetic field. In general, $T_1 > T_2$[3]. The equation governing these relaxations are called the Bloch equations.

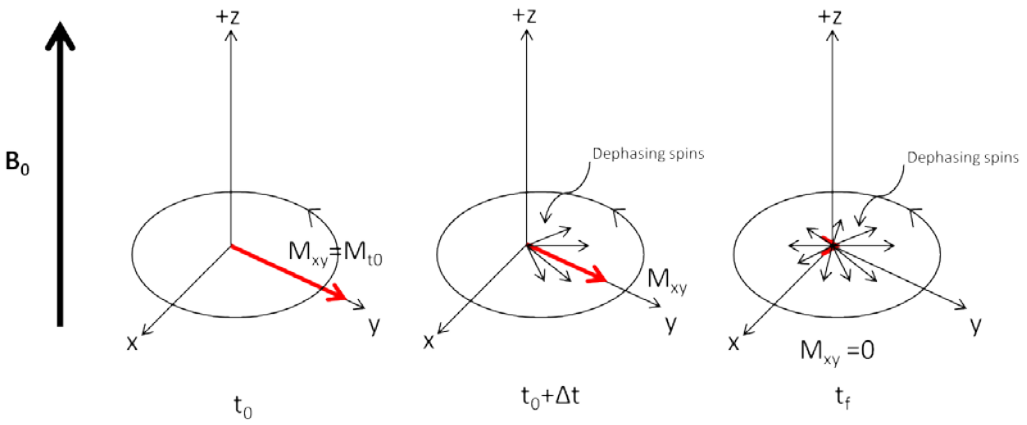

Figure 1.1-6 Spin-spin relaxation of magnetic moments in the xy plane.

This dephasing is called spin-spin relaxation and occurs in a characteristic time T_2. Spin-spin relaxation is governed by a decaying exponential,

$$M_{xy}(t) = M_{xy}(0)e^{-i\omega_0 t/T_2} \qquad \textbf{Equation 1.1-7}$$

Where $M_{xy}(0)$ is the initial value of M_{xy}. The terms in the exponential describe both the phase change in the rotational motion of the transverse magnetisation as well as the T_2 decay of the transverse magnetisation.

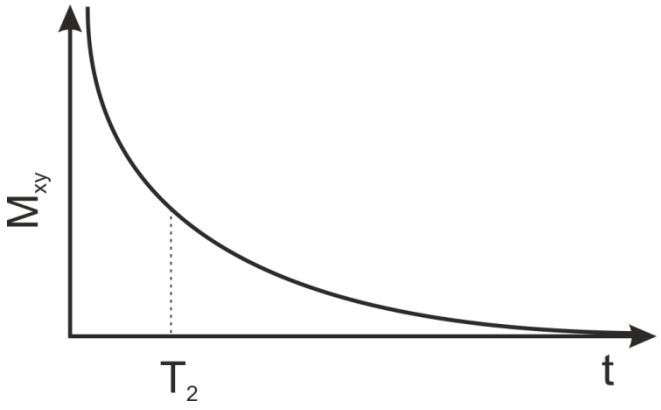

Figure 1.1-7 Exponential T_2 relaxation of the M_{xy} component of the magnetic moment.

1.1.5 T_2* decay

As previously mentioned, T_2 relaxation is due to internuclear, dipole, interactions; however, in practice the magnetisation of a material is very heterogeneous. This is due to a combination of varying internal magnetic susceptibilities and inhomogeneities in the external magnetic field. These differences throughout the volume of the media create a Larmor frequency and

phase of precession with spatial dependency. This change in the Larmor frequency and phase causes the net transverse magnetisation to decay much faster than in simple T_2 relaxation. This decay time is characterised by the time constant T_2* and is a combination of T_2 relaxivity and T_2', a time constant linked to the inhomogeneity of the external magnetic field.

$$\frac{1}{T_2^*} = \frac{1}{T_2} + \frac{1}{T_2'} \qquad \textbf{Equation 1.1-8}$$

1.1.6 Acquiring an NMR signal

Signal acquisition in an NMR experiment is achieved by placing a receiving coil next to the sample. Following the application of an r.f. pulse on the sample, the magnetic moments inside the sample will gradually relax and realign themselves with the static external field B_0. This in turn will induce a voltage in the receiving coil. This voltage is called an electromotive force, *emf* and is dependent on the r.f. pulse as well as the static magnetic field. The signal generated by this force is called the *free induction decay* (FID) and is proportional to both the Larmor frequency and the initial magnetisation in the sample[4].

This signal is then Fourier transformed into the frequency domain and converted into the well-known NMR spectra.

1.1.7 Forming an image using MRI

When using nuclear magnetic resonance to image a volume, it is necessary to segment the volume into slices and selectively image each slice. In order to achieve this, only the nuclei in the desired slice must be excited in a fashion that they will emit an NMR signal. In an MRI this is done by applying magnetic field gradients. The gradient fields are used to create small perturbations in the magnetic field along the direction of the main magnetic field B_0. In order to image in all three dimensions, the gradients must be able to be applied in all three dimensions separately, x, y and z. When a gradient is applied, the magnetic field at position r_i is defined as,

$$B_i = B_0 + G_T r_i \qquad \textbf{Equation 1.1-9}$$

where G_T is the total gradient amplitude. As expected, in the presence of these gradient fields, the Larmor frequency of the nuclei will also be spatially dependent.

$$\omega_i = \gamma(B_0 + G_T r_i)$$ **Equation 1.1-10**

To obtain an image from a slice, r.f. pulsed, gradient pulses and data acquisition periods are arranged together into what is called a pulse sequence.

There are three separate steps when imaging a slice with MRI; these are slice selection, phase encoding and frequency encoding.

The first step of slice selection is the selective excitation of nuclei in a slice of the body. As mentioned previously, a gradient pulse will perturb the Larmor frequencies of nuclei as a function of spatial position. In order to select a slice, a specific gradient pulse is applied such that nuclei in a certain area have a Larmor frequency which coincides with the excitation r.f. pulse. This results in only the protons in the selected volume which have a Larmor frequency equal to the r.f. pulse being excited. To control the thickness of the slice, two parameters can be changed, either the gradient field amplitude can be changed or the bandwidth of the r.f. pulse can be changed. These two parameters are linked by the following equation,

$$\Delta\omega_{rf} = \gamma \times \Delta(G_{ss} \times r_i)$$ **Equation 1.1-11**

Where $\Delta\omega_{rf}$ is the bandwidth of the r.f. pulse, G_{ss} is the gradient amplitude and t is the slice thickness (Figure 1-7). In general, $\Delta\omega_{rf}$ is kept constant and the gradient field is changed to select the desired slice thickness. As an MR image is made up of multiple slices, slice selection is done by keeping the gradient field constant and tuning the r.f. pulse to selectively excite nuclei in different areas.

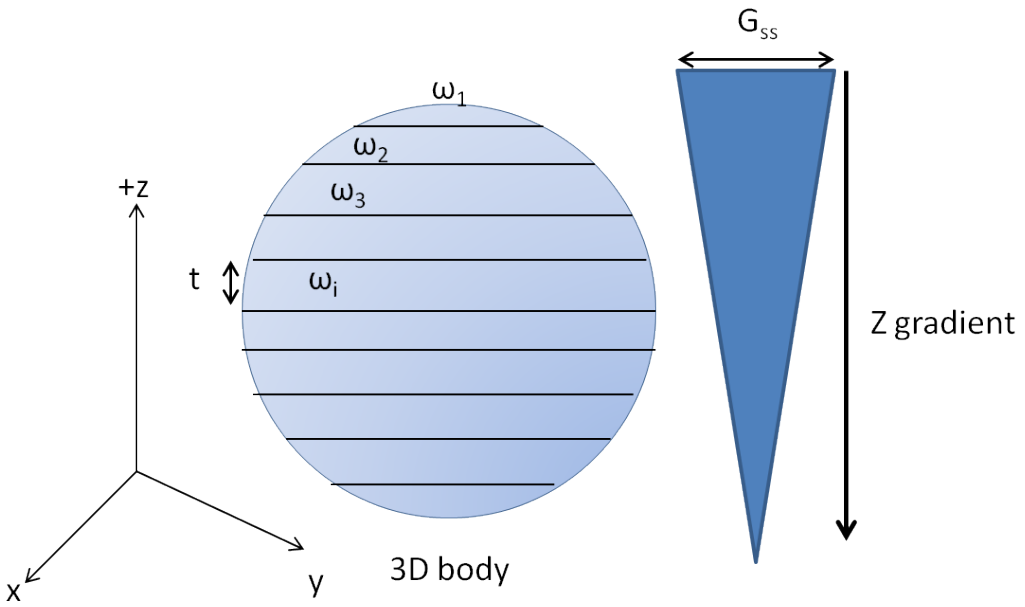

Figure 1.1-8 Magnetic field gradient used to perform slice selection during imaging.

Once the selected slice is excited, it is then necessary to detect the emitted signal and spatially decode the signal in the x and y directions. This is performed using frequency and phase encoding.

Frequency and phase encoding are in effect the opposite of slice selection. Two gradients are used, one in the x direction of the slice and one in the y direction of the slice. In the case of slice selection, a gradient is used to make sure that all the protons in the selected slice have the same Larmor frequency so that they are all excited by the r.f. pulse. In the case of frequency and phase encoding, the two gradients perturb the excited nuclei, which are now precessing the the transverse plane, and change their frequency as a function of position along the gradient. This is done in both the x and y directions. When the signal is acquired through the pickup coils, the spread in frequency can be deconvoluted from the applied field gradients, hence resulting in a 2d image[2].

1.2 Contrast in MRI

1.2.1 Endogenous contrast in MRI

In an MR image, the contrast between two areas of an image, or two tissues A and B, is defined as,

$$C(A,B) = \frac{|I_A - I_B|}{I_{ref}}$$ **Equation 1.2-12**

Where I_A and I_B are the signal intensities of regions A and B respectively, and I_{ref} is the arbitrary reference intensity[5]. In a simple MR image, I_{ref} does not exist and therefore the contrast is just the difference of intensities between the two tissues.

1.2.2 T_1 weighted contrast

T_1 weighted images are obtained by varying the repetition time between successive excitation pulses. When a pulse is applied to the system, nuclei will relax through T_1 relaxation. A nucleus with a short T_1 relaxation will relax quickly and emit a large signal when re-excited with the following r.f. pulse. On the other hand, if the nucleus has a long T_1 relaxation, its relaxation will be very little between two successive r.f. pulses. The lack of full signal recovery before the next pulse results in a low signal intensity for the following pulse. To control the contrast between areas in the body with high T_1 and low T_1 relaxivity, the repetition time can be changed. If the repetition time is very long, all nuclei will have a chance to relax into the ground state between the pulses resulting in little contrast. If the repetition time is very short, only those areas with fast T_1 relaxivity will show large signal intensity.

This can be seen when imaging the body; contrast between water and fat is obtained via T_1 imaging. For a short pulse repetition time, fat, which has a short T_1, shows up as bright spots on an image, whereas water with a long T_1 shows up as dark patches. Table 1.2-1 shows the T_1 and T_2 relaxation times of common tissues in the body.

Table 1.2-1 Table of T_1 and T_2 relaxation times of different tissues in the body[6].

Tissue	T_2 – 3T (ms)	T_1 – 3T (ms)
Cartilage	36.9 ± 3.8 [6]	1240 ± 107 [6]
Skeletal Muscle	31.7 ± 1.9 [6]	1420 ± 38 [6]
Subcutaneous fat	133 ± 6 [6]	371 ± 8 [6]

1.2.3 T_2 weighted contrast

Obtaining images with T_2 is possible by altering the time between the excitation pulse and the echo recovery. The echo recovery is the signal which is obtained after 'refocusing' the magnetic moments following a dephasing. When the 90 degree r.f. pulse is applied, the spins drop down into the x-y plane. They then start to dephase as a function of their T_2 relaxation rates. To refocus the spins, a 180 degree pulse is applied and the spins re-join in the x-y plane. The signal is then measured as an echo. The time between the 90 degree pulse and the echo is called the echo time, TE. By varying this time, T_2 weighted contrast images can be obtained. In general a long TE is used for T_2 imaging. In this case nuclei with short T_2 relaxivity, such as fat, will result in low signal intensity, whereas nuclei with a long T_2 relaxivity, such as water, will have a large signal intensity.

1.3 MRI contrast agents

Unfortunately, the sensitivity of MRI is inherently low due to the small energetic difference between spin states at these magnetic fields (Zeeman splitting). In order to increase the signal intensities, and allow this technique to be viable for diagnostics, contrast agents are generally required. Contrast agents are used to shorten the magnetic relaxation times of their local environment, increasing the contrast between healthy and diseased tissue resulting in an increase in sensitivity and accuracy of MRI.

This is achieved by introducing local magnetic inhomogeneities in the area of interest, creating non-uniform relaxation rates due to the interaction between the proton spins and the electron spins of the contrast agent.

Although all contrast agents affect both T_1 and T_2 relaxation rates, they are usually developed and optimised to shorten either T_1 or T_2 relaxation times of surrounding water protons.

1.3.1 T_1 contrast agents

T_1 contrast agents, also known as ‘positive’ contrast agents, create an increase in MRI signal intensity (bright contrast) of their local environment on a T_1 weighted image. The most common magnetic compounds used as T_1 contrast agents are

stable gadolinium ion based complexes. These typically consist of one Gd^{3+} ion an organic chelating ligand and one or two available water bonding sites[7]. Gadolinium, located in the middle of the lanthanide series, has seven unpaired electrons due to its half-filled 4f shell and therefore has a large magnetic moment and long electronic relaxation times (9-10 s). This slow relaxation enables these compounds to enhance their local relaxation rate. However, free Gd^{3+} ions are very toxic to the body, intercepting and disrupting Ca^{2+} signalling, it is therefore necessary to chelate these ions with organic ligands. Inert Gd complexes are usually formed using poly(amino carboxylates) as chelating ligands. After forming the complex, typically, one or two coordination sites are left open to allow for water binding. This is important for a highly efficient T_1 contrast agent as the inner sphere interaction is where the Gd ion will have its greatest effect on surrounding water[8].

The efficiency of a T_1 contrast agent is characterised by its r_1 relaxivity – the change in longitudinal relaxation rate as a function of contrast agent concentration.

$$\frac{1}{T_{1,obs}} = \frac{1}{T_{1,d}} + r_1[Gd^{3+}] \qquad \textbf{Equation 1.3-13}$$

Where $1/T_{1,obs}$ and $1/T_{1,d}$ are the T_1 relaxation rates with and without contrast agent, respectively[9].

Typical chelates used for Gd based CAs are diethylene triamine pentaacetic acid (DTPA) (Magnevist®) and 1,4,7,10-tetraazacyclododecane-1,4,7,10-tetraacetic acid (DOTA) (Dotarem®), both used in clinical imaging. They are typically blood-pool agents, signifying that they freely circulate in the blood stream without a specific targeting or activation mechanism. These are used to detect breakages in the vascularity system, typically in the blood brain barrier. They can also be used to monitor blood flow dynamics and perfusion[10]. These have r_2 relaxivities of around 3-4 $mM^{-1}s^{-1}$. [11]

1.3.2 T_2 contrast agents

T_2 contrast agents, also known as 'negative' contrast agents, increase the T_2 relaxation rate of surrounding hydrogen nuclei causing a darkening effect on the scan image. Unlike T_1 CAs, T_2 CAs operate solely through dipole-dipole interactions, there is no direct binding or magnetic exchange between the contrast media and the water molecules. The high magnetic moment of the compounds induce a large magnetic field which perturbs the magnetic relaxation rate of surrounding water protons, shortening of the spin-spin relaxation time of the protons. This high magnetic moment also means that less material is required to achieve sufficient contrast. This is a major advantage over Gd based contrast agents as a lower dose means less potentially toxic material is injected into the body. This greatly reduces the possibility of any complications. In addition, the materials used in T_2 contrast agents are less toxic than for T_1 contrast agents.

The majority of T_2 CA are based on superparamagnetic iron oxide nanoparticles (SPIONs). They were first proposed as a CA in 1986 by Mendonca Dias et al. for imaging the liver and spleen[12]. This is due to their lack of toxicity, biodegradability and chemical stability[13-14]. In addition, the nanoparticle form of T_2 contrast agents allows for much great control over their physical properties such as size, shape, material composition, magnetic properties and surface coating[15-17]. Their high surface area is ideal for surface modifications. Jain et al have reported on an oleic acid/Pluronic F127 coated iron oxide nanoparticle able to carry a drug payload as well as provide contrast enhancement in T_2 imaging[16].

It has been found that doping iron oxide nanoparticles with magnetically susceptible elements such as Mn, Ni and Co can lead to an increase in the contrast agent's relaxivity[18].

1.3.3 Environmentally Responsive MRI contrast agents (non-REDOX)

Recent trends in MRI CA development have been around 'active' contrast agents. The majority of clinically used CAs are all blood pool agents, they are not site specific and must be either injected directly into the region of interest or if left to circulate uniformly around they body, only larger diseased areas are visible where there is clear leakage from the vascular system. In contrast, 'active' CAs are able to change their effect on the local relaxation rate based on environmental factors. The cellular microenvironment is tightly regulated by the presence of biomarkers, metal ions, enzymes, proteins, pH and REDOX potential. In the event of pathological conditions, these environmental factors are altered. The ability to sense these changes would provide a diagnostic system capable of detecting the early signs disease.

1.3.3.1 pH responsive

A key factor to detecting abnormal metabolic activity in tissue is the acidification of the local environment[19]. In addition, the change in pH is closely linked to tumour growth and development. The development of pH sensitive CAs has mainly revolved around changing either the inner-sphere interaction or the rotational correlation time of the CA. Kim et al. have developed a cancer-recognizable MRI contrast agent based on self-assembled amphiphilic block copolymers containing Gd-DTPA[20]. At physiological pH, the CA has a spherical shape with a size of around 40 nm. The Gd ions, located in the core of the micelle, are shielded from inner sphere interactions and hence do not induce any change in contrast. However, in acidic tumour environments (pH 6.5), imidazole groups present in the micelles are protonated and cause the network to break apart into small water soluble polymers. This opens up access for water molecules to exchange freely with the Gd ion, increasing the local relaxation rate. A similar 'pH-sensitive magnetic nanogrenade' has been reported by Ling et al[21].

1.3.3.2 Temperature responsive

The ability to selectively measure the temperature of specific areas of the body is a powerful tool when performing diagnostics or thermal therapies such as

thermal ablation or regional hyperthermia. The use of fibre-optic probes increases the chance of infection or local damage, therefore the development of imaging probes in order to indirectly view or measure the local temperature is important. Lindner et al. have developed thermo-responsive liposomes loaded with gadolinium or manganese based contrast agent[22]. The phospholipid membrane used has a well-defined gel-to-liquid crystalline phase transition temperature. At this temperature, the permeability of the membrane is increased due to its change from a gel phase to a liquid crystalline phase. Lindner shows that this leads to an increase in the T_1 relaxivity due to the increased water exchange between the outside and the paramagnetic compounds inside of the liposome, as well as the gradual release of the CA from inside. These have been successfully tested in animal models by McDannold et al., injecting them into rabbit liver and irradiating with ultrasounds[23]. The areas where the transition temperature T_m ~57°C was reached showed a persistent increase in T_1 signal intensity.

1.3.3.3 Bio-responsive

The detection of biologically relevant compounds such as enzymes, proteins or metal ions is another method for diagnosing potential pathological conditions.

Pathologically relevant enzyme detection is one area of key interest in responsive MRI CA design. Meade et al. have pioneered the area by developing a b-galactosidase and β-glucuronidase sensitive CAs[24-25]. In both cases, a Gd complex is linked to an enzyme cleavable group. Upon cleavage, the water exchange site is freed allowing for magnetic exchange between the Gd complex and the surrounding water, increasing the inner sphere T_1 relaxation.

Copper is one of the most abundant metals (after iron and zinc) present in the human body. Its role in various biological processes lends it to being an ideal marker for abnormal activity. One such application is in the detection of Alzheimer's where the concentration of copper in amyloid plaques can reach 400 μmol/L [26]. Li et al. have shown the synthesis of a Cu^{2+}-responsive MRI contrast agent[27]. Exploiting the chelating characteristics of a quinolone-based ligand (8-

amidequinoline) for Cu^{2+} binding, Li links it to a Gd^{3+} loaded DO3A unit. Upon addition of Cu^{2+}, a T_1 relaxivity enhancement of up to 71% is observed.

1.3.3.4 Light responsive

Bioluminescence and fluorescence has been greatly used during in vitro experiments due to its high sensitivity and the availability of many labelling compounds[28-29]. It has however very limited use in vivo due to the small penetration depths of UV and visible radiation[30].

1.3.4 REDOX responsive contrast agents

1.3.4.1 REDOX, ROS and Inflammation

When studying cellular microenvironments, many factors and biomarkers come into play, one of which is the intracellular and extracellular REDOX environment. REDOX potential is strongly regulated in tissues and any changes can be linked to both pathological and non-pathological conditions (cancer, Alzheimer's disease, psoriasis)[31].

The REDOX state of a cellular environment is usually defined using the redox couples glutathione/glutathione disulfide (GSH/GSSG) and nicotinamide adenine dinucleotide (NAD^+)/NADH.

Glutathione, due to its high concentration in cellular environments (1 – 11 mM) and its ability to be easily transported to the extracellular matrix, is the main REDOX buffer used to regulate cellular and extracellular REDOX potential[32].

Reactive Oxygen Species (ROS), oxidants such as hydrogen peroxide H_2O_2, superoxide O_2^- and hypochlorite OCl^-, are involved in a large number of oxidation reactions. They are typically found in areas of inflammation, and can be used as a marker when diagnosing inflammatory pathologies[33-35].

Inflammation occurs naturally in the body as a defence mechanism; protecting the organism from potentially infectious or damaging foreign bodies and aiding in tissue regeneration and repair. However if inflammation is persistent, it can

prevent tissue repair leading to degenerative pathologies such as rheumatoid arthritis, atherosclerosis, neurodegenerative diseases or developing cancers[36].

Typically, inflammation starts with the activation of nicotinamide adenine dinucleotide phosphate (NADPH) oxidase, a membrane-bound enzyme that can from superoxide anion radicals from its reaction with NADPH and free oxygen. These radicals, in turn, can from hydrogen peroxide through their reaction with superoxide dismutase, creating a chain reaction of ROS production[37-38].

The focus of this project is to use ROS sensitive materials to image areas of high ROS concentration via MRI. This would enable non-invasive imaging of pathological tissue for diagnosis.

1.3.4.2 REDOX responsive contrast agents

Current research on REDOX sensitive contrast agents is focused on developing T_1 contrast agents which alter their relaxivity in the presence of reducing agents. These take advantage of reduced thiol groups present in the extracellular matrix such as the thiol of cysteine-34 on Human serum albumin (HSA). Jagadish et al. have developed a Gd-DOTA derivative with a pendant thiol group. Depending on the oxidation state of HAS, a dithiol link can be created between the two compounds leading to the increase in rotational correlation time of the Gd-DOTA and therefore an increase in longitudinal relaxivity [39].

Martinelli et al. have taken another approach to the development of a reduction sensitive CA using β-cyclodextrin based nanocapsules. They consist of perthiolated β-CD, linked together by disulfide bridges to form a closed nano-carrier for Gd(III) complexes. Under reducing conditions, the disulfide bonds are broken allowing for the Gd complex to diffuse out, hence increasing the magnetic exchange with surrounding water protons and increasing longitudinal relaxivity.

Viger et al. have recently shown a bio-responsive T_1 contrast agent based on Gd oxide nanoparticles encapsulated in responsive polymer microparticles. In one instance, polyester bearing boronic ester based polymer microparticles, are used

to encapsulate the Gd oxide nanoparticles. Upon oxidation with H_2O_2, the particles release their payload. Viger obtained a maximum increase in r_1 of 11-fold. He used a similar system with a pH responsive polymer[40].

1.3.5 Targeted MRI contrast agents

Much less researched, however just as important, are targeted MRI CAs. These usually consist of a magnetic medium linked to a targeting group such as an antibody or specific peptides that enhances specific binding. The original strategy for developing these CAs was to bind a standard gadolinium based complex, typically Gd-DTPA, to an antibody[41]. This however, did not produce clinically usable contrast agents due to the inherently low sensitivity of MRI and of Gd CAs combined with the low concentration of targetable compounds. Efforts then turned to conjugating multiple Gd complexes to one antibody or peptide.

1.4 Molecular magnets

1.4.1 Single molecule magnetism

Single molecule magnets (SMMs) or molecular nanomagnets are organic molecules containing one or more metal centres with unpaired electrons. These complexes are surrounded by organic ligands, usually through carboxylate links. The metal centres are anti-ferromagnetically coupled to each other, this allows for the engineering of clusters with precise ground state spins. The first SMM that was discovered was a Mn_{12}-containing complex, $[Mn_{12}O_{12}(O_2CMe)_{16}(H_2O)_4]$, first synthesised by Lis et al. in 1980, whose properties were measured by Caneschi et al. in 1991[42-43]. The eight Mn^{III} ions, with a ground state spin of 2, and the four Mn^{IV} ions with ground state spin of 3/2, couple together anti-ferromagnetically to giving the cluster an overall ground-state spin of 10.

1.4.2 Heterometallic wheels

One form of molecular magnet are cyclic metallic clusters, of which the heterometallic Cr_7M wheels are a member of. These wheels were first synthesised by Larsen et al. in 2003[44]. Larsen derived these from the Cr8 homometallic wheel first synthesised in 1985(48). By refluxing CrF_3•H2O with

pivalic acid in DMF, the homometallic wheels were easily formed. The Cr^{III} ions are bridged to each other via one fluoride and two pivalate groups into a cyclic structure. The eight Cr^{III} ions, each with a spin of 3/2, couple to each other creating an S = 0 ground state spin.

In order to synthesise the heterometallic variation, Larsen added a divalent metal to the reaction mixture. In a first instance, $2NiCO_3 \bullet 3Ni(OH)_2 \bullet 4H_2O$ was used to form a Cr_7Ni heterometallic wheel (Figure 1.4-9). This synthesis route can be extended to other M^{II} ions by adding the corresponding second metal salt (M = Mn, Fe, Cd). As with the homometallic wheels, each metal centre is linked by a fluoride and two carboxylate groups for a total of eight fluoride atoms and sixteen carboxylates. The wheel is template around a central amine, located in the cavity, hydrogen bonded to the fluorides.

Unlike the Cr_8 wheel, Cr_7Ni heterometallic wheels have a non-zero ground state spin. The eight anti-ferromagnetically coupled metal centres, seven Cr^{III} with a spin of 3/2 and one Ni^{II} with a spin of 1, give a resulting ground state spin of S = ½. This has been confirmed with the Q-band EPR spectra of the wheels showing a typical S = ½ absorption spectra with axial symmetry (g_{xy} = 1.781, g_x = 1.740).

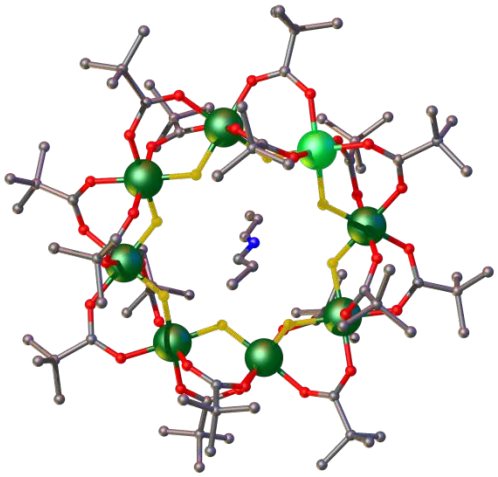

Figure 1.4-9 Crystal structure of $[(C_3H_7)_2NH_2][Cr_7NiF_8((CH_3)_3CCO_2H)_{16}]$ with hydrogen bonds omitted for clarity. Dark green (Cr), light green (Ni), yellow (F), red (O)[44].

1.4.3 Wheel customisation

One major advantage of using these heterometallic wheels is their possibility to be heavily customised. Using different trivalent or divalent metals, changing the ammonium template or altering the carboxylate used gives access to over 1400 different combinations[45]. The primary focus of this project was to see how changing the carboxylate group and the metal ions alter the ring's ability to be loaded into nano-carriers, as well as its interaction with water, changing its magnetic relaxation properties. Using metal centres with higher spin states, such as gadolinium or dysprosium could help to improve the magnet's effect on relaxivity. In addition, using short ligands compared to longer ones would reduce the distance between the water proton and the metal cores. Although these rings do not have any water binding sites, it could be interesting to use a ligand which allows water to hydrogen bond to it, to see if it could affect its T_1 relaxivity.

1.4.4 SMM as MRI contrast agents

There exist very few examples of single molecule magnet structures applied to the MRI contrast agent domain. The molecular magnet Fe_8 has been investigated multiple times as a potential CA with conflicting results[46-48]. It has been shown that $_{Fe8}$ acts as a T_1 contrast agent despite the lack of direct water binding sites on its surface[46]. Its efficiency compared to Gd-DTPA however has been disputed, some studies show that it performs better, others show that it doesn't perform as well depending on environmental conditions (temperature, pH, concentration).

Another molecular magnet that has been shown to be an effective T_2 contrast agent is Mn_{12} cluster[49]. Wang successfully dispersed the clusters in water using stearic acid in an emulsion assisted self-assembly method. Its T_2 relaxivity was measured to be 190.54 $mM^{-1}s^{-1}$, in water.

1.5 Polysulfide nano-carriers

1.5.1 Episulfide polymerisation

Polysulfides are a class of synthetic polymers which contain multiple sulfur(II) atoms. Originally, the synthesis of polysulfides was performed via step polymerisation; this form of polymerisation involves the use of a sulfur-containing nucleophile such as an organic thiol or an alkali metal sulfide[50-51]. However, step polymerisation has shown to have very little control over molecular weight. To overcome this limitation, chain polymerisation has been investigated as another method for polysulfide synthesis. In this project, anionic ring opening polymerisation of episulfides (namely propylene sulfide, PS) has been selected for the preparation of poly(propylene sulfide) (PPS) nanoparticles. This polymerisation method avoids the common problems of termination/cross-linking or slow kinetics and depolymerisation of other ring opening reactions[52]. In this way, preparation of narrow dispersity macromolecules with an excellent control over terminal groups, possibly featuring a blocky structure can be prepared[53-57]. Episulfide polymerisation can be carried out under mild

conditions, and can be performed in protic media, provided that disulfide impurities are removed[58-59].

Another interesting feature of episulfide polymerisation is its living character. During a living polymerization, the rate of initiation is greater than the rate of propagation resulting in more uniform chain lengths and hence a low polydispersity[60]. Living polymerizations also lack the ability to self-terminate. Polymers synthesized via this method require an additional reagent to either end-cap and/or functionalise the chain ends. In the case of polysulfide synthesis, the thiolate end groups can be easily functionalised, for instance, with mono- or polyfunctional cross-linkers (leading to linear polymers or cross-linked polymer networks, respectively). For instance, Rehor et al have shown that the PPS chains can be functionalised with fluorescent dyes as well as end-cappers to stop further polymerisation[61].

1.5.2 Anionic polymerization of propylene sulfide

The first experimental investigations of episulfide anionic polymerization were performed by Boileau et al. of the University of Paris 6. Their experiments focused primarily on the polymerization of the episulfide monomer propylene sulfide (PS). It was found that the ideal conditions for episulfide polymerization occurred when using an anionic-coordinated initiator, producing polymers with high stereoregularity. With episulfides, Boileau showed that if the propagating species, thiolates, were in the form of free ions rather than ion pairs, the reaction was accelerated[62-63].

The initiator which will be used in the polymerization of the PPS in the core of the nanoparticle is 3,6-dioxa-1,8-octanedithiol. This is a double ended sulfur based initiator. The reason a sulfur base initiator is used, rather than other nucleophiles such as tertiary amines, phosphines or carboxylates, is to do with the initiation rate (compared to the propagation rate). When a non-sulfur based initiator is used, it was found that the initiation rate was slow compared to the propagation rate[64]. However, if the initiator is similar to the propagating species,

then the initiation rate will be similar to the propagation rate, hence resulting in a more controllable reaction.

1.5.3 Disulfide formation

One drawback, however, to episulfide polymerisation is the possible formation of disulfides which can act as chain transfer agents during an episulfide polymerisation[65]. In this polymerization, both the initiating and propagating species are thiolates. Due to the relatively low pKa of thiols (7 to 11 in water), only mild conditions are required to preserve the living character of the polymerization, preventing the protonation of the thiolates. However, the drawback to using thiolates as propagating species is their ability to form disulfide impurities; these in turn have a negative effect on the episulfide polymerization. The sole presence of disulfide impurities reduces the number of initiating groups via early chain termination and therefore reduces the overall degree of polymerization; however, disulfides can also act as chain transfer agents, exchanging with thiolates at different stages of the polymerization [28]. In the case where the transfer occurs between a thiolate terminated polymer and a low molecular weight disulfide, two outcomes are possible. The new molecule would have the same mass as the original but with the formation of a heterodisulfide at the end of the chain, or the molecular weight would double in the case of dimerization to homodisulfide. The former would be easier to manipulate and possibly reduce; however, the latter is a more hindered disulfide.

There are however, methods to overcome/minimise this disulfide formation; they include adding a reducing agent to the polymerisation media to reduce any disulfide bonds or using a protected initiator to be deprotected either in situ or just before the reaction[65].

For this reason, the initiator, 3,6-dioxa-1,8-octanedithiol, is protected by reacting it with acetyl chloride. It is then deprotected with sodium methoxide under inert conditions immediately prior to use[60]. This reduces the possibility of the formation of disulfides during the synthesis.

1.5.4 Poly(propylene sulfide) nanoparticles

PPS nanoparticles are a development on the episulfide polymerisation of PS. These nanoparticles were first synthesized by Rehor et al. to take advantage of the oxidation sensitive properties of polysulfides[66-67].

When describing oil-in-water polymerization techniques for nanoparticles, there exist three primary methods: emulsion polymerization, micro-emulsion polymerization and dispersion polymerization.

In an emulsion polymerization, stabilized monomer droplets are formed in the water phase. The initiator is usually water soluble and present in the dispersed phase. The polymerization begins when monomer diffuses out of the stabilized droplets into the micelles which are present in the water phase. As they diffuse across, they begin their polymerization with the free, water soluble, initiator molecules. Due to their large surface area, the smaller micelles are more likely to react with free initiator and monomer, increasing their size. In the end, the free monomer droplets disappear leaving behind polymer nanoparticles stabilized by surfactant. These particles are usually larger, on the order of hundreds of nanometers to micrometers. In order to keep the emulsion stable and prevent the particles for coalescing, high shear forces must be applied, this is usually done via magnetic or mechanical agitation[68].

The primary difference between an emulsion polymerization and a microemulsion polymerization is the need of external energy for an emulsion polymerization. Microemulsions usually do not require external energy to form; they spontaneously create micellar particles with average particle sizes below 20nm[68-69].

Dispersion polymerization is a third method for synthesizing nanoparticles. This starts from a homogenous mixture of reagents. Nucleation sites for the particles start in the medium and slowly grow. This form of particle synthesis is slow but creates very monodisperse particles with sizes between 1-20μm[70].

Emulsions are an example of phase separated systems. They are usually composed of three components, the disperse phase, the dispersed phase and a surfactant. The 'classical' emulsion is an oil-in-water emulsion. In this case, the disperse phase is water, the dispersed phase is oil and the surfactant is some amphiphilic polymer. The topological structure of the emulsion is dependent on the ratios between the three phases. In a low surfactant mixture, there will be a clear phase separation between the oil and water. If any surfactant is present in the mixture, it will arrange itself as a monolayer between the two phases. The hydrophobic part of the molecule in the oil phase and the hydrophilic part in the water phase.

If on the other hand, the solution is only water and surfactant, at low concentrations, the surfactant starts off as free molecules in the water. The system will try to lower its free energy by aligning the surfactant molecules along the air-water interface in order to reduce surface energy. As the concentration of surfactant increases, it will reach a critical point known as the critical micelle concentration (cmc). At this point, the surfactant molecules begin to aggregate into small spherical structures called micelles. This allows them to reduce even more the free energy of the system by reducing the area of contact between the hydrophobic parts of the surfactant molecules and the water phase.

At this point, above the cmc, if an oil phase is introduced, the oil molecules will localize themselves in the core of the micelles formed by the surfactant, forming an emulsion. From this point on, if more surfactant is added, the emulsion structure will change to cylindrical micelles, the reason for this structure change is due to the surface energy of the particles. Above a certain surface area, spherical particles are no longer the most energy efficient systems and therefore change their topological structure to cylindrical.

On the other hand, if at low surfactant concentration, the oil phase is greater than the water phase, a phase inversion will occur. This involves the spherical micelles 'flipping' inside-out. The oil phase will become the disperse phase and the water phase will become the dispersed phase. From this point, if the

surfactant concentration is increased, it will follow the same phase as previously described, however in an inverted state.

The synthesis of PPS nanoparaticles is neither strictly an emulsion polymerization nor a mini-emulsion polymerization. This synthesis proceeds via the use of non-water soluble monomer and initiator. Before the polymerization is initialized, all of the material is located in preformed 'nano-droplets' stabilized by the surfactant Pluronic-F127. The synthesis takes place inside the droplets; in the end the droplets are cross-linked to form elastic nanoparticles. This synthesis technique creates particles ranging in sizes from 30nm up to 500nm.

Pluronic-F127 is a triblock copolymer consisting of a central hydrophobic block of polypropylene glycol (PPG), surrounded by two hydrophilic polyethylene glycol (PEG) blocks. The surfactant entangles itself with the PPS core, the polypropylene glycol block physically linked into the PPS chains and the polyethylene glycol blocks pointing outwards.

Until the nanoparticles are cross-linked via Michael-type addition with a tetra-functional cross-linker, the droplets remain in equilibrium under stirring. This droplet form is necessary for the loading of the molecular nanomagnets into the core as diffusion through a liquid core is easier than through a cross-linked rubbery core. Once the nanomagnets are in the core of the nanoparticles, the core is cross-linked creating a coherent network entrapping the nanomagnets.

There are many properties that support the use of polysulfide nanoparticles in the development of novel MRI contrast agents.

1) In a first instance, the Pluronic F-127 surfactant of the nanoparticles has been used in pharmaceutics and coatings as bio-compatible sheathes. The PEG coating prevents the absorption of proteins, hence reducing the probability of uptake by the body's immune system (stealth properties).

2) Another important factor which controls the uptake of the nanoparticles in the body is the size distribution. Rehor et al. showed that PPS nanoparticles prepared by emulsion polymerisation have very uniform size distributions, and

their size can be easily controlled by tuning the ratio of surfactant to monomer; the higher the ratio, the smaller the nanoparticles. This way, nanoparticles of 33, 55, 100 and 154nm were prepared in this work[71]. It is generally accepted that particles with a hydrodynamic size greater than 200nm will be very quickly uptaken by the body's reticuloendothelial system (RES), preventing them from freely circulating the body for imaging purposes; on the other hand, nanoparticles smaller than 20nm will be filtered out by the body's renal and liver systems[72-73].

3) Another advantage of this synthesis is its 'one pot' approach. As the synthesis is performed in one reactor, it is possible to easily scale up the production of the nanoparticle synthesis. This is crucial for an MRI contrast agent. In the planning for this to become a commercial product, scale up is a very important step in this process. Enabling this early on in the research will simplify some aspects of the route to commercialization.

4) Another important characteristic of PPS nanoparticles which is essential to the loading of the nanomagnets is their hydrophobic core. The cross-linked core of the nanoparticles behaves as a 'rubbery', elastic material. This will enable the nanomagnets to diffuse homogeneously through the nanoparticle core and create a uniform magnetic field throughout the nanoparticle. The hydrophobic nature of the nanomagnets, due to hydrophobic groups on their outside, will force them to stay within the nanoparticle, not allowing them to leach out into the body.

5) Finally, the shell structure of the PPS nanoparticles could allow for further functionalisation via the incorporation of reactive functional groups at the distal ends of PEG chains (for instance, by modification of Pluronic or, more interestingly, by incorporation of a functional PEG-polymer derivative during micelle formation). This would allow the introduction of targeting ligands for active targeting imaging purposes (nanoparticles which can selectively recognise cell receptors for specific tissue imaging). Thus, this active targeting approach

could enable, for instance, a more precise imaging of tumours, with images showing a well-defined boundary between cancerous and healthy tissues.

1.6 Scope of the thesis

The area of contrast agent development is highly active, however there are only a limited selection of materials that are being used, primarily gadolinium based complexes for T_1 CAs and iron oxide based nanoparticles for T_2 CAs. In addition, the development of responsive or targeted contrast agents is growing due to the need for more precise diagnostic tools allowing for the earlier detection of diseased areas as well as the need for a lower administered dose. This thesis focuses on the development of a high relaxivity T_2 contrast agent, sensitive to Reactive Oxygen Species (ROS). In particular, the use of novel magnetic material (for biological applications), allowed a high T_2 relaxivity to be achieved.

Chapter 2 reports an in-depth study on the synthesis and the oxidation properties of poly(propylene sulfide) nanoparticles. It was necessary to fully understand the nanoparticles before using them as carriers for the molecular nanomagnets. This includes the internal structure and composition of the nanoparticles as well as their response to oxidants.

Chapter 3 is a short, high-impact article showing the key results for the most performant system, PPS nanoparticles loaded with Cr_7Ni heterometallic wheels functionalised with 2,2-ethylhexanoic acid. It includes their synthesis and magnetic characterisation, as well as their response to the presence of different amounts of hydrogen peroxide.

Chapter 4 presents a complete comparison between the four different magnets what were used in this project. Three of which are Cr_7Ni heterometallic wheels with different functionalization groups and one gadolinium containing molecular nanomagnet. The loading efficiency based on magnet composition is compared, as well as the r_2 relaxation rates before and after oxidation with hydrogen peroxide.

1.7 References

1 P. Caravan, *Chem. Soc. Rev.*, 2006, **35**, 512.

2 D. Weishaupt, V. D. K\Hochli and B. Marincek, *How does MRI work?: an introduction to the physics and function of magnetic resonance imaging*, Springer, 2003.

3 M. H. Levitt, *Spin Dynamics: Basics of Nuclear Magnetic Resonance*, John Wiley & Sons, New York, 2008.

4 R. S. Macomber, *A complete introduction to modern NMR spectroscopy*, Wiley, 1998.

5 P. Callaghan, *Principles of Nuclear Magnetic Resonance Microscopy*, Oxford University Press, 1994.

6 G. E. Gold, E. Han, J. Stainsby, G. Wright, J. Brittain and C. Beaulieu, *American Journal of Roentgenology*, 2004, **183**, 343.

7 A. S. Merbach, L. Helm and É. Tóth, *The Chemistry of Contrast Agents in Medical Magnetic Resonance Imaging*, Wiley, 2013.

8 D. W. McRobbie, E. A. Moore, M. J. Graves and M. R. Prince, *MRI from Picture to Proton*, Cambridge University Press, 2006.

9 M. M. Amiji, *Nanotechnology for Cancer Therapy*, CRC Press, 2006.

10 H. Shokrollahi, *Materials Science and Engineering: C*, 2013, **33**, 4485.

11 S. Laurent, L. V. Elst and R. N. Muller, *Contrast Media & Molecular Imaging*, 2006, **1**, 128.

12 M. H. M. Dias and P. C. Lauterbur, *Magnetic Resonance in Medicine*, 1986, **3**, 328.

13 N. J. Wittenberg and C. L. Haynes, *Wiley Interdisciplinary Reviews: Nanomedicine and Nanobiotechnology*, 2009, **1**, 237.

14 S.-Y. Shim, D.-K. Lim and J.-M. Nam, *Nanomedicine*, 2008, **3**, 215.

15 W. J. Rogers and P. Basu, *Atherosclerosis*, 2005, **178**, 67.

16 T. K. Jain, M. A. Morales, S. K. Sahoo, D. L. Leslie-Pelecky and V. Labhasetwar, *Molecular Pharmaceutics*, 2005, **2**, 194.

17 M. Bradbury and H. Hricak, *Magnetic Resonance Imaging Clinics of North America*, 2005, **13**, 225.

18 S. Sun, H. Zeng, D. B. Robinson, S. Raoux, P. M. Rice, S. X. Wang and G. Li, *Journal of the American Chemical Society*, 2004, **126**, 273.

19 L. M. De Leon-Rodriguez, A. J. M. Lubag, C. R. Malloy, G. V. Martinez, R. J. Gillies and A. D. Sherry, *Acc. Chem. Res.*, 2009, **42**, 948.

20 K. S. Kim, W. Park, J. Hu, Y. H. Bae and K. Na, *Biomaterials*, 2014, **35**, 337.

21 D. Ling, W. Park, S.-j. Park, Y. Lu, K. S. Kim, M. J. Hackett, B. H. Kim, H. Yim, Y. S. Jeon, K. Na and T. Hyeon, *Journal of the American Chemical Society*, 2014, **136**, 5647.

22 L. H. Lindner, H. M. Reinl, M. Schlemmer, R. Stahl and M. Peller, *International Journal of Hyperthermia*, 2005, **21**, 575.

23 N. McDannold, S. L. Fossheim, H. Rasmussen, H. Martin, N. Vykhodtseva and K. Hynynen, *Radiology*, 2004, **230**, 743.

24 R. A. Moats, S. E. Fraser and T. J. Meade, *Angew. Chem. Int. Ed. Engl.*, 1997, **36**, 726.

25 J. A. Duimstra, F. J. Femia and T. J. Meade, *Journal of the American Chemical Society*, 2005, **127**, 12847.

26 P. Faller and C. Hureau, *Dalton Transactions*, 2009, 1080.

27 W.-S. Li, J. Luo and Z.-N. Chen, *Dalton Transactions*, 2010, **40**, 484.

28 C. Tu and A. Y. Louie, *Chemical Communications*, 2007, 1331.

29 E. A. Osborne, B. R. Jarrett, C. Tu and A. Y. Louie, *Journal of the American Chemical Society*, 2010, **132**, 5934.

30 C. Tu, E. A. Osborne and A. Y. Louie, *Annals of Biomedical Engineering*, 2011, **39**, 1335.

31 E. H. Sarsour, M. G. Kumar, L. Chaudhuri, A. L. Kalen and P. C. Goswami, *Antioxid. Redox Signal.*, 2009, **11**, 2985.

32 S. Chakravarthi, C. E. Jessop and N. J. Bulleid, *EMBO Reports*, 2006, **7**, 271.

33 Q. Wang, X. N. Tang and M. A. Yenari, *Journal of Neuroimmunology*, 2007, **184**, 53.

34 G. Poli and M. Parola, *Free Radical Biology and Medicine*, 1997, **22**, 287.

35 N. R. Madamanchi, S.-K. Moon, Z. S. Hakim, S. Clark, A. Mehrizi, C. Patterson and M. S. Runge, *Arteriosclerosis, Thrombosis, and Vascular Biology*, 2005, **25**, 950.

36 R. d'Arcy and N. Tirelli, *Polym. Adv. Technol.*, 2014, **25**, 478.

37 K. Bedard and K.-H. Krause, *The NOX Family of ROS-Generating NADPH Oxidases: Physiology and Pathophysiology*, 2007.

38 K. K. Griendling, D. Sorescu and M. Ushio-Fukai, *Circulation Research*, 2000, **86**, 494.

39 B. Jagadish, G. P. Guntle, D. Zhao, V. Gokhale, T. J. Ozumerzifon, A. M. Ahad, E. A. Mash and N. Raghunand, *J. Med. Chem.*, 2012, **55**, 10378.

40 M. L. Viger, J. Sankaranarayanan, C. de Gracia Lux, M. Chan and A. Almutairi, *Journal of the American Chemical Society*, 2013, **135**, 7847.

41 D. Shahbazi-Gahrouei, M. Williams, S. Rizvi and B. J. Allen, *Journal of Magnetic Resonance Imaging*, 2001, **14**, 169.

42 T. Lis, *Acta Crystallographica Section B*, 1980, **36**, 2042.

43 A. Caneschi, D. Gatteschi, R. Sessoli, A. L. Barra, L. C. Brunel and M. Guillot, *Journal of the American Chemical Society*, 1991, **113**, 5873.

44 F. K. Larsen, E. J. L. McInnes, H. E. Mkami, J. Overgaard, S. Piligkos, G. Rajaraman, E. Rentschler, A. A. Smith, G. M. Smith, V. Boote, M. Jennings, G. A. Timco and R. E. P. Winpenny, *Angewandte Chemie International Edition*, 2003, **42**, 101.

45 R. H. Laye, F. K. Larsen, J. Overgaard, C. A. Muryn, E. J. L. McInnes, E. Rentschler, V. Sanchez, S. J. Teat, H. U. Gudel, O. Waldmann, G. A. Timco and R. E. P. Winpenny, *Chemical Communications*, 2005.

46 E. Rodríguez, A. Roig, E. Molins, C. Arús, M. R. Quintero, M. E. Cabañas, S. Cerdán, P. Lopez-Larrubia and C. Sanfeliu, *NMR in Biomedicine*, 2005, **18**, 300.

47 S. Isaacman, R. Kumar, E. D. Barco, A. D. Kent, J. W. Canary and A. Jerschow, *Polyhedron*, 2005, **24**, 2691.

48 B. Cage, S. E. Russek, R. Shoemaker, A. J. Barker, C. Stoldt, V. Ramachandaran and N. S. Dalal, *Polyhedron*, 2007, **26**, 2413.

49 Y. Wang, W. Li, S. Zhou, D. Kong, H. Yang and L. Wu, *Chemical Communications*, 2011, **47**, 3541.

50 W. D. Graaf, J. S. S. Damsté and J. W. d. Leeuw, *Geochimica et Cosmochimica Acta*, 1992, **56**, 4321.

51 C. S. Marvel and A. Kotch, *Journal of the American Chemical Society*, 1951, **73**, 1100.

52 C. C. Price and E. A. Blair, *Journal of Polymer Science Part A-1: Polymer Chemistry*, 1967, **5**, 171.

53 G. Kilcher, L. Wang, C. Duckham and N. Tirelli, *Macromolecules*, 2007, **40**, 5141.

54 O. Nuyken, T. Pöhlmann and M. Herberhold, *Macromolecular Chemistry and Physics*, 1996, **197**, 3343.

55 A. Napoli, N. Tirelli, G. Kilcher and A. Hubbell, *Macromolecules*, 2001, **34**, 8913.

56 C. Bonnans-Plaisance, M. Jean and F. Lux, *European Polymer Journal*, 2003, **39**, 863.

57 G. Kilcher, D. Delneri, C. Duckham and N. Tirelli, *Faraday Discussions*, 2008, **139**, 199.

58 A. Rehor, N. Tirelli and J. A. Hubbell, *Macromolecules*, 2002, **35**, 8688.

59 C. Bonnans-Plaisance and G. Levesque, *Macromolecules*, 1989, **22**, 2020.

60 L. Wang, G. Kilcher and N. Tirelli, *Macromolecular Bioscience*, 2007, **7**, 987.

61 *Macromolecular Chemistry and Physics*, 2009, **210**, 447.

62 S. Boileau, G. Champetier and P. Sigwalt, *Die Makromolekulare Chemie*, 1963, **69**, 180.

63 S. Boileau and P. Sigwalt, *COMPTES RENDUS HEBDOMADAIRES DES SEANCES DE L ACADEMIE DES SCIENCES*, 1961, **252**, 882.

64 N. Spassky and P. Sigwalt, *Tetrahedron Letters*, 1968, **9**, 3541.

65 G. Kilcher, L. Wang and N. Tirelli, *Journal of Polymer Science Part a-Polymer Chemistry*, 2008, **46**, 2233.

66 A. Rehor, 2005, p. 148.

67 A. Rehor, N. E. Botterhuis, J. A. Hubbell, N. Sommerdijk and N. Tirelli, *Journal of Materials Chemistry*, 2005, **15**, 4006.

68 C. S. Chern, *Principles and Applications of Emulsion Polymerization*, Wiley, 2008.

69 J. C. Salamone, *Concise Polymeric Materials Encyclopedia*, Taylor & Francis, 1998.

70 M. Okubo, *Polymer Particles*, Springer, 2005.

71 A. Rehor, J. A. Hubbell and N. Tirelli, *Langmuir*, 2005, **21**, 411.

72 B. L. Allen, J. D. Johnson and J. P. Walker, *ACS Nano*, 2011, **5**, 5263.

73 F. Alexis, E. Pridgen, L. K. Molnar and O. C. Farokhzad, *Molecular Pharmaceutics*, 2008, **5**, 505.

1.8 Appendix - Characterisation techniques

1.8.1 Electron paramagnetic resonance (EPR)

Electron Paramagnetic Resonance (EPR) uses magnetic fields and microwaves to study compounds with one or more unpaired electrons. The use of EPR dates back to World War II, with Soviet physicist Zavoisky who experimented with the interaction of static magnetic fields with materials[1]. EPR is a powerful technique for studying and understanding many different kinds of materials including organic radicals and transition metals[2]. In this thesis, however, this technique is used to detect the presence of paramagnetic heterometallic clusters.

The easiest case to understand is with a material that has an S=1/2 ground state spin, so only one unpaired electron. At room temperature, without an external magnetic field, the free electron could be in any of the two m_s= +1/2 or m_s = -1/2 spin states. When an external magnetic field is applied, Zeeman splitting occurs and a large energy gap is produced between the two states. The difference in population between the two states is what influences the EPR signal intensity and is controlled by the Boltzmann distribution; which says that lower temperatures increases the population difference between the two states. EPR is therefore usually performed at temperatures on the order of 5-10K. Once all the electrons are in the ground state, m_s= -1/2, a defined amount of energy will need to be applied for the electron to be excited up to its higher energy state.

$$\Delta E = h\nu = g\beta H \qquad \textbf{Equation 1.8-14}$$

This population depletion is created by a microwave excitation which excites the electrons up to the m_s = +1/2 state. Relaxation back to the ground state is achieved via intrinsic spin-lattice relaxation process. The signal obtained from an EPR measurement is the first derivative of the absorption spectrum.

1.8.2 Nuclear magnetic resonance (NMR)

In 1938, Isidor Isaac Rabi started work on the interaction of matter with electromagnetic waves in magnetic fields[3]. This work was later refined into

modern day nuclear magnetic resonance spectroscopy as we know it today by Felix Bloch and Edward Mills Purcell in 1945, for which they won the Nobel Prize in Physics in 1952[4]. Conceptually, NMR is identical to EPR, however, instead of observing excited electrons, NMR observes protons. The most common form of NMR is ^{1}H NMR, the technique used throughout this thesis. A description of how NMR works is detailed in Chapter 1.

1.8.3 Dynamic light scattering (DLS)

Dynamic light scattering (DLS) is a technique developed to measure size distributions of colloidal dispersions. It uses time dependent light intensity measurements of scattered light in order to measure diffusion coefficients of the objects in the dispersion.

Sub-micron particles in solution follow a physical phenomenon called Brownian motion. This can be described as the random motion of objects under the sole effect of thermal energy (proportional to k_bT) and particle/liquid collisions-the effects of gravity are negligible. Considering a complete conversion between thermal energy and kinetic energy, it results that there is an inverse relationship between the mass of the particle and its velocity. Therefore, the smaller the particle, the faster it will move under Brownian motion.

Measuring the speed of a moving particle is difficult; however monitoring its average displacement over time, or diffusion coefficient (D), is considerably easier. The Stokes-Einstein equation, makes it possible to convert the diffusion coefficient to the hydrodynamic radius (R_h) using Boltzmann's constant, k_B.

$$R_h = \frac{k_B T}{3\pi\eta D} \qquad \textbf{Equation 1.8-15}$$

In order to measure the diffusion coefficient of particles, DLS uses intensity fluctuations of scattered light to measure local particle concentration as a function of time. As long as the particles are smaller than the wavelength used, the light will scatter in all directions (Rayleigh scattering). The intensity of light scattered will fluctuate over time due to the motion of the particles in the

solution. This is due to the change in constructive and destructive interference as the particles move relative to each other. From this, an autocorrelation function can be derived between the intensity of light at time t and at t+τ.

$$g(t) = \int I(t) * I(t+\tau)dt \qquad \textbf{Equation 1.8-16}$$

If the sample is monodisperse, the correlation curve will be a simple exponential with a high correlation at short times, as the particles have not moved much, and no correlation at long times (Figure 1.8-10).

In this simple case, the autocorrelation curve is fitted with a single exponential decay function.

$$g(q,t) = \exp(-\Gamma t) \qquad \textbf{Equation 1.8-17}$$

$$\Gamma = Dq^2 \qquad \textbf{Equation 1.8-18}$$

$$q = \frac{4\pi n}{\lambda_0}\sin(\theta/_2) \qquad \textbf{Equation 1.8-19}$$

The decay is governed by the decay rate Γ. Γ is directly linked to the diffusion coefficient D via the wave vector q, a parameter dependent on the experimental set up (wavelength, refractive index and detector angle).

For more complex polydisperse systems, the autocorrelation function is a sum of exponential decay functions; each corresponding to a species in the population. In order to obtain the polydispersity index of the system, cumulant method may be used. In addition to the sum of exponentials, the average decay rate may be obtained as well as the second order polydispersity index, an indication of the variance. From the average decay rate, the z-averaged diffusion coefficient and therefore size may be obtained.

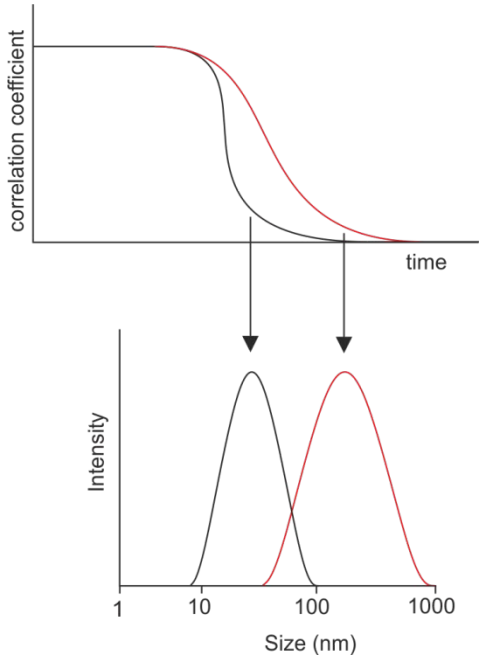

Figure 1.8-10 Typical correlation curves and corresponding size distribution obtained from monodisperse colloidal samples. The autocorrelation function (top) decays faster for smaller particles (black line) than for larger particles (red line).

There are, however, some draw backs to using DLS. First, DLS measures the hydrodynamic size of the particles, this includes the layer of solvent molecules that are located on the surface of the particles and diffuse with them. Second, DLS assumes that the sample consists of hard, perfectly spherical particles with a uniform refractive index. It is in this assumption that many of the errors arise. Very few, if no, samples are completely spherical and of uniform refractive index. Many colloids may have a dynamic shape, or an ill-defined surface.

In the case of this project, the DLS measurement of the swollen nanoparticles is one example of this. As the PPS nanoparticles swell with water, their refractive index changes and therefore induce an error on the fitting parameters. In order to overcome this, diffusion ordered spectroscopy was use.

1.8.4 Diffusion ordered spectroscopy (DOSY)

In chapter 2, the oxidation of the PPS nanoparticles was studied by both DLS and diffusion ordered spectroscopy (DOSY). Where DLS uses optical methods to

measure intensity distributions of the nanoparticles, DOSY uses gradient enhanced nuclear magnetic resonance to measure number distributions.

DOSY combines r.f pulses used in NMR with magnetic field gradients that encode spatial information to obtain diffusion coefficients of the different species in the solution.

In the simplest case, a 90° pulse is applied to the sample followed by a pulsed magnetic field gradient. This disperses the magnetization vector of the spins across the tube resulting in a zero net signal. After a certain time, a 180° pulse is applied to invert the spins, followed by a second gradient pulse to refocus the signal. In the case where no diffusion has occurred between the initial pulse and the final pulse, the difference in initial signal and final signal will be zero. However, if there has been diffusion though the tube, spins will experience different refocusing pulses from their original pulse causing a drop in signal as full refocusing will not have happened. The more a nucleus has diffused, the lower the final signal (Figure 1.8-11). The intensity and duration of the magnetic field pulses are what determine the distance a nucleus can travel and therefore its final signal.

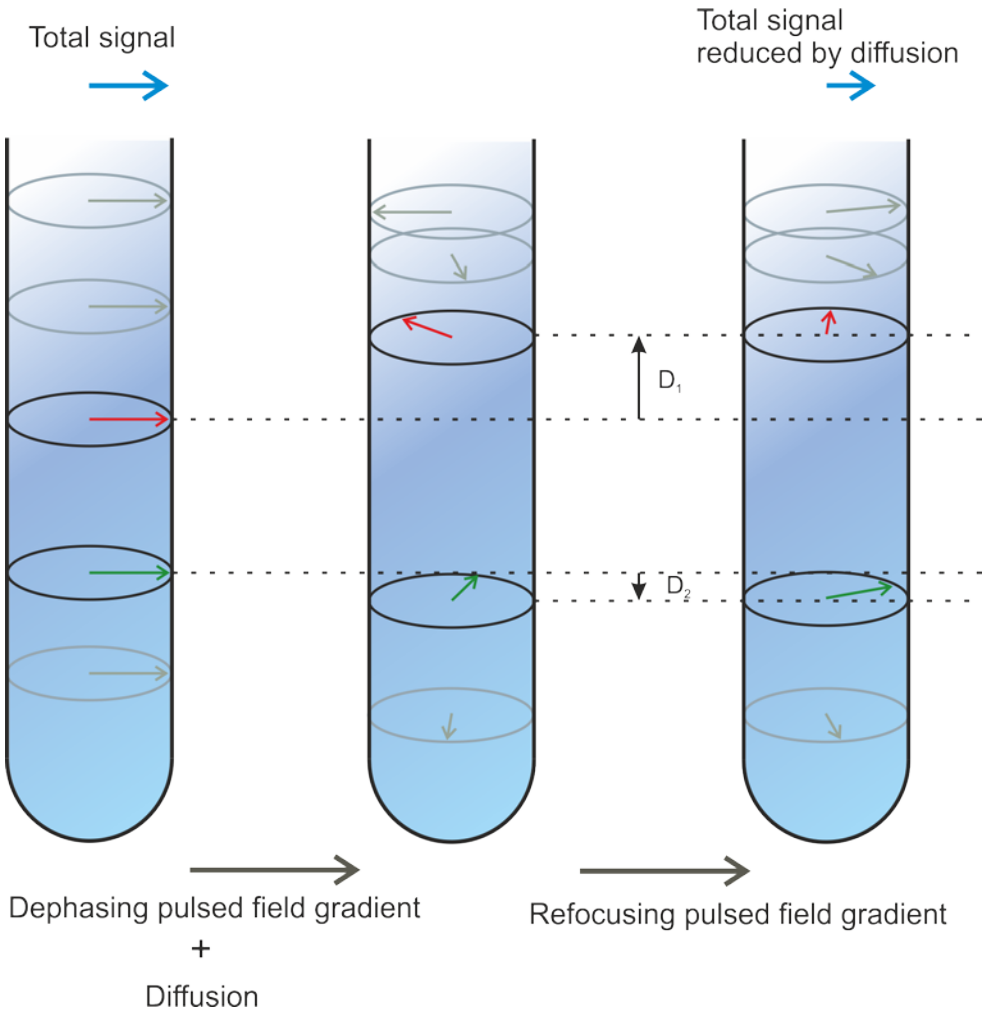

Figure 1.8-11 Prior to the dephasing magnetic field pulse, all the spins are aligned. Upon diffusion and refocusing, each spin is dephased from their original position based on their rate of diffusion.

This is repeated multiple times keeping the delays constant but gradually increasing the gradient strength. The intensity of the signal can be described by equation 5, where δ and Δ are the timing constants, g is the gradient strength and D is the diffusion coefficient.

$$I = \exp\left[-(\gamma g \delta)^2 D\left(\Delta - \frac{\delta}{3}\right)\right] \qquad \textbf{Equation 1.8-20}$$

In order to obtain the diffusion coefficient distribution of the sample, CONTIN analysis was used. Developed by Stephen Provencher to solve complex or incomplete systems of linear equations, the technique uses inverse Laplace transforms to solve such equations[5]. In the case of DOSY, the intensity decay can

be described by a sum of exponential decay terms, one for each population in the system.

Using CONTIN analysis, we are able to measure multiple diffusion coefficients for the same chemical species, impossible to do with DLS. This allowed us to measure desorption of Pluronic-F127 from the surface of the nanoparticles following oxidation.

1.8.5 Appendix references

1 E. Zavoisky, *J. Phys.-USSR*, 1944, **8**, 377.

2 B. Commoner, J. Heise and J. Townsend, *Proc Natl Acad Sci U S A*, 1956, **42**, 710.

3 I. I. Rabi, S. Millman, P. Kusch and J. R. Zacharias, *Physical Review*, 1939, **55**, 526.

4 E. M. Purcell, H. C. Torrey and R. V. Pound, *Physical Review*, 1946, **69**, 37.

5 S. W. Provencher, *Computer Physics Communications*, 1982, **27**, 229.

2 Chemical specificity in REDOX-responsive materials: the diverse effects of different Reactive Oxygen Species (ROS) on polysulfide nanoparticles

Damien Jeanmaire[1], Jureerat Laliturai[1†], Abdulaziz Almalik[1§], Paolo Carampin[1], Richard d'Arcy[2], Enrique Lallana[2], Robert Evans[3¶], Richard Winpenny[4], Nicola Tirelli[2,3 *1]

[1] School of Pharmacy and Pharmaceutical Sciences, University of Manchester, Oxford Road, Manchester, M13 9PT, United Kingdom

[2] School of Medicine, Institute of Inflammation and Repair, University of Manchester, Oxford Road, Manchester, M13 9PT, United Kingdom

[3] School of Materials, University of Manchester, Oxford Road, Manchester, M13 9PL, United Kingdom

[4] School of Chemistry, University of Manchester, Brunswick Street, Manchester, M13 9PL, United Kingdom

* to whom correspondence should be addressed :

Prof. Nicola Tirelli, School of Materials and Institute of Inflammation and Repair / School of Medicine, University of Manchester, Oxford Road, Manchester, M13 9PT, United Kingdom

Tel.: +44 161 275 24 80.

Fax: +44 161 275 23 96

Email: nicola.tirelli@manchester.ac.uk

[1] **Author Contributions**: Jureerat Laliturai – solution polymerisation and initial particle synthesis with Br4, Abdulaziz Almalik – H_2O_2 and OCl- cell studies, Paolo Carampin – Initial linear polymerisation studies and TEM images, Richard d'Arcy – GPC measurements, Enrique Lallana – Helped with NMR analysis, Robert Evans – Helped with DOSY analysis, Richard Winpenny/Nicola Tirelli – Supervisors.

Abstract

REDOX responsive (nano)materials typically exhibit chemical changes in response to the presence and concentration of oxidants/reductants. Due to the complexity of biological environments, it is critical to ascertain whether the chemical response may depend on the chemical details of the stimulus, in addition to its REDOX potential, and whether chemically different responses can determine a different overall performance of the material.

Here, we have used oxidation-sensitive materials, although these considerations can be extended also to reducible ones. In particular, we have used poly(propylene sulfide) (PPS) nanoparticles coated with a PEGylated emulsifier (Pluronic F127); inter alia, we here present also an improved preparative method. The nanoparticles were exposed to two Reactive Oxygen Species (ROS) typically encountered in inflammatory reactions, hydrogen peroxide (H_2O_2) and hypochlorite (ClO^-); their response was evaluated with a variety of techniques, including diffusion NMR spectroscopy that allowed to separately characterize the chemically different colloidal species produced.

The two oxidants triggered a different chemical response: H_2O_2 converted sulfides to sulfoxides, while ClO^- partially oxidized them further to sulfones. The different chemistry correlated to a different material response: H_2O_2 increased the polarity of the nanoparticles, causing them to swell in water and to release the surface PEGylated emulsifier; the uncoated oxidized particles still exhibited very low toxicity. On the contrary, ClO^- rapidly converted the nanoparticles into water-soluble, depolymerized fragments with a significantly higher toxicity.

The take-home message is that it is more correct to discuss ‘smart’ materials in terms of an environmentally specific response to (REDOX) stimuli. Far from being a problem, this could open the way to more sophisticated and precisely targeted applications.

2.1 Introduction

Variations in REDOX potential can often be associated to specific biological environments and sometimes to pathological conditions[1,2], thus (nano)materials responding to REDOX-active species can be used to perform biological targeting. We are specifically interested in polymeric nanostructures responsive to oxidizing conditions, which are often a signature of inflammatory reactions [3,4]. A complete overview of this field is out of the scope of the present paper, but is provided by a number of very recent reviews [5–7]. In order to simplify a very complex chemical landscape, in a first approximation we can restrict the field of the biologically occurring, inflammation-related oxidants to only a few of the most common Reactive Oxygen Species (ROS): superoxide anion ($O_2^{\bullet-}$), hydrogen peroxide (H_2O_2) and hypochlorite (ClO^-)[8].

Our oxidation-sensitive units are hydrophobic organic polysulfides, in particular poly(propylene sulfide) (PPS), which we have previously produced in the form of PEG-containing block-copolymers to yield e.g. micelles[9] or vesicles[10], or as PEGylated and cross-linked polymeric nanoparticles[11]. Upon exposure to ROS, the sulfide groups can be converted to more polar and thus also more hydrophilic groups (sulfoxides, sulfones). This increase in polarity, leading to water ingress and swelling/solubilization, allows for responsive actions such as the ROS-stimulated release of encapsulated payloads [12,13]. However, as recently seen on linear polymers[14], the details of polysulfide oxidation are difficult to explain simply on the basis of a scale of standard reduction potentials. Using water as a final product and a neutral pH, the order of reactivity would be predicted to be $O_2^{\bullet-}$ >H_2O_2> ClO^- ($O_2^{\bullet-}$- H_2O_2: 0.94 V[15,16]; H_2O_2 - H_2O: 1.32[15] V, 1.77 V[17]; ClO^- - Cl^-/H_2O 1.08 V [18]), ; on the contrary, a) polysulfides are largely unresponsive to superoxide[19], b) oxidation leads to sulfur (IV) (sulfoxides) with H_2O_2 [14], while c) hypochlorite produces both sulfoxide and sulfur (VI) (sulfone)-containing structures which cause the depolymerisation of the polysulfides[14]. Therefore factors other than the pure REDOX potential are probably critical in

determining the responsiveness of these materials to oxidizing condition, *e.g.* the solubility of the oxidant in the polysulfide domain.

Here, we have examined the effects of H_2O_2- and hypochlorite-mediated oxidation on cross-linked polysulfide nanoparticles, a class of particles recently used also for vaccine delivery purposes[20–22], predominantly focusing on the characterization of the structural effects arising from their exposure to the two ROS.

PPS nanoparticles are prepared by combining the emulsion anionic ring-opening polymerization of episulfides[23] and a cross-linking based on the reactivity of the PPS terminal thiolate groups[11]. For a detailed review of preparative methods for such polysulfide structures, the reader can refer to a specific review[24], while here we rapidly summarize this template preparative method: a) propylene sulfide (PS) is dispersed in water by the use of a PEGylated emulsifier (generally Pluronic F127) to create droplets sized from tens to hundreds of nm (modulated by the emulsifier-to-monomer ratio); b) PS polymerization and cross-linking convert the droplets into stable hydrophobic nanoparticles, which are coated by physically but irreversibly entrapped Pluronic (Scheme 2.1-1, top left)[25], where its poly(propylene glycol) (PPG) middle block remains entangled in the PPS network. The template character of the method allows to precisely control the size of the nanoparticles using different monomer/emulsifier ratios (Scheme 2.1-1, top right).

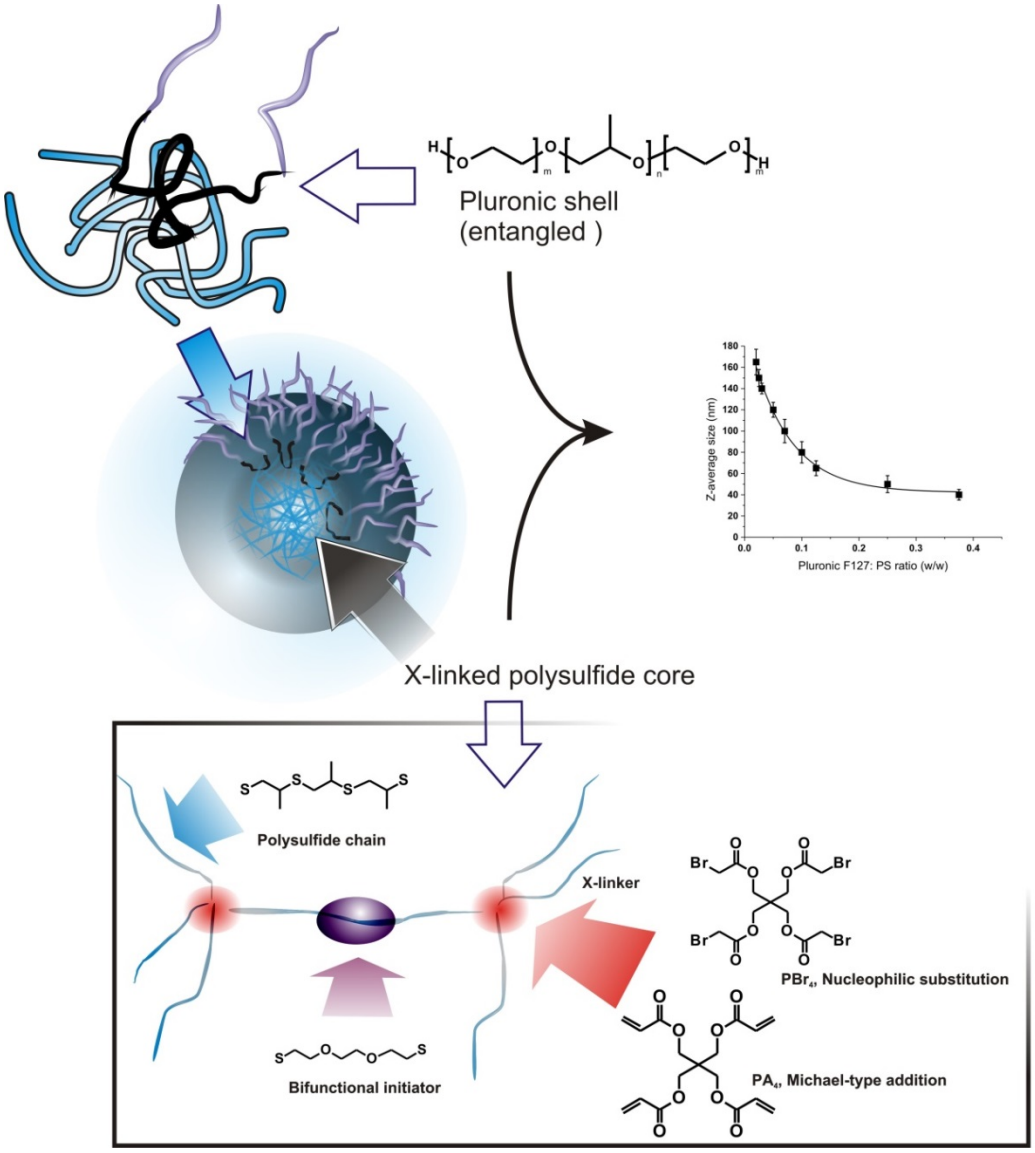

Scheme 2.1-1 Polysulfide nanoparticles can be prepared via emulsification of PS (Pluronic F127 as PEGylated emulsifier) followed by its polymerization using a bifunctional initiator. The resulting bifunctional PPS chains are then reacted with tetrafunctional cross-linkers: PBr_4 and PA_4. The hydrophobic PPG block is retained in the network, stabilizing the Pluronic surface layer and providing a permanent PEGylated surface; the dimensions of the nanoparticles are templated on those of the emulsion droplets, which depend on the Pluronic/PS ratio (inset graphic; PPS of *overall DP* = 50, PA_4 as a cross-linker (n = 3)).

In previous studies, we have employed tetrafunctional initiators (in form of thioacetates) to yield tetra-armed star polymers that were eventually cross-linked with difunctional end-cappers, e.g. divinyl sulfone or a diacrylate. Thioacetates allow to minimize the presence of disulfides, which act as chain

transfer agents in the episulfide polymerization and compromise the control over molecular weight and end groups[26]. This procedure, however, is rather cumbersome, since it requires the synthesis and purification of a protected initiator and also an additional deprotection step prior to polymerization.

Here, we have simplified the nanoparticle preparation, adopting a specular synthetic approach based on a difunctional initiator and tetrafunctional end-cappers. As initiator, we have employed 2,2'-(ethylenedioxy)diethanethiol, which has a low propensity of intramolecular disulfide formation, due both to the low local density of thiol groups (lower than e.g. tetrathiols) and the impossibility to form stable 5- or 6-membered rings, as for 1,3-propanedithiol[23]. As tetrafunctional end-cappers, we have evaluated pentaerythritol tetraacrylate (PA_4) and tetrabromoacetate (PBr_4), which respectively react with PPS terminal thiols through Michael-type addition and nucleophilic substitution (Scheme 2.1-1, bottom). We have first applied this procedure to the synthesis of linear polymers (using monofunctional end-cappers), in order to ensure that the polymerization still preserves a controlled character, i.e. the polymers have an acceptably narrow molecular weight distribution. This point is essential to ensure that the final networks have a homogeneous cross-link density (= polymer chains with controlled molecular weight between cross-links).

2.2 Experimental Section

2.2.1 Materials

All chemicals were used as received from suppliers unless otherwise stated. Propylene sulfide (PS), pentaerythritol tetraacrylate (PA_4), Nile Red, triethylamine (TEA), Pluronic F127, sodium hypochlorite (NaOCl) in aqueous solution (available chlorine 10-15 %), pentaerythritol, ethyl 2-bromoacetate, 2,2'-(ethylenedioxy)diethanethiol and fungizone were purchased from Sigma-Aldrich (Gillingham, UK). Dichloromethane, acetonitrile and 30% wt. H_2O_2 in water were purchased from BDH (Leicestershire, UK). Bromoacetyl bromide and

1,8-diazabicyclo[5.4.0]undec-7-ene (DBU) were purchased from Fluka (Gillingham, UK). Phosphate buffered saline (PBS) Dulbecco A tablets were purchased from Oxoid (Hampshire, UK). Dulbecco's modified Eagle's medium (DMEM), foetal bovine serum (FBS), L-glutamine 200 mM (x100) and penicillin-streptomycin were purchased from Invitrogen (Paisley, UK). CellTiter 96® AQ_{ueous} One Solution Cell Proliferation Assay was purchased from Promega (Southampton, UK). All other chemicals were of analytical grade and used without further purification.

2.2.2 Physico-chemical characterization

^1H NMR spectra were recorded on 1% wt. solutions in deuterated chloroform using a 300 MHz Bruker spectrometer (Bruker UK Limited, UK). FT-IR spectra were recorded in ATR mode (Golden Gate) on a Tensor 27 Bruker spectrometer (Bruker UK Limited, UK) equipped with a 3000 Series TM High Stability Temperature Controller with RS232 Control (Specac, UK). The spectra of nanoparticles upon oxidation with H_2O_2 or NaOCl were recorded by allowing a drop of the oxidation mixture (typically 20-50 μL) to dry at 50 °C for ca. 3 min on the bottom plate of the Golden Gate ATR accessory. Turbidity measurements were performed by monitoring the optical density of nanoparticle dispersions at 600 nm using a UV/Vis spectrophotometer Perkin Elmer Lambda 25 (Perkin Elmer, UK). Nile Red fluorescence was measured through a Perkin Elmer LS 55 (Perkin Elmer, UK) at a temperature of 25°C (excitation 540 nm, emission at 620 nm). *Gel permeation chromatography (GPC):* *M*olecular weight and molecular weight distribution of polymers were determined using a Polymer Laboratories PL-GPC50 integrated GPC (Polymer Laboratories, UK) comprising a PLgel 5 μm Guard and two PolyPore 5 μm columns operating online at 30 °C. THF was used as an eluent at a flow rate of 1.0 mL/min. A series of near-mono-dispersed linear polystyrene standards (Fluka; Gillingham, UK) was used for calibration with a refractive index detector for the analysis of the polymers.

Dynamic light scattering (DLS). Size distributions and scattering intensity of nanoparticles were measured with the help of a Zetasizer Nano ZS Instrument

(Model ZEN3500, Malvern Instruments Ltd, UK). All the samples were analyzed at an angle of 173° and a temperature of 25°C.

Pulsed field gradient NMR spectroscopy (PFG NMR, also referred to as diffusion-ordered NMR spectroscopy (DOSY)[27]. Diffusion NMR data were acquired on a Bruker Avance II 400 MHz spectrometer, without spinning, using a 5 mm insert probe equipped with a gradient coil producing a maximum gradient strength of 1190 G cm^{-1}. All experiments were carried out with active temperature regulation at 25.0 °C. ^{1}H spectra of the samples were acquired with a simple pulse-acquire sequence, recording 32 transients. DOSY data were acquired using a One-Shot[28] sequence.

Transmission electron microscopy (TEM). Nanoparticle dispersions were pipetted on carbon/formvar coated copper 100 mesh grids and left for 2-3 min; the grids were then washed in distilled water for 3 times, stained with 1% uranyl acetate and air dried. Samples were observed using a Technai 12 electron microscope at 100kV.

2.2.3 Preparative operations

Synthesis of linear polysulfides. Both the polymerization experiments described hereafter and the nanoparticle preparations were conducted in 50 mL round-bottom flasks under magnetic agitation. However, analogous experiments were also conducted at a larger scale (typically 3 mL of monomer), using 150 mL vessels in a Tornado parallel reactor (Radleys, UK) under mechanical stirring (1,000 rpm). Reagents were introduced in argon purged reaction flasks and polymerizations were carried out always under a positive argon pressure. Degassed MilliQ water (argon bubbling for 1 h) was used for polymerizations. 0.15 g of Pluronic F127 ($\overline{M_n}$ ≈ 12,600 g/mol) was dissolved in 75 mL of degassed MilliQ water (0.2% wt.) in a 250 mL three-neck round bottom flask under argon. The system was continuously stirred at 1,000 rpm and purged with argon for 1 h. PS (3.17 mL, 3.0 g, 40.4 mmol) was mixed with an appropriate amount of 2,2'-(ethylenedioxy)diethanethiol (0.246, 0.148, 0.105, 0.082 g, respectively, providing monomer to initiator ratios corresponding to *overall DP* = 30, 50, 70 and 90, and *DP per arm* = 15, 25, 35 and 45), the mixture was then added to the

Pluronic F127 solution and stirred for another 10 min, followed by the addition of 2.2 equivalents compared to initiator of DBU (0.451, 0.271, 0.194, 0.151 g respectively). The reaction mixture was stirred for 2 h, then the pH was lowered to 9.5 by the addition of acetic acid, and 1.5 equivalents of ethyl 2-bromoacetate (0.676, 0.405, 0.290 0.225 g respectively) were finally added. After 1 minute the pH was brought to 7.4 by adding 5 mL of PBS (50 mM, pH 7.4), in order to minimize the hydrolysis of the end-capper. The mixture was additionally stirred for 1 h before the addition of 20 mL of dichloromethane; the organic phase was decanted and washed with brine three times. The organic layer was dried over Na_2SO_4 and evaporated under vacuum. The resulting oily material was further washed with methanol (3x5 mL), separated by decantation after centrifugation, and dried under high vacuum for 24 h at 40°C.

^{1}H NMR ($CDCl_3$); δ = 1.26–1.30 (t, 6H, C**H$_3$**CH_2–OOC–), 1.35–1.45 (d, C**H$_3$** in PPS chain), 2.55–2.75 (m, PPS chain: 1 diastereotopic C**H$_2$**), 2.71–2.78 (t, 4H, –SC**H$_2$**CH_2OCH_2CH_2OCH_2C**H$_2$**S–), 2.85-3.05 (m, PPS chain: C**H** and 1 diastereotopic C**H$_2$**), 3.16-3.25 (d, 2H, –S–C**H$_2$**–COO–: 1 diastereotopic C**H$_2$**), 3.25-3.37 (d, 2H, –S–C**H$_2$**–COO–: 1 diastereotopic C**H$_2$**), 3.61–3.68 (m, 8H, –SCH_2C**H$_2$**-OC**H$_2$**C**H$_2$**OC**H$_2$**CH_2S–), 4.15–4.26 ppm (q, 4H, CH_3C**H$_2$**–O(O)C–).

ATR FT-IR (thin film); 2959 (ν_{as} CH_3), 2917 (ν_{as} CH_2), 2865 (ν_s CH_3 and ν_s CH_2), 1730 (ν C=O ester), 1448 (δ_s CH_2), 1372, 1263, 1221, 1172, 1103 (ν_{as} C-O-C), 943, 852 cm^{-1} (ν_s C–O–C).

Representative ^{1}H NMR and IR spectra are provided in Supporting Information, Figure 2.7-SI-8 and Figure 2.7-SI-9.

Preparation of multifunctional cross-linkers. Pentaerythritol tetrakis(2-bromoacetate) (*PBr_4*). Pentaerythritol (1 g, 7.3 mmol) and TEA (8.2 mL, 5.9 g, 58.7 mmol) were sequentially introduced into a 250 mL three-neck round bottom flask containing 40 mL of acetonitrile under an argon atmosphere. The solution was then cooled down to 0ºC, and 6.0 equivalents of bromoacetyl bromide (3.8 mL, 8.80 g, 43.6 mmol) diluted in acetonitrile (5 mL) were added in a dropwise fashion over 1 h. The reaction mixture was then allowed to reach

room temperature and stirred overnight. Afterwards, the formed TEABr precipitate was removed by filtration, and the filtrate was concentrated in a rotary evaporator. The resulting viscous liquid was purified via flash column chromatography on silica gel (230-400 mesh) with a first elution in dichloromethane/ethyl acetate (40:1) and a second one in pure dichloromethane. Yield: 75% wt. (3.39 g, 5.5 mmol; 100% esterification of OH groups by ^{1}H NMR).^{1}H NMR ($CDCl_3$); δ = 3.86 (s, 8H, -O-COC**H**$_2$-Br), 4.28 ppm (s, 8H, -C-C**H**$_2$-O-CO-). Pentaerythritol tetraacrylate (*PA$_4$*). PA_4 is commercially available (Sigma Aldrich) and was purified by flash column chromatography on silica gel (230-400 mesh) with dichloromethane/ethyl acetate (10:1) as a mobile phase. Butylated hydroxytoluene (BHT; 3,5-di-*tert*-butyl-4-hydroxytoluene) was then added (800 ppm) and the resulting waxy solid was stored under Ar at -20°C. ^{1}H NMR ($CDCl_3$); δ = 4.27 (s, 8H, -C-C**H**$_2$-O-CO-), 5.86 (dd, 4H, -O-COCH=C**H$_2$**: *cis*-H), 6.09 (dd, 4H, -O-COC**H**=CH_2), 6.39 ppm (dd, 4H, -O-COCH=C**H$_2$**: *trans*-H).

Preparation of cross-linked nanoparticles. 20 mg of Pluronic F127 were dissolved in 25 mL of degassed MilliQ water (0.08% wt.; for studies of particle size Pluronic F127 concentrations ranging between 0.08 and 1.5% wt. were used; the targeted *overall DP* was set at 50) in a 50 mL three-neck round bottom flask. The system was continuously stirred at 1,000 rpm for 10 min under an argon atmosphere. Then, 2,2'-(ethylenedioxy)diethanethiol (0.047 g, 0.256 mmol) and PS (1.0 mL, 0.95 g, 12.8 mmol, corresponding to 25 PS equivalents per thiol group; *overall DP* = 50) were added, the reaction mixture was further stirred for 10 min, and 2 equivalents of DBU (0.076 µL, 0.078 g, 0.512 mmol) were finally added to initiate the polymerization. The reaction mixture was stirred under inert conditions for 2 h; the pH was lowered to 9.5 by the addition of acetic acid, and 0.5 equivalents of the desired tetrafunctional cross-linker (0.128 mmol, corresponding to 79.3 mg of PBr_4 or 45.1 mg of PA_4) dissolved in dichloromethane (0.3 mL) were then added to the reaction mixture. After 1 minute the pH was brought to 7.4 by adding 5 mL of PBS (50 mM, pH 7.4), in order to minimize the hydrolysis of the cross-linkers. The suspension was additionally stirred for 16 h before purification by ultrafiltration (Amicon Ultrafiltration Cell Model 8200, Millipore, UK) against

MilliQ water through 300 kDa MWCO regenerated cellulose membranes (Spectrum Laboratories, UK). For any further use, the concentration of nanoparticles was determined gravimetrically after freeze drying samples of their dispersions. ATR FT-IR (thin film): 2958 (ν_s CH_3), 2914 (ν_{as} CH_2), 2864 (ν_s CH_3), 1745 (ν C=O), 1246 (ν_{as} C-O-C, ester), 1097 (ν_{as} C-O-C in Pluronic F-127), 800-600 cm^{-1} (ν C-S in PPS).

Loading of Nile Red in nanoparticles. The above preparative procedure was modified by dissolving Nile Red (1.63 or 0.163 mg, respectively corresponding to 5.12 and 0.512 μmol) in the cross-linker dichloromethane solution (respectively, 1:2500 and 1:25000 Nile Red/thioether molar ratio) and adding it to the reaction mixture. The fluorescence emission of Nile Red in different possible environments was monitored at 620 nm (excitation in the window 540 ± 25 nm, emission in the window 620 ± 40 nm).

2.2.4 Oxidation of nanoparticles

A) DLS and fluorescence analysis. Experiments were carried out with PA_4 or PBr_4 nanoparticles obtained using a 0.02 Pluronic/PS weight ratio (*overall DP* = targeted molecular weight between cross-links = 50, corresponding to *DP per arm* = 25) prepared as described above and with a Z-average size of 160 nm. 1 mL of nanoparticle dispersion in deionized water (concentration ≈ 3.5 mg/mL = 0.35 % wt.) was added to 10 mL of an aqueous solution of H_2O_2 or NaOCl (of an adequate concentration) and adjusted to pH = 7.4 by the addition of concentrated NaOH (aq), to obtain a final concentration of ≈ 0.32 mg/mL of nanoparticles (= 4.3 mM in thioethers); the reaction was allowed to proceed at 37ºC monitoring the time-dependent changes in turbidity (optical density at a wavelength of 600 nm), particle size (DLS) and Nile Red fluorescence (at 620 nm). Please note that Nile Red's absorption maximum shifts considerably from hydrophobic to polar environments (e.g. from below 500 nm in alkanes to about 530 in alcohols), and the same applies to its emission maximum; therefore, we have chosen spectral parameters (excitation at 540 nm, emission at 620 nm) that provide the highest readings in polar environments with low water content, and negligible fluorescence both in apolar polysulfides and in water-swollen

environments.

B) NMR analysis. Experiments were carried out on PA_4 nanoparticles obtained using 0.02 and 0.2 Pluronic/PS weight ratio (*overall DP* = targeted molecular weight between cross-links = 50, corresponding to *DP per arm* = 25) prepared as described above and with a Z-average size respectively of 160 and 50 nm. Due to the relatively low sensitivity of the technique when working with cross-linked polymers, the nanoparticle concentrations employed for these experiments were considerably larger than for DLS, turbidity or fluorescence experiments. *Diffusion NMR.* For diffusion experiments, 200 μL of 10% or 30% wt. H_2O_2 or 268 mM NaOCl were added to 200 μL of a 20 mg/mL nanoparticle dispersion in deionized water to obtain a final concentration of 10 mg/mL of nanoparticles (= 134 mM in thioethers). The reaction was allowed to proceed at room temperature for six hours. 100 μL of D_2O were then added to the dispersion prior to NMR analysis. For T_2 relaxivity experiments, similar conditions were used (200 μL of 10% wt. H_2O_2 to yield a final 5% wt. H_2O_2). The experiments were conducted acquiring 256 transients, and using a diffusion delay Δ of 0.01 s and 0.02 s, respectively, and a total diffusion encoding time δ of 0.001 s. 20 gradient levels were acquired, in equal steps of gradient squared from 119 to 890 G cm^{-1}. The maximum gradient was chosen so that ~75% of the polymer signal (methyl group at δ = 1.47 ppm for PPS, ethylene group at δ = 3.77 ppm and methyl group at δ = 1.19 ppm for Pluronic F127) was attenuated. Due to the broad peaks present in the nanoparticle spectra, neither resolution enhancement nor reference deconvolution was used. *T_2 spin-spin relaxation measurements.* T_2 measurements were performed on nanoparticle dispersions in 90% H_2O and 10% D_2O using a 400 MHz Bruker spectrometer (Bruker UK Limited, UK). The pulse sequence used was the Carr-Purcell-Meiboom-Gill (CPMG) sequence.

2.2.5 Cell culture

L929 mouse fibroblasts were obtained from the European Collection of Animal Cell Cultures (ECACC, Rockville, UK). Cells were routinely maintained in a culture medium composed of DMEM supplemented with 10% v/v FBS, 2 mM L-glutamine, 1% v/v fungizone and 0.5% v/v penicillin-streptomycin, growing them

as a confluent monolayer culture in 75 cm^2 polystyrene flasks (Falcon, Oxford, UK) and changing the medium 3 times a week. Cell cultures were maintained at 37ºC in a humidified atmosphere of 5% CO_2. Adherent cells approaching 90% confluence were harvested with trypsin and subcultured. Passages were always below 6. The semi-adherent J774.2 murine macrophages were also obtained from ECACC. Cells were routinely maintained in DMEM supplemented with 10% v/v FBS, 2 mM L-glutamine, penicillin G (100 units/mL), streptomycin sulfate (0.1 mg/mL) and amphotericin B (0.25 µg/mL), and cultured in 75 cm^2 polystyrene flasks at 37ºC in a humidified atmosphere of 5% CO_2. Subcultures were obtained every 2 or 3 days by scraping with a rubber policeman, and re-suspended in new cell culture medium. For all experiments, the cells were subjected to no more than 20 cell passages. *Preparation of test materials*: purified pristine PA_4 or PBr_4 nanoparticles (0.02 Pluronic/PS weight ratio; purification via ultrafiltration as previously described; concentration around 40 mg/mL in deionized water) were diluted with cell culture medium to reach the desired final concentration. Oxidized nanoparticles (15% wt. H_2O_2 or 10 mM NaClO, as previously described but on a 20x scale) were purified and concentrated via ultrafiltration using membranes with 1 kDa MWCO; when the concentration of the suspensions (monitored by collecting samples and recording their weight after freeze drying) was in proximity of 40 mg/mL, they were diluted with culture medium to reach the desired final concentration.

Cytotoxicity tests: L929 mouse fibroblasts and J774.2 mouse macrophages were plated at a density of 8,000 cells/well in 96-well plates at 37ºC in 5% CO_2 atmosphere. After 24 h of culture, the medium in the wells was replaced with fresh medium containing variable amounts of a 0.45 µm sterile-filtered PA_4 nanoparticle dispersion, or hypochlorite, or 1.25 mM hypochlorite with variable concentrations of nanoparticles. After 48 h of incubation, the medium was removed, and the cells were rinsed twice with PBS (pH 7.4). Later, a mixture containing culture medium (without FBS and phenol red) and MTS proliferation assay solution (CellTiter 96® AQ_{ueous} One Solution Cell Proliferation Assay) was added into each well. After 3 h, the quantity of formazan produced was

evaluated from its absorbance at 490 nm using a Synergy2 Biotek plate reader with Gen5 software. The measured absorbance is proportional to both the number and the metabolic activity of the living cells in culture; in order to obtain values predominantly linked to the metabolic (mitochondrial) activity, the absorbance readings were normalised against the total protein content obtained using the Quantipro BCA assay kit, which is roughly supposed to be proportional to the number of cells: the cells were washed with PBS, and incubated for 15 min, in 100 mL cell lysis buffer (0.5%triton X-100 in PBS), to which 100 mL of Quantipro solution (prepared following the instructions of the manufacturer) was added. The absorbance at 562 nm was finally recorded after 2 hours incubation at 37°C.

2.3 Results and Discussion

2.3.1 Synthesis of model polymers and of nanoparticles

We have first confirmed that the simplified preparative method (dithiol + tetrafunctional end-capper vs. the previously used tetrathioacetate + difunctional end-capper) still offered a sufficient control over molecular weight to allow for homogeneous networks (→ homogeneous diffusion of oxidants): a series of linear polymers was prepared by this emulsion polymerization approach, and GPC, ^{1}H NMR and FT-IR analysis showed a reasonably good agreement between experimental and theoretical degrees of polymerization (Figure 2.3-1 and Table 2.3-1). A significant discrepancy between theoretical and spectroscopic values could be seen only at the lowest initiator/monomer ratio (DP = 90), likely due to incomplete polymerization because of the slower polymerization kinetics. The molecular weight dispersity of these model linear polymers is clearly larger than when the disulfide presence is carefully avoided (1.4 - 1.6 vs. ≈ 1.1 with protected initiators and *in situ* reducing agents); indeed a high MW shoulder can be easily spotted in the GPC traces (Figure 2.3-1, left): this is typical of polymers with internal disulfides that are a clear visual marker of disulfide-mediated chain transfer activity [26]. However, this effect is quantitatively

small and we judged the new synthetic method appropriate for the preparation of reasonably controlled cross-linked nanoparticles.

Nanoparticles were therefore prepared by synthesizing a difunctional PPS with overall *DP* = 50, and using two different tetrafunctional end-cappers, pentaerythritol tetraacrylate (PA_4) and pentaerythritol tetrakis(2-bromoacetate) (PBr_4) (Scheme 2.1-1), in order to investigate possible effects of different cross-linking mechanisms. Often PBr_4 yielded slightly smaller nanoparticles but with a larger variability in size than PA_4, and among the two we could not detect any statistically relevant difference. Importantly, PPS nanoparticles showed an excellent physical stability, e.g. no agglomeration upon storage (1 mg/mL in water; >3 months at room temperature) or freeze-drying (using sucrose as a cryoprotectant; see Supporting Information, Figure 2.7-SI-10).

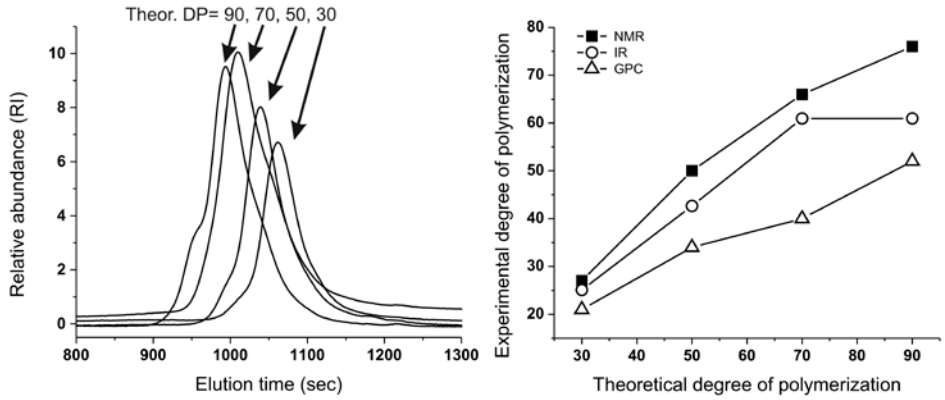

Figure 2.3-1 ***Left*****:** GPC traces showing that the emulsion synthesis of linear PPS from the difunctional initiator 2,2'-(ethylenedioxy)diethanethiol produces polymers (with different DPs) with acceptable molecular weight distributions and relatively small amounts of disulfide impurities: the latter are recognizable because of the presence of a "dimer peak", i.e. a higher molecular weight shoulder of the GPC trace[26]. ***Right*****:** Experimental vs. theoretical number average DP of linear, difunctional PPS via "unprotected" emulsion polymerization: although numerically different, the results of ^{1}H NMR, FT-IR and GPC clearly showed the proportionality between the theoretical DP (PS/initiator molar ratio in the feed) and that of the actual polymers, which demonstrates the good control of PS polymerization initiated by 2,2'-(ethylenedioxy)diethanethiol, even without the use of thiol protecting groups (e.g. as thioacetate). For typical NMR and FT-IR spectra, see Supporting Information, Figures 1SI and 2SI, respectively. Please realize that the discrepancy between GPC and spectroscopic results is probably to ascribe to the use of single detection in the GPC measurements.

Table 2.3-1 Physico-chemical characterization of linear PPS initiated by 2,2'-(ethylenedioxy)diethanethiol in emulsion and end-capped with ethyl 2-bromoacetate. Please note that *overall DP* = monomer/initiator molar ratio, which is twice the *DP per arm* of the bifunctional macromolecules.

Theoretical *overall DP*	^{1}H NMR		GPC			FT-IR
	Overall DP [a]	End-capping [b] (mol %)	$\overline{M_n}$ [c]	$\overline{M_w}/\overline{M_n}$ [c]	*Overall DP*	Relative DP [d]
30	27 ± 1	89	1900	1.39	25 ± 1	27 ± 2
50	50 ± 1	84	2900	1.48	37 ± 3	45 ± 3
70	66 ± 1	80	3300	1.61	45 ± 2	67 ± 6
90	76 ± 4	86	4200	1.51	60 ± 3	69 ± 6

[a] Calculated from the ratio between the integrals of protons of the PPS chain (CH_3, 1.35-1.45 ppm) and of the initiator (–$SCH_2C\mathbf{H_2}$-$OC\mathbf{H_2}C\mathbf{H_2}OC\mathbf{H_2}CH_2S$–, 3.61–3.68 ppm). Average values over three different polymerization experiments. For a representative DP, see Supporting Information, Figure 2.7-SI-8.

[b] Calculated from the ratio between the integrals of protons of the PPS chain (CH_3, 1.35-1.45 ppm) and of the end-capper ($OC\mathbf{H_2}CH_3$, δ = 4.15–4.26 ppm). Average values over three different polymerization experiments.

[c] Average values over three different polymerization experiments.

[d] Calculated using the integral of the peak at 1130 cm^{-1} (fingerprint region peak associated to the PPS chain; the area between 1080 and 1200 cm^{-1} was fitted with four Gaussian peaks to depurate the absorbance readings from the contribution of neighboring peaks) and that of the C=O stretching peak at 1735 cm^{-1} (proportional to the amount of end-capper); these figures are supposedly related to the degree of polymerization assuming a constant end-capping yield. The data were normalized assuming a DP = 27 for PPS with a theoretical DP = 30 (i.e. using the DP calculated through ^{1}H NMR for that sample). FT-IR spectra of the different polymers can be found in Supporting Information, Figure 2.7-SI-9. Average values over three different polymerization experiments

2.3.2 Nanoparticle response to hydrogen peroxide

H_2O_2 caused nanoparticles to swell, independently on the nature of the cross-linker. The turbidity of the nanoparticle suspensions decreased (Figure 2.3-2A) at a rate proportional to the oxidant concentration (Figure 2.3-2B) and their size

increased with identical kinetics (Figure 2.3-2B, empty circles). It is important to note that all curves showed the sigmoidal shape typical of auto-accelerating phenomena: the poor solubility of H_2O_2 in the originally hydrophobic matrix is reflected by a lag phase (a “toe” region), followed by an accelerating phase due to the better solubility of the oxidant in the increasingly polar material [3].

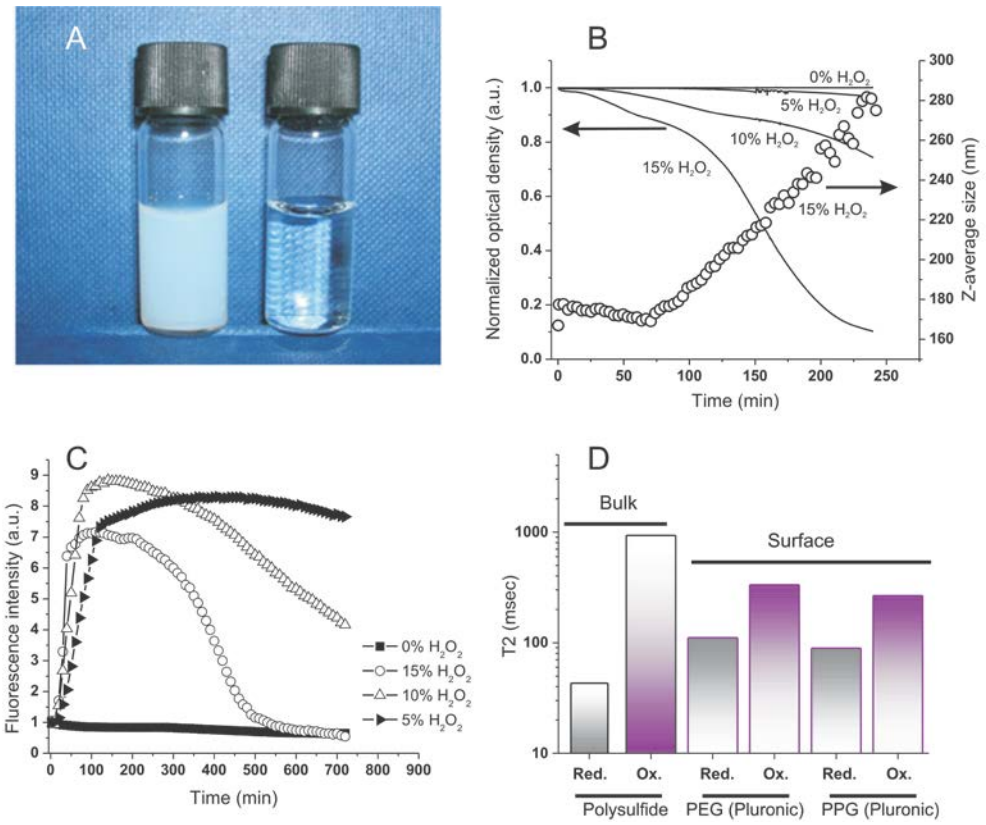

Figure 2.3-2 Oxidation of PA_4 nanoparticles (Z-average size: 160 nm); 0.32 mg/mL in deionized water, 37 ºC and pH = 7.4. ***A*:** Appearance of the nanoparticle dispersion before and after oxidation with 15% wt. H_2O_2. ***B*:** Optical density at 600 nm (solid lines) and Z-average size (open circles) of nanoparticle dispersion vs. H_2O_2 concentration and time. The nanoparticle response was marginally affected by the nature of the cross-linker (compare with Figure 2.7-SI-13A in Supporting Information; see also the similarities in Figures 4SI and 5SI), although PBr_4 particles may undergo a more significant hydrolytical degradation during oxidation. ***C*:** Fluorescence emission intensity of Nile Red-loaded nanoparticles (excitation at 540 nm, emission at 620 nm; 1:2500 Nile Red/thioether molar ratio) vs. H_2O_2 concentration and time. The initial emission intensity is virtually zero due to the choice of the spectral parameters (see text). Similar results were obtained with two largely different Nile Red loadings, excluding therefore any influence of self-quenching effects (see Supporting Information, Figure 2.7-SI-12); PBr_4 cross-linked particles appeared to show a marginally quicker first phase, but the effect was not statistically significant (Figure 2.7-SI-12). ***D*:** T_2 Relaxivity of polysulfide (bulk) and Pluronic (surface) resonances before and after oxidation with 5% wt. H_2O_2 at room temperature for 3 h; see Table 2.7-SI-2 in Supporting Information for numerical values.

Infrared spectra showed that sulfoxide (S=O) groups were the only major feature introduced during this oxidation, as already shown on soluble polymers [14] (stretching vibration peak at 1030 cm^{-1}; see Supporting Information, Figure

2.7-SI-11); they could be detected only after the initial "toe" region (= the time window with relatively little changes) seen in turbidity and Dynamic Light Scattering (DLS) measurements (Figure 2.3-2B).

The polarity of the nanoparticle bulk was monitored via the fluorescence of Nile Red; taking advantage of the solvatochromic shifts of this dye, we have chosen an excitation wavelength (540 nm) that provides negligible emission (620 nm) in a very apolar environment and high fluorescence in moderately polar ones. This allowed to identify a major increase in the nanoparticle polarity (increase in emission) during the "toe" region, before significant swelling (water intake) occurred and caused fluorescence quenching (Figure 2.3-2C); therefore, it would appear some minor oxidative processes to have taken place also in the initial phases of the exposure to H_2O_2, although not sufficient to produce significant water ingress.

The ingress of water was further confirmed by a dramatic increase of the network molecular mobility after oxidation, as witnessed by a >20-fold increase in the spin-spin relaxation time (T_2) of the polysulfide chains (Figure 2.3-2D; see also Supporting Information, Table 1SI); interestingly, also the Pluronic protons showed a significant (3-fold) increase in T_2 values both in the hydrophilic (PEG) and in the hydrophobic (PPG) domains, which would suggest a mobilization also of these water-exposed groups.

To further investigate these transformations we have employed diffusion NMR spectroscopy. This technique has a precision comparable to DLS (Figure 2.3-3), but is chemically selective; for example, it confirms the presence of Pluronic on the surface non-oxidized nanoparticles[25], since the diffusion coefficients associated to both Pluronic and polysulfide resonances are virtually identical, but much different from that of Pluronic in micellar dispersion or in solution.

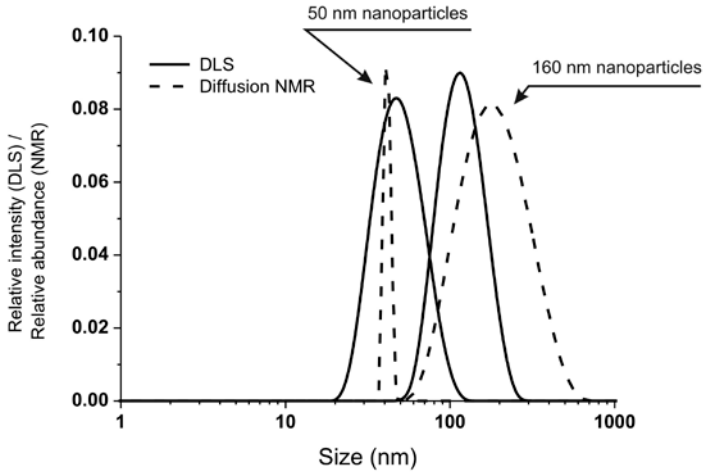

Figure 2.3-3 Comparison of size distributions obtained via DLS (solid lines) and diffusion NMR (dashed lines) for two differently sized nanoparticle preparations. Please note that the two techniques provide intensity (DLS) and number (NMR) distributions; considering this, the agreement between the two sets of measurements is remarkable.

The exposure of 50 nm nanoparticles to 5% wt. H_2O_2 for 6 hours caused roughly 50% oxidation of the sulfide groups (see the broadening of the methyl group resonance highlighted by an arrow in Figure 2.3-4A), which was accompanied by dramatic changes in DOSY spectra (Figure 2.3-4B and C). Before oxidation all resonances presented the same diffusion coefficient, indicating the close association between Pluronic and polysulfides (Figure 2.3-4C); after oxidation Pluronic displayed a much larger diffusion coefficient, which is easy to relate to 10-20 nm micelles (Figure 2.3-4D, purple curve). The increase in mobility associated to the transition from a compressed surface-entrapped state to a micellar one explains why also the hydrophilic PEG blocks showed a decrease in T_2 upon oxidation.

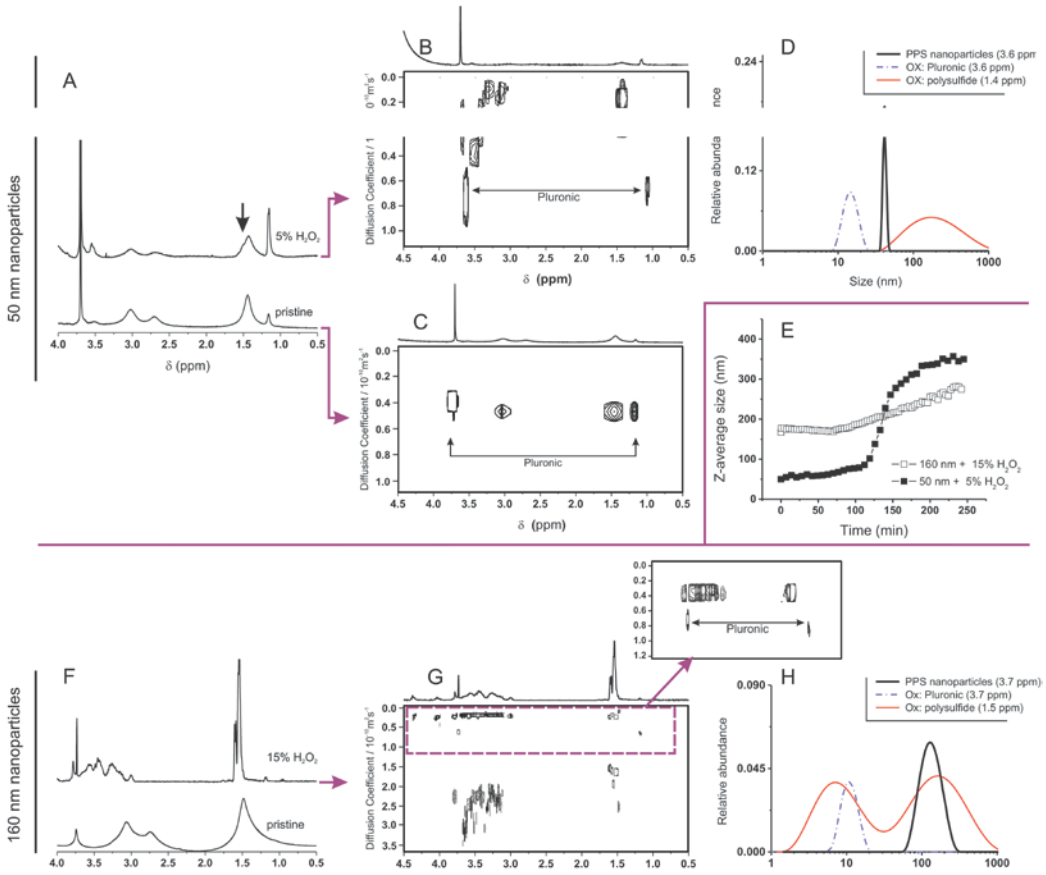

Figure 2.3-4 ***A, F:*** ^{1}H NMR spectra of 160 nm (A) and 50 nm (F) PA_4 nanoparticles (10 mg/mL) recorded before and after 6 h exposure to 15% (A), or 5% wt. H_2O_2 (F). ***B, C and G.*** DOSY spectra of pristine nanoparticles (C; 160 nm nanoparticles show a similar but more noisy pattern, due to the very low relative intensity of Pluronic resonances -results not shown-) and after oxidation (B and G). Please note the larger scale of diffusion coefficients in G; the inset allows a better appreciation of the larger species ($D<1*10^{-10}$ m^2s^{-1}). ***D and H.*** Size distributions obtained by applying a CONTIN algorithm to DOSY data. For the pristine nanoparticles (black lines), the size distributions obtained using the polysulfide and the Pluronic signals overlap (only Pluronic signal showed). ***E:*** Z-average size (DLS) of 160 nm and 50 nm nanoparticles (10 mg/mL) during their oxidation with different H_2O_2 concentrations as a function of time. Please note that the oxidation of 160 nm nanoparticles with 5% wt. H_2O_2 proceeds very slowly in this time window (see Figure 2.3-1 B), while that of 50 nm nanoparticles with 15% wt. H_2O_2 is too rapid to be easily monitored.

Further, the Pluronic loss from the nanoparticle surface is likely to cause aggregation in the yet not completely oxidized nanoparticles, which explains the presence of objects with a size too large (up to 1 μm) to be due only to swelling (Figure 2.3-4D, red curve).

We have also analyzed the diffusion behavior of nanoparticles with different size, because their dimensions may influence the rapidity of the oxidation response: indeed, 50 nm nanoparticles treated with a lower amount of H_2O_2 increased in size (swelled) more rapidly than 160 nm nanoparticles with a larger excess of the oxidant (5% wt. H_2O_2, ≈ 10-fold stoichiometric excess vs. thioethers as opposed to 15% wt. H_2O_2, ≈ 30-fold stoichiometric excess, Figure 2.3-4E). The accelerated response of the smaller colloids is likely due to a kinetic effect: their higher surface/volume ratio would allow a more rapid equilibration of the H_2O_2 concentration in the nanoparticle bulk. Despite this kinetic difference, larger and smaller nanoparticles behaved similarly from a structural point of view: for example, DOSY spectra (Figures 4B and G) and size distributions (Figures 4D and H) showed that also in this case the oxidation implied the loss of the Pluronic coating (always present in micellar form after oxidation) and that the nanoparticles increased in size. However it is noteworthy that the 160 nm nanoparticles produced also some high diffusion coefficient (ca. 2-20 nm sized) polysulf(ox)ide-containing compounds (<10% in mol of the dispersed material); due to the high degree of oxidation, they are probably produced by the hydrolysis of the cross-liker´s ester groups, which are no longer protected by a hydrophobic environment.

2.3.3 Nanoparticle response to hypochlorite

Hypochlorite almost instantaneously decreased the turbidity of nanoparticle dispersions, and it is noticeable that this reached a minimum at the stoichiometric equivalence between sulfides and hypochlorite (Figure 2.3-5A and B): at a 4.3 mM thioether concentration, the opacity was rapidly reduced to less than a half at 2.5 mM ClO^- and down to zero at 10 mM ClO^-. DLS analysis suggested this effect to be due to a reduction in particle number, since the scattering intensity decreased but the particle size remained substantially unaltered (Figure 2.3-5A and B, empty circles); the reduction in particle number without significant changes in dimension was also confirmed by TEM (Figure 2.3-5C). Also the ClO^--mediated oxidation may proceed through an autocatalytic mechanism, although much more rapid than for H_2O_2: this would explain the

persistence of apparently pristine nanoparticles (= unaltered size and negligible Nile Red fluorescence) at intermediate oxidant concentrations. Diffusion NMR experiments supported this point, showing that at a 1:1 sulfide/hypochlorite molar ratio, only micellar Pluronic and oxidized low molecular weight compounds could be detected, without any larger colloidal object being present (Figure 2.3-6). The nanoparticle solubilization is to ascribe to polymer fragmentation occurring at sulfone sites and producing fragments containing carbonyl, hydroxyl and sulfone groups ($\rightarrow$ band at 1350 cm^{-1}, see Supporting Information, Figure 2.7-SI-13 B), as previously shown on linear polysulfides[14]. Nile Red fluorescence at 620 nm remained very low at any time point for any ClO^- concentration (data not shown), suggesting that the fluorophore did not experience environments with intermediate polarity (as opposed to with H_2O_2) for significant periods of time during the oxidation process.

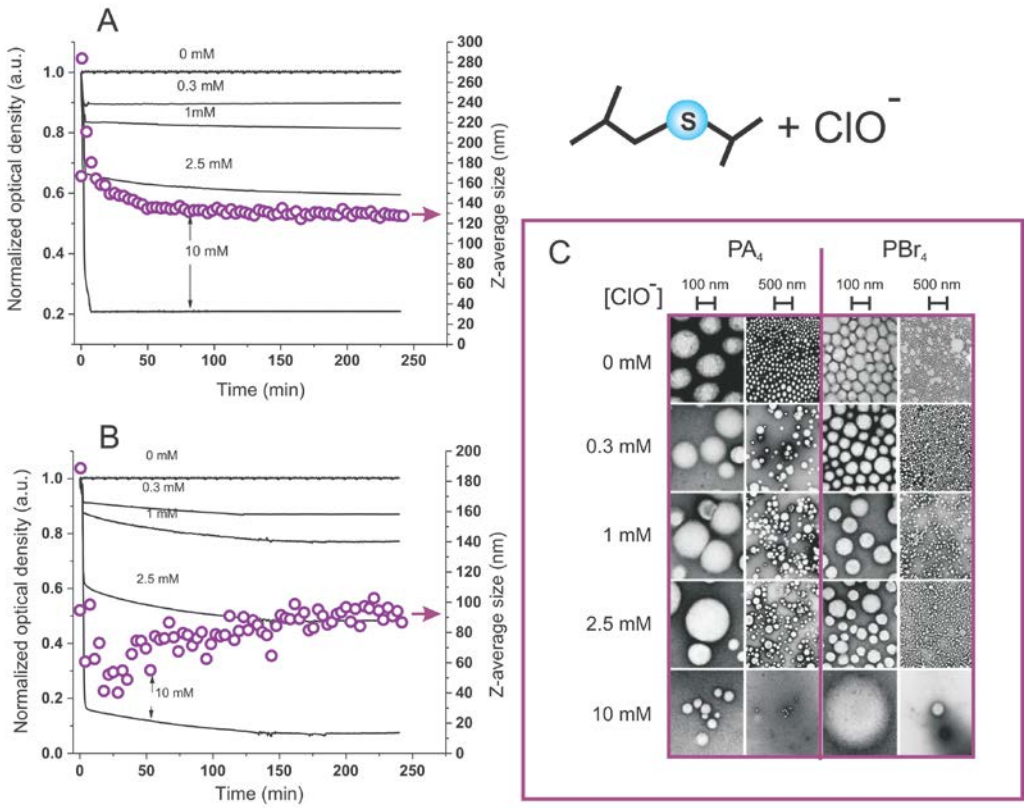

Figure 2.3-5 ***A:*** Optical density at 600 nm (solid lines) and Z-average size (open circles) of 0.32 mg/mL PA_4-based nanoparticle dispersions vs. tune for different ClO^- concentrations; please note a sudden and transient increase in the nanoparticle size at initial reaction times (<3 min), which is possibly related to the initial swelling of degrading particles. ***B:*** As in graph A, but using PBr_4-based nanoparticles. ***C:*** TEM images of PA_4 and PBr_4 nanoparticles oxidized with different concentrations of NaOCl for 240 min (at 37 ºC and pH = 7.4) and then purified via dialysis. Although in some cases a small increase in nanoparticle dimensions could be noticed, the most striking result of this analysis is the dramatic reduction in the number of nanoparticles when approaching the stoichiometric thioether/ClO^- equivalence.

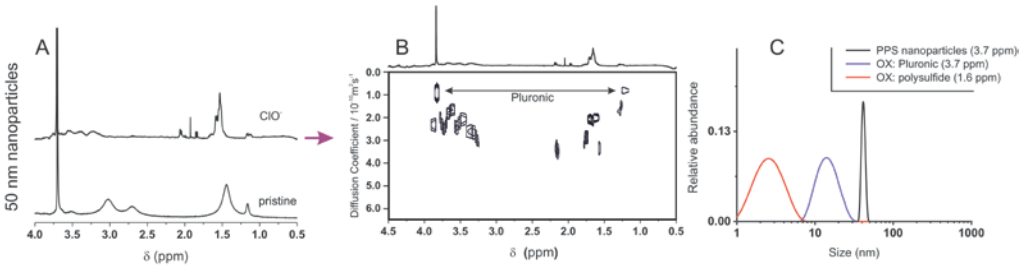

Figure 2.3-6 ***A,*** ^{1}H NMR spectra of 50 nm PA_4 nanoparticles (10 mg/mL) recorded before and after exposure to 135 mM NaOCl (stoichiometric equivalence to sulfides). ***B.*** DOSY spectrum of the oxidized nanoparticles. ***C.*** Size distributions obtained by applying a CONTIN algorithm to DOSY data.

It is therefore apparent that the ROS-dependent chemical response was mirrored by a ROS-dependent evolution of the material morphology, as graphically summarized in Scheme 2.3-2.

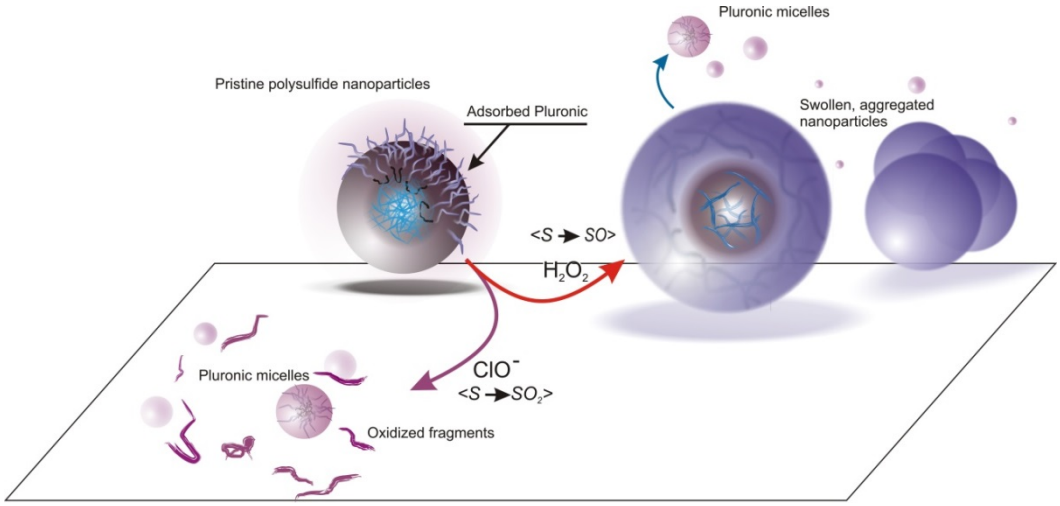

Scheme 2.3-2 Summary of the main effects of hydrogen peroxide and hypochlorite on polysulfide nanoparticles.

It is noticeable that, despite the known sensitivity of polyether chains to oxidizing conditions[29], both hydrogen peroxide and hypochlorite did not appear to dramatically affect Pluronic behaviour: 1) if oxidized groups (e.g. carbonyls) were introduced in large amounts in Pluronic chains without cleaving them, their

resonances should be recorded in correspondence of the Pluronic micelles' diffusion coefficient; however, the only intense signals that we could recognize in NMR are those of ethylene glycol units and propylene glycol methyl groups (Figure 2.3-4B and G, Figure 2.3-6B). 2) If Pluronic chains were significantly cleaved, this would have predominantly occurred in PEG blocks, leading to a lower hydrophilic/hydrophobic balance and to the formation of larger aggregates associated by the Pluronic resonances; however, the only diffusion coefficient associated to PEG resonances was indeed that of the usual Pluronic micelles, both for oxidation with hydrogen peroxide and hypochlorite. This does not imply the complete absence of Pluronic oxidation, but indicates a protective effect of polysulfides.

2.3.4 Biological effects of the differential oxidation response

Due to the morphologically and chemically different nature of the H_2O_2 and ClO^- oxidation products, it is reasonable to assume them to have different effects on a cellular environment. The cytotoxicity of nanoparticles was assessed using two common cell lines: L929 mouse fibroblasts and J774.2 mouse macrophages (Figure 2.3-7A); the latter phagocytic cells are typically characterized by a higher sensitivity to toxic stimuli and were used as a worst case scenario. PPS nanoparticles had already shown a benign character *in vivo*[11], therefore the absence of significant effects on the viability of both cell lines also at concentrations as high as 5 mg/mL is not surprising. More importantly, the H_2O_2-oxidized nanoparticles showed an remarkably benign behavior, which confirms previous data of low cytotoxicity of the oxidized linear PPS (IC50 >30-40 mg/mL on L929 mouse fibroblasts[14]).

The products of ClO^--mediated oxidation provided a pretty different picture. They considerably reduced the viability of both cell lines already at a concentration of 0.3 mg/mL, with IC50s located around 1 mg/mL. Although the sulfone-containing fragments were considerably more toxic from their precursors, these IC50 values are similar to those of several polymers generally considered 'biocompatible' such as chitosan, and indicate also a lower toxicity than hypochlorite: the IC50 of NaOCl in L929 mouse fibroblasts (24 h exposure)

is reported to be lower than 0.05 mg/mL = 0.7 mM[30]. The polysulfide nanoparticles may therefore provide a remarkable detoxification effect; indeed, following an analogous concept, similar nanoparticles have been used to improve the stability of enzymes against hypochlorite[31].

Using both cell lines we have confirmed the hypochlorite IC50 to be in the range of 0.7-1 mM for fibroblasts (Figure 2.3-6B). Exposing then the cells to hypochlorite at a concentration > IC50 (1.25 mM, with a residual cell viability of ≈ 20%), we have recorded a 3-fold improvement of viability in the presence of nanoparticles at the concentration of the hypochlorite:sulfide stoichiometric equivalence (arrow in Figure 2.3-6C).

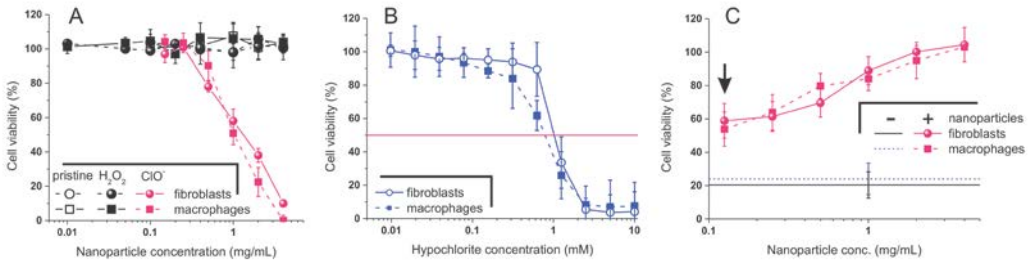

Figure 2.3-7 ***A*****:** Viability of L929 fibroblasts and J774.2 macrophages (mitochondrial activity measured via MTS and normalized against the protein content measured via BCA) upon incubation with nanoparticles before and after oxidation with H_2O_2 and ClO^- (15% H_2O_2, 10 mM ClO^-; 48 h; 37 ºC; pH = 7.4). Please realize that the nanoparticles were purified via dialysis and very low MW compounds (<1 kDa) were eliminated. ***B*****:** Viability of the two cell lines upon a 48 hours incubation with different concentrations of hypochlorite. ***C*****:** Viability of the two cell lines upon a 48 hours incubation with 1.25 mM hypochlorite and different concentrations of nanoparticles. The arrow indicated the results for the nanoparticle concentration with a stoichiometric equivalence between hypochlorite and sulfide groups. The two horizontal lines indicate the viability of the two cell lines in the absence of nanoparticles.

Keeping fixed the concentration of hypochlorite, and considering the apparently stoichiometric character of its oxidation, the same amount of oxidized fragments should be produced irrespectively of the overall concentration of nanoparticles, which would therefore be expected not to influence the cell viability. On the

contrary, the viability increased with increasing nanoparticle concentration, above all above 1 mg/mL, which indicates the presence of further protecting effects of the polysulfides.

2.4 Conclusions

Polysulfide nanoparticles can be produced with a controlled size (through the Pluronic/PS ratio) and a homogeneous cross-linking density (through the control over PPS molecular weight); we have showed that they feature different oxidation-responsive mechanisms in response to the presence of different ROS, and that this point does not depend on size and nature of the cross-linker. In particular, the exposure to H_2O_2 induces swelling and loss of PEGylated surface layer without however significantly affecting the nanoparticle cytotoxicity; on the contrary, ClO^- causes instantaneous solubilization and production of medium-toxicity fragments, in addition to the concomitant release of Pluronic (as summarized in Scheme 2.3-2).

This differential response can open the way to ROS-specific therapeutic actions e.g. release of encapsulated drugs. The remarkable sensitivity to ClO^- could make them particularly attractive to perform rapid and efficient actions in response to pathological neutrophil respiratory bursts[32], or to other pathologies based on myeloperoxidase over-activation[33]. On the other hand, their slower response to H_2O_2 and lower toxicity after oxidation appear more suited for more sustained release actions.

It is noteworthy that similar general considerations could be applied to materials sensitive to reducing agents; for example, disulfide-containing materials are notoriously responsive to the presence of thiols[34,35], but chemical details unrelated to the REDOX potential may significantly affect the material response, e.g. the tendency of the thiol to produce homo- or heterodisulfides or the kinetics of the thiol-disulfide exchange process.

2.5 Acknowledgements

Dr. Jureerat Laliturai gratefully acknowledges a studentship from the Government Pharmaceutical Organization of Thailand. Mr. Damien Jeanmaire and Mr. Richard d'Arcy are indebted to EPSRC for their studentships in the NoWNano Doctoral Training Centre. Financial support from EPSRC (grant No. EP/C543564/1 and Advanced Research Fellowship for Nicola Tirelli) for the initial part of this work and from the Knowledge Centre of Materials Chemistry (University of Manchester) is also gratefully acknowledged.

2.6 References

1 Adler, V.; Yin, Z. M.; Tew, K. D.; Ronai, Z. Role of Redox Potential and Reactive Oxygen Species in Stress Signaling. *Oncogene* **1999**, *18*, 6104–6111.

2 Rahman, I.; MacNee, W. Oxidative Stress and Regulation of Glutathione in Lung Inflammation. *Eur. Respir. J.* **2000**, *16*, 534–554.

3 Khutoryanskiy, V. V.; Tirelli, N. Oxidation-Responsiveness of Nanomaterials for Targeting Inflammatory Reactions. *Pure Appl. Chem.* **2008**, *80*, 1703–1718.

4 Lux, C. D.; Joshi-Barr, S.; Nguyen, T.; Mahmoud, E.; Schopf, E.; Fomina, N.; Almutairi, A. Biocompatible Polymeric Nanoparticles Degrade and Release Cargo in Response to Biologically Relevant Levels of Hydrogen Peroxide. *J. Am. Chem. Soc.* **2012**, *134*, 15758–15764.

5 Lallana, E.; Tirelli, N. Oxidation-Responsive Polymers: Which Groups to Use, How to Make Them, What to Expect From Them (Biomedical Applications). *Macromol. Chem. Phys.* **2013**, *214*, 143–158.

6 Huo, M.; Yuan, J.; Tao, L.; Wei, Y. Redox-Responsive Polymers for Drug Delivery: From Molecular Design to Applications. *Polym. Chem.* **2013**, DOI: 10.1039/C3PY01192E.

7 Lee, S. H.; Gupta, M. K.; Bang, J. B.; Bae, H.; Sung, H. J. Current Progress in Reactive Oxygen Species (ROS)-Responsive Materials for Biomedical Applications. *Adv. Healthc. Mater.* **2013**, *2*, 908–915.

8 Babior, B. M. Phagocytes and Oxidative Stress. *Am. J. Med.* **2000**, *109*, 33–44.

9 Hu, P.; Tirelli, N. Inter-Micellar Dynamics in Block Copolymer Micelles: FRET Experiments of Macroamphiphile and Payload Exchange. *React. Funct. Polym.* **2011**, *71*, 303–314.

10 Napoli, A.; Valentini, M.; Tirelli, N.; Muller, M.; Hubbell, J. A. Oxidation-Responsive Polymeric Vesicles. *Nat. Mater.* **2004**, *3*, 183–189.
11 Rehor, A.; Schmoekel, H.; Tirelli, N.; Hubbell, J. A. Functionalization of Polysulfide Nanoparticles and Their Performance as Circulating Carriers. *Biomaterials* **2008**, *29*, 1958–1966.
12 Allen, B. L.; Johnson, J. D.; Walker, J. P. Encapsulation and Enzyme-Mediated Release of Molecular Cargo in Polysulfide Nanoparticles. *ACS Nano* **2011**, *5*, 5263–5272.
13 Rehor, A.; Botterhuis, N. E.; Hubbell, J. A.; Sommerdijk, N.; Tirelli, N. Glucose Sensitivity through Oxidation Responsiveness. An Example of Cascade-Responsive Nano-Sensors. *J. Mater. Chem.* **2005**, *15*, 4006–4009.
14 Carampin, P.; Lallana, E.; Laliturai, J.; Carroccio, S. C.; Puglisi, C.; Tirelli, N. Oxidant-Dependent REDOX Responsiveness of Polysulfides. *Macromol. Chem. Phys.* **2012**, *213*, 2052–2061.
15 Koppenol, W. H.; Butler, J. Energetics of Interconversion Reactions in Oxyradicals. *Adv Free Radic. Biol Med* **1985**, *1*, 91–131.
16 Winterbourn, C. C. Reconciling the Chemistry and Biology of Reactive Oxygen Species. *Nat. Chem. Biol.* **2008**, *4*, 278–286.
17 Yeager, E. Dioxygen electocatalysis mechanisms in relation to catalyst structure. *J. Mol. Catal.* **1986**, *38*, 5–25.
18 Koppenol, W. H. Thermodynamic considerations on the formation of reactive species from hypochlorite, superoxide and nitrogen monoxide - could nitrosyl chloride be produces by neutrophils and macrophages. *FEBS Lett.* **1994**, *347*, 5–8.
19 Hu, P.; Tirelli, N. Scavenging ROS: Superoxide Dismutase/Catalase Mimetics by the Use of an Oxidation-Sensitive Nanocarrier/Enzyme Conjugate. *Bioconjug. Chem.* **2012**, *23*, 438–449.
20 Hirosue, S.; Kourtis, I. C.; van der Vlies, A. J.; Hubbell, J. A.; Swartz, M. A. Antigen Delivery to Dendritic Cells by Poly(propylene Sulfide) Nanoparticles with Disulfide Conjugated Peptides: Cross-Presentation and T Cell Activation. *Vaccine* **2010**, *28*, 7897–7906.
21 Stano, A.; van der Vlies, A. J.; Martino, M. M.; Swartz, M. A.; Hubbell, J. A.; Simeoni, E. PPS Nanoparticles as Versatile Delivery System to Induce Systemic and Broad Mucosal Immunity after Intranasal Administration. *Vaccine* **2011**, *29*, 804–812.
22 Thomas, S. N.; van der Vlies, A. J.; O'Neil, C. P.; Reddy, S. T.; Yu, S. S.; Giorgio, T. D.; Swartz, M. A.; Hubbell, J. A. Engineering Complement Activation on Polypropylene Sulfide Vaccine Nanoparticles. *Biomaterials* **2011**, *32*, 2194–2203.
23 Rehor, A.; Tirelli, N.; Hubbell, J. A. A New Living Emulsion Polymerization Mechanism: Episulfide Anionic Polymerization. *Macromolecules* **2002**, *35*, 8688–8693.
24 Vo, C. D.; Kilcher, G.; Tirelli, N. Polymers and Sulfur: What Are Organic Polysulfides Good For? Preparative Strategies and Biological Applications. *Macromol. Rapid Commun.* **2009**, *30*, 299–315.
25 Valentini, M.; Vaccaro, A.; Rehor, A.; Napoli, A.; Hubbell, J. A.; Tirelli, N. Diffusion NMR Spectroscopy for the Characterization of the Size and

Interactions of Colloidal Matter: The Case of Vesicles and Nanoparticles. *J. Am. Chem. Soc.* **2004**, *126*, 2142–2147.

26 Kilcher, G.; Wang, L.; Tirelli, N. Role of Thiol-Disulfide Exchange in Episulfide Polymerization. *J. Polym. Sci. Part Polym. Chem.* **2008**, *46*, 2233–2249.

27 Johnson, C. S. Diffusion Ordered Nuclear Magnetic Resonance Spectroscopy: Principles and Applications. *Prog. Nucl. Magn. Reson. Spectrosc.* **1999**, *34*, 203–256.

28 Pelta, M. D.; Morris, G. A.; Stchedroff, M. J.; Hammond, S. J. A One-Shot Sequence for High-Resolution Diffusion-Ordered Spectroscopy. *Magn. Reson. Chem.* **2002**, *40*, S147–S152.

29 Lange, M.; Braune, S.; Luetzow, K.; Richau, K.; Scharnagl, N.; Weinhart, M.; Neffe, A. T.; Jung, F.; Haag, R.; Lendlein, A. Surface Functionalization of Poly(ether Imide) Membranes with Linear, Methylated Oligoglycerols for Reducing Thrombogenicity. *Macromol. Rapid Commun.* **2012**, *33*, 1487–1492.

30 Simbula, G.; Dettori, C.; Camboni, T.; Cotti, E. Comparison of Tetraacetylethylendiamine plus Sodium Perborate and Sodium Hypochlorite Cytotoxicity on L929 Fibroblasts. *J. Endod.* **2010**, *36*, 1516–1520.

31 Allen, B. L.; Johnson, J. D.; Walker, J. P. Hydrolase Stabilization via Entanglement in Poly(propylene Sulfide) Nanoparticles: Stability towards Reactive Oxygen Species. *Nanotechnology* **2012**, *23*.

32 Heinzelmann, M.; Mercer-Jones, M. A.; Passmore, J. C. Neutrophils and Renal Failure. *Am. J. Kidney Dis.* **1999**, *34*, 384–399.

33 Van der Veen, B. S.; de Winther, M. P. J.; Heeringa, P. Myeloperoxidase: Molecular Mechanisms of Action and Their Relevance to Human Health and Disease. *Antioxid. Redox Signal.* **2009**, *11*, 2899–2937.

34 Cheng, R.; Feng, F.; Meng, F. H.; Deng, C.; Feijen, J.; Zhong, Z. Y. Glutathione-Responsive Nano-Vehicles as a Promising Platform for Targeted Intracellular Drug and Gene Delivery. *J. Controlled Release* **2011**, *152*, 2–12.

35 Klaikherd, A.; Nagamani, C.; Thayumanavan, S. Multi-Stimuli Sensitive Amphiphilic Block Copolymer Assemblies. *J. Am. Chem. Soc.* **2009**, *131*, 4830–4838.

2.7 Supporting information

2.7.1 Synthesis of model polysulfides

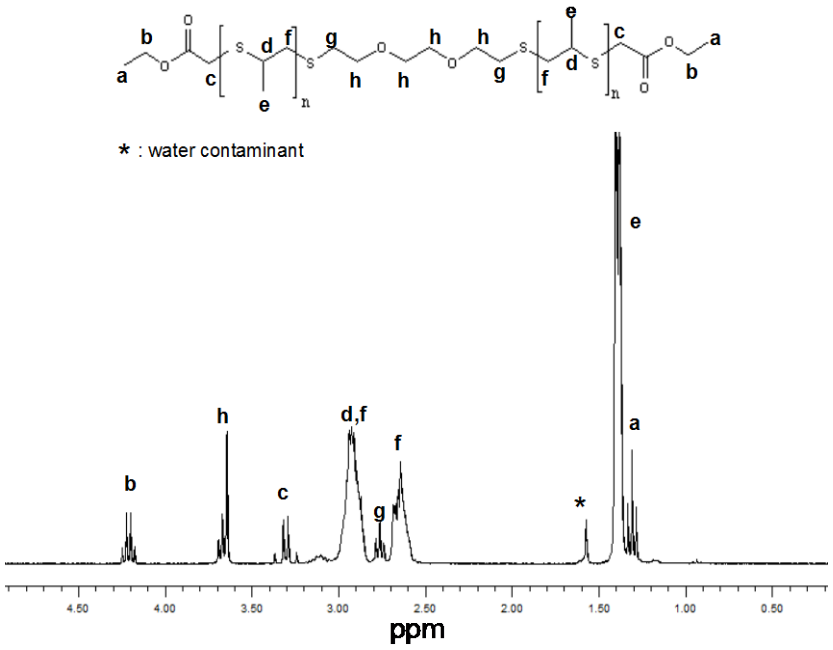

Figure 2.7-SI-8 ^{1}H NMR spectrum of PPS with theoretical *overall DP* = 30, end-capped with ethyl 2-bromoacetate.

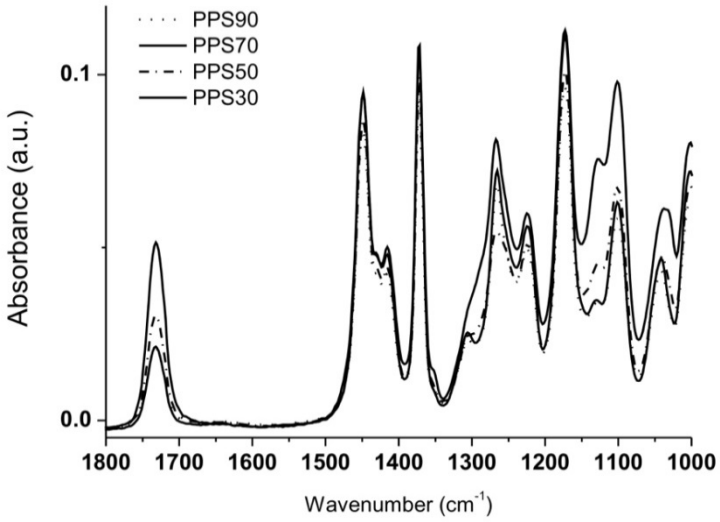

Figure 2.7-SI-9 FT-IR spectra of PPS with variable DP and end-capped with ethyl 2-bromoacetate. The spectra were normalized against the absorbance of the CH_3 stretching band at 2959 cm^{-1}.

2.7.2 Nanoparticle freeze drying

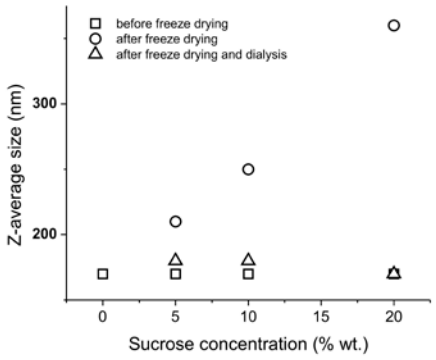

Figure 2.7-SI-10 Z-average size of PA_4 nanoparticles obtained with a 0.02 Pluronic/PS weight ratio after synthesis and purification (solid squares), after freeze drying of dispersions containing different amounts of sucrose (open circles) and after the removal of sucrose via dialysis (through membranes with 3,500 Da MWCO, open triangles), which provided nanoparticles virtually indistinguishable from the starting ones.

2.7.3 Nanoparticle oxidation

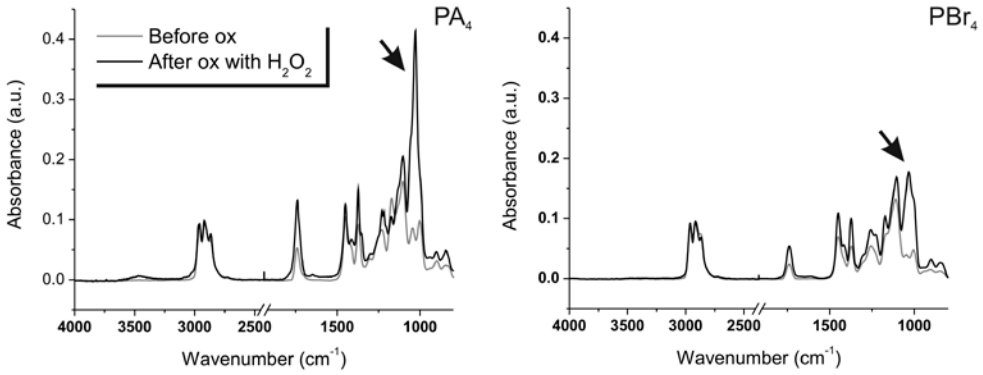

Figure 2.7-SI-11 Comparison of FT-IR spectra of PPS nanoparticles (Z-average size: 160 nm) before and after 4 h oxidation with H_2O_2 (15% wt.). The spectra were normalized against the CH_3 stretching band at 2958 cm^{-1}. With both the PA_4 (*left*) and the PBr_4 (*right*) cross-linkers, the main spectral difference is the appearance of an S=O stretching band (arrow). The carbonyl band shows an increase in strength, which may be due to hydrolytic processes (the stretching of a carboxylate can be stronger than that of an ester and can be localized in the same spectral area) although the higher polarity of the environment may play a role too. However, the increase is very moderate if other bands are used for normalization.

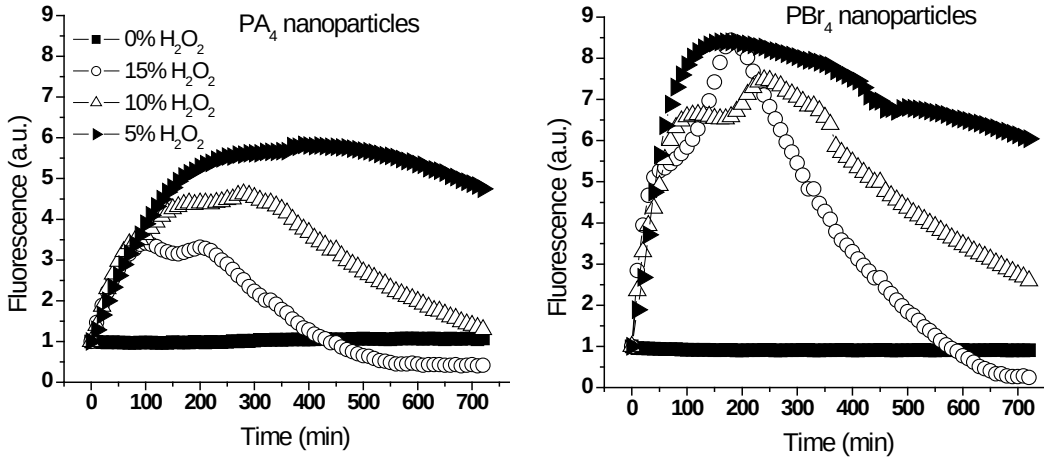

Figure 2.7-SI-12 Fluorescence emission intensity of Nile Red-loaded PA_4 (left) and PBr_4 (right) nanoparticles vs. H_2O_2 concentration and time (excitation at 540 nm, emission at 620 nm; 1:25000 Nile Red/thioether molar ratio). Although a higher fluorescence intensity can be detected for the second kind of particles, the kinetic behavior is substantially identical.

Table 2.7-SI-2 T_2 relaxivity measurements of PA_4 nanoparticles (50 nm in Z-average size). The relaxivity of the protons associated to the methyl group on the PPS chain and the relaxivity of the protons associated to the CH_2 of PEG and CH_3 of PPG of the surfactant, Pluronic F127, were measured on untreated nanoparticles and on PPS nanoparticles, 3 h after being treated with 5% H_2O_2.

	Polysulfide	*Pluronic*	
	CH_3 (1.5/1.6 ppm)	CH_2 (3.7 ppm, PEG)	CH_3 (PPG)
untreated	43 ms	111 ms	89 ms
5% H_2O_2	934 ms	333 ms	266 ms

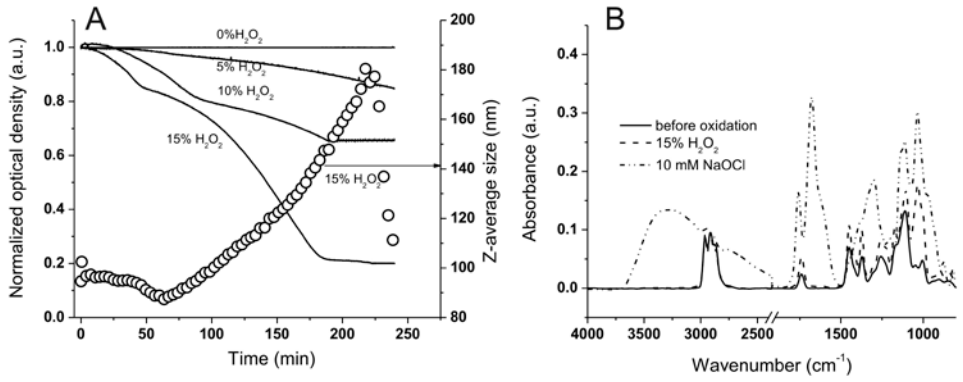

Figure 2.7-SI-13 Oxidation of PBr_4 nanoparticles in deionized water (0.32 mg/mL) at 37 ºC and pH = 7.4. *A.* Optical density at 600 nm (solid lines) and Z-average size (open circles) of nanoparticle dispersion vs. H_2O_2 concentration and time. As expected on the basis of the higher hydrolytical lability of the PBr_4 esters, signs of solubilization (drop both in size and in scattered intensity) were recorded after 220 minutes exposure to 15% wt. H_2O_2; however, FT-IR analysis did not show appreciable presence of carboxylate groups (flat baseline below 1700 cm^{-1}) either after 220 minutes with 15% or after 24 h with 10% wt. H_2O_2, suggesting that the "solubilization" process is likely to initially produces branched polymer structures (= a few cleaved esters would be necessary for solubilization). *B*. Comparison of FT-IR spectra of the nanoparticles before and after 4 h oxidation with H_2O_2 (15% wt.) or OCl^- (10 mM). The spectra were normalized against the CH_3 stretching band at 2958 cm^{-1}.

3 Binary behaviour of an oxidation-responsive MRI nano contrast agent

Damien Jeanmaire,[a] Grigore Timco,[b] Arianna Gennari,[c] Stephen Sproules,[b] Kaye J. Williams,[a] Richard E.P. Winpenny [b] and Nicola Tirelli*[c,d2]

[a]Manchester School of Pharmacy, University of Manchester, Oxford Road, Manchester M13 9PT, United Kingdom.

[b]School of Chemistry, University of Manchester, Brunswick Street, Manchester, M13 9PL, UK.

[c]Institute of Inflammation & Repair, University of Manchester, Oxford Road, Manchester M13 9PT, United Kingdom.

[d]School of Materials, University of Manchester, Grosvenor Street, Manchester, M1 7HS, UK.

* to whom correspondence should be addressed :

Prof. Nicola Tirelli, School of Materials and Institute of Inflammation and Repair / School of Medicine, University of Manchester, Oxford Road, Manchester, M13 9PT, United Kingdom

Tel.: +44 161 275 24 80.

Fax: +44 161 275 23 96

Email: nicola.tirelli@manchester.ac.uk

[2] **Author Contributions**: Grigore Timco – heterometallic wheel synthesis, Arianna Gennari – glucose oxidase study, Stephen Sproules – EPR measurements, Kaye Williams/Richard Winpenny/Nicola Tirelli - Supervisors

Abstract

A new nano contrast agent has been prepared incorporating a molecular magnet in oxidation-responsive nanoparticles; this system has shown a remarkable sensitivity to hydrogen peroxide (detection down to at least 40 μM). which was used as a model ROS. Surprisingly, the response had a binary (off/on) character, due to a non-linear cascade relation between extent of oxidation and water permeability in the particles.

3.1 Introduction

Contrast agents (CA) are molecular materials used to increase contrast in the biomedical applications of Magnetic Resonance Imaging (MRI). In the clinical practice, the most widely used CAs increase the magnitude of the MR signal by reducing the longitudinal relaxation time (T_1) of water hydrogen nuclei; this action leads to a signal enhancement, hence they are defined as positive CAs. Water molecules directly bind to these paramagnetic systems (Gd-DO3A-butron in Gadovist®, Gd-DOTA in Dotarem®, etc)[1, 2] while also rapidly exchanging. Negative CAs predominantly affect the water transverse relaxation time (T_2), whose decrease leads to a decrease in the MR signal; the mode of action of these metallic or metal oxide clusters, e.g. Superparamagnetic Iron Oxide Nanoparticles (SPIONs)[3], is based on non-contact dipole-dipole interactions with nearby water molecules. The main advantages of negative CAs are a) their high saturation magnetization, which allows for lower diagnostic doses than for positive CAs, b) a better control in their biodistribution since their nanoparticulate nature makes it difficult for them to cross a number of biological barriers.

CAs capable of an environmentally- and possibly metabolically sensitive response[4], e.g. responding to variations in pH[5] or REDOX potential[6], could in principle allow to selectively image pathological conditions. We are specifically interested in mapping the presence of biological oxidants (Reactive Oxygen Species (ROS)), which are generally associated to both pathological and non-pathological inflammatory reactions[7-10].

3.2 Experimental

The literature provides several examples of positive CAs with 'smart' behaviour, due the ease of precisely engineering the water binding site of metallorganic complexes with groups capable of a REDOX or pH responsiveness [11 12, 13]. Here, we tackled the design of a REDOX-responsive negative CA. This system is based

on a hydrophobic molecular magnet physically entrapped into ROS-sensitive nanoparticles, which are composed of a cross-linked hydrophobic but oxidizable polymer matrix. The magnet would be shielded from interacting with water by the nanoparticle matrix in a completely reduced state; a similar concept has been exploited by Almutairi, encapsulating Gd oxide in (pH- or oxidative) degradable nanoparticles to yield responsive positive CAs[14]. Differently from this example, we are seeking to obtain a strongly non-linear effect, i.e. to boost the sensitivity of the system by associating a large T_2 reduction to a very early oxidative response. The rationale is that a minimal degree of oxidation may be sufficient to increase the water penetration in the particles to a level high enough to affect its magnetic interactions (Figure 3.2-1A).

As a molecular magnet we have employed an anti-ferromagnetically-coupled polycyclic coordination compound (**1**) [15], which is composed of a large ring (a 'wheel') of fluorine-bridged metal atoms (seven chromium, one nickel); this is surrounded by a corona of 2-ethylhexanoic groups conferring a hydrophobic exterior and making the magnet organosoluble (Figure 3.2-1B). Due to the lack of free coordination sites, the magnetic interaction of **1** with water is strictly dipole-dipole, which makes the system suitable to develop a negative (T_2-weighted) CA. Heterometallic wheels are extensively investigated by our group [16, 17], and **1** is only one example of possible molecular magnetic structures. To our knowledge, the only other example of a single molecule magnet CA is from Wu who uses Mn_{12} as a negative CA[18].

The host nanoparticles were prepared following a two-step literature procedure[19, 20] via a) emulsion anionic episulfide polymerization (monomer: propylene sulfide, PS), which is initiated via the deprotection of a bifunctional initiator and provides double thiol-terminated poly(propylene sulfide) (PPS) chains; b) subsequent cross-linking of the material via Michael-type addition of the terminal thiols with a tetraacrylate.

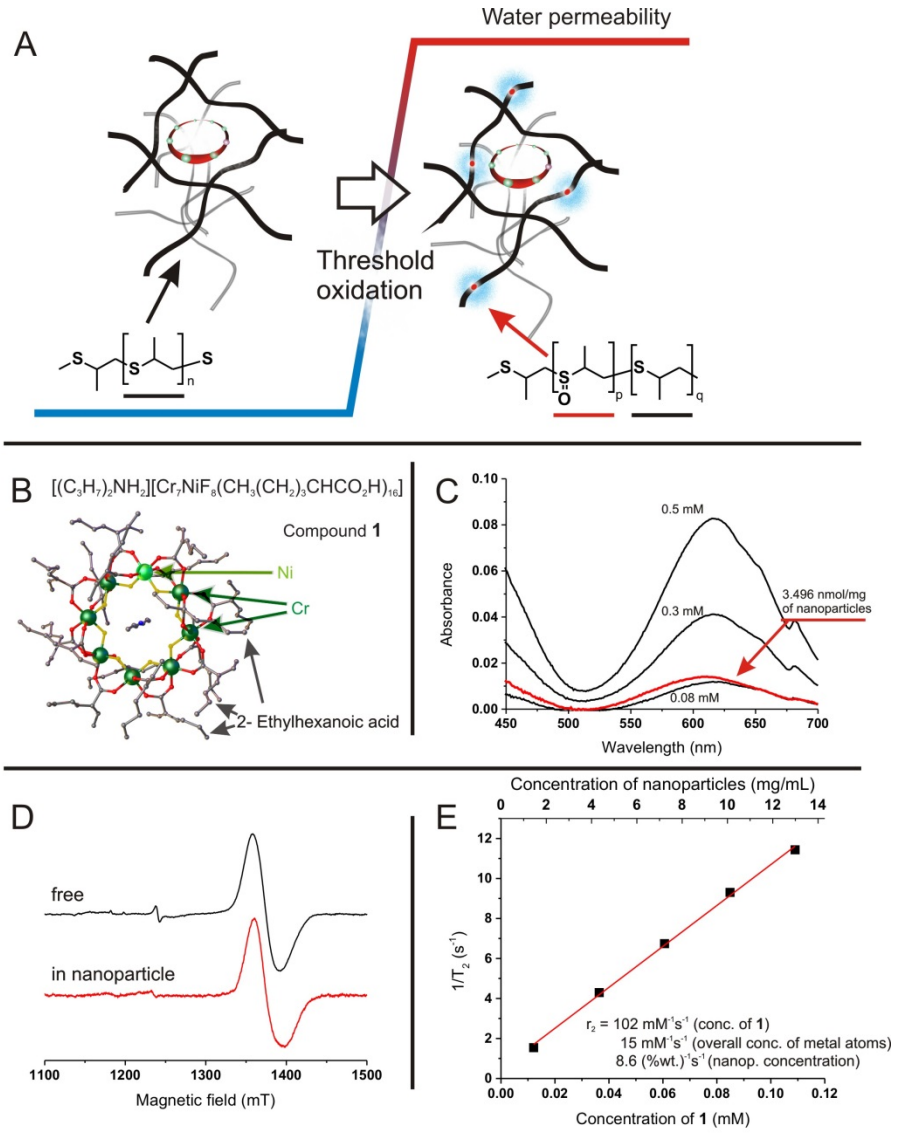

Figure 3.2-1 ***A:*** Scheme of the mode of oxidant-response of the magnet-loaded nanoparticles. The molecular magnets influence the water T_2 values in a fashion proportional to the water solubility and diffusivity in the matrix that surround them; both parameters increase upon the oxidative conversion of thioethers to sulfoxides, as operated by hydrogen peroxide. ***B:*** Wheel-like structure of the molecular magnet (**1**). ***C:*** Vis spectra of **1** in THF at different concentrations in reference solutions (black lines) and after swelling and sonication of freeze dried nanoparticles (red line, corrected of a scattering baseline as described in Supplementary Information, **Figure 3.6-SI-3**). ***D:*** EPR spectra of **1** in a pure form and in freeze dried nanoparticles (50 nm, 8.42 nmol of **1**/mg); the spectra are characteristic of an S = ½ species with axial symmetry - a pair of transitions at g_{xy} = 1.781 and g_z = 1.740. ***E:*** Relaxivity of 50 nm nanoparticles with a load of 8.42 nmol of **1**/mg of particle.

3.3 Results

The size of the nanoparticles can be precisely controlled through the ratio between monomer and emulsifier (Pluronic F127); in order to maximize the exchange surface between water and the magnet-loaded matrix, we have prepared them with the smallest size compatible with the emulsion process, i.e. with a hydrodynamic diameter of about 50 nm. The molecular magnet was added in form of THF solution after polymerization but prior to the cross-linking step; it was therefore loaded into the hydrophobic polysulfide matrix (composed by chains with an average number of 90 PS units), and then trapped through cross-linking in order to minimize uncontrolled leaching. The loading process did not significantly affect the molecular structure of **1**, nor the nanoparticle properties:

A) First, the visible absorption of **1** is unchanged (Figure 3.2-1C); incidentally, using this as a tool to assess the amount of magnet in the nanoparticles, it is possible to estimate a saturation level of 2.50% wt. = 8.42 nmol/mg of nanoparticles (Figure 3.2-1D. Also the EPR spectrum of **1** (Figure 3.2-1D, black line) was not appreciably modified in the encapsulation process, further confirming the integrity of the loaded magnets. It is worth mentioning that the magnet-loaded nanoparticles were characterized by a rather high relaxivity: particles with a magnet load of 8.42 nmol/mg exhibited a r_2 = 102 ± 5 $mM^{-1}s^{-1}$ if referred to the molar concentration of **1**; this corresponds to 15 $mM^{-1}s^{-1}$ if referred to the overall concentration of metal atoms or 8.6 $(\%wt)^{-1}s^{-1}$ if referred to the nanoparticle concentration (Figure 3.2-1E). The high relaxivity suggests that some dipolar interactions already occur despite the hydrophobicity of the particles, with the possible beneficial effect of allowing to trace also the non-oxidized nanoparticles. In fact, SPIONs have comparable, albeit generally larger r_2 values; for example, r_2 of the commercially available and similarly sized Resovist is reportedly comprised between 82[21] and 151[22] $mM^{-1}s^{-1}$, both expressed in reference to metal (Fe) atom concentration.

B) Second, the presence of **1** did not affect the size distribution of the particles (Figure 3.3-2A), nor their response to H_2O_2 used as a model ROS (Figure 3.3-2B). Please note that in this study we have employed reaction conditions (exposure time and concentration of H_2O_2) that cause only a minor oxidative conversion of sulphides to sulfoxides (<5%), see e.g. the low intensity of the S=O stretching band in Figure 3.3-2B and the substantial absence of swelling in Figure 3.3-2A.

The magnet-loaded particles showed a significant decrease (>50%) decrease in T_2 upon exposure to H_2O_2. It is worth pointing out that this effect could not be studied in the presence of high concentrations of the peroxide, since the latter alone lowers the water T_2 to less than 60 ms (an effect well known in literature[23]). Therefore, for concentrations >10 mM, H_2O_2 was removed via the addition of KI (Supporting Information, Figure 3.6-SI-4 and Table 3.6-SI-1). Within the experimental limits of this investigation, the oxidation provided a binary, off-on response: a strong T_2 reduction was observed for oxidation times as short as 15 minutes (Figure 3.3-2C) and for H_2O_2 concentrations as low as 0.05 mM (Figure 3.3-2D) with no further reduction thereafter or at higher concentrations. The oxidation of the polysulfide matrix is a slow phenomenon: completion only after a few hours with 5% wt. H_2O_2[19] and with long initial lag[20]; no sulfoxide band detected by IR after 15 minutes (data not shown); thus it seems reasonable to conclude that the critical concentration of oxidized groups to enable significant effects on water permeability, and thus on water T_2, is extremely small.

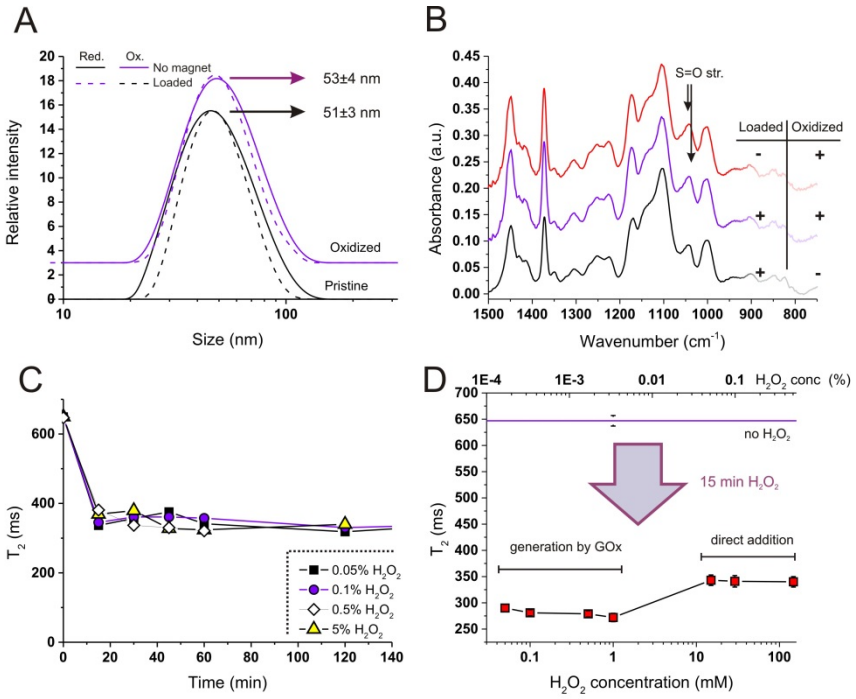

Figure 3.3-2 ***A:*** the presence of **1** (8.42 nmol/mg of particle) did not significantly alter the size distribution of polysulfide nanoparticles (black curves); oxidation for 30 minutes with 0.5% H_2O_2 negligibly shifted the distribution to larger sizes, independently on the presence of **1**. ***B:*** Exposure to 0.5% H_2O_2 for 30 minutes is known[19] to introduce only small amounts of sulfoxide groups, as it can be seen from the very moderate increase of the band at 1050 cm^{-1} due to a component associated to S=O stretching. The presence of **1** introduces no appreciable difference in the IR spectra (compare red and purple spectra). ***C:*** The reduction in T_2 following exposure of 2 mg/mL nanoparticles to 0.5% H_2O_2 was independent of oxidant concentration and exposure time. ***D:*** The CA response was investigated also at physiologically relevant concentrations of hydrogen peroxide, which was generated by glucose oxidase (GOx), confirming the high sensitivity of the system[3]. *n* = 3.

3.4 Conclusions

The inclusion of a molecular magnet in oxidizable nanoparticles has provided a T_2 CA with a strong sensitivity to hydrogen peroxide, with the potential of becoming a 'smart' system with the capacity of detecting ROS. The response observed to even very low concentrations of H_2O_2 is

[3] The T_2 values obtained after GOx treatment were marginally lower than those of samples treated directly with H_2O_2; this is possibly due to the presence of other chemicals (enzyme, glucuronic acid; please note that no pH drift was apparent) or to the fact that KI was not added to these experiments (tests showed the complete absence of residual H_2O_2).

particularly intriguing and is ascribed to a non-linear coupling between a chemical REDOX event (conversion of small amounts of sulfides into sulfoxides) and the development of a sufficiently high permeability to allow water molecules to interact with the molecular magnets.

3.5 References

1. C. F. G. C. Geraldes and S. Laurent, *Contrast Media Mol. I.*, 2009, **4**, 1-23.
2. G. Strijkers, W. M. Mulder, G. F. van Tilborg and K. Nicolay, *Anti-Cancer Agent. Me.*, 2007, **7**, 291-305.
3. H. B. Na, I. C. Song and T. Hyeon, *Adv. mater.*, 2009, **21**, 2133-2148.
4. L. M. De Leon-Rodriguez, A. J. M. Lubag, C. R. Malloy, G. V. Martinez, R. J. Gillies and A. D. Sherry, *Accounts Chem. Res.*, 2009, **42**, 948-957.
5. M. P. Lowe, D. Parker, O. Reany, S. Aime, M. Botta, G. Castellano, E. Gianolio and R. Pagliarin, *J. Am. Chem. Soc.*, 2001, **123**, 7601-7609.
6. S. J. Ratnakar, S. Viswanathan, Z. Kovacs, A. K. Jindal, K. N. Green and A. D. Sherry, *J. Am. Chem. Soc.*, 2012, **134**, 5798-5800.
7. A. Fernandez-Sanchez, E. Madrigal-Santillan, M. Bautista, J. Esquivel-Soto, A. Morales-Gonzalez, C. Esquivel-Chirino, I. Durante-Montiel, G. Sanchez-Rivera, C. Valadez-Vega and J. A. Morales-Gonzalez, *Int. J. Mol. Sci.*, 2011, **12**, 3117-3132.
8. H. Jaeschke, *J. Gastroen. Hepatol.*, 2011, **26**, 173-179.
9. P. S. Leung and Y. C. Chan, *Antioxid. Redox Sign.*, 2009, **11**, 135-165.
10. S. Reuter, S. C. Gupta, M. M. Chaturvedi and B. B. Aggarwal, *Free Radical Biol. Med.*, 2010, **49**, 1603-1616.
11. Q. N. Do, J. S. Ratnakar, Z. Kovacs and A. D. Sherry, *Chemmedchem*, 2014, **9**, 1116-1129.
12. C. Q. Tu and A. Y. Louie, *NMR Biomed.*, 2013, **26**, 781-787.
13. P. B. Tsitovich, P. J. Burns, A. M. McKay and J. R. Morrow, *J. Inorg. Biochem.*, 2014, **133**, 143-154.
14. M. L. Viger, J. Sankaranarayanan, C. D. Lux, M. Chan and A. Almutairi, *J. Am. Chem. Soc.*, 2013, **135**, 7847-7850.

15. A. Ghirri, V. Corradini, C. Cervetti, A. Candini, U. del Pennino, G. Timco, R. J. Pritchard, C. A. Muryn, R. E. P. Winpenny and M. Affronte, *Adv. Funct. Mater.*, 2010, **20**, 1552-1560.

16. M. Affronte, S. Carretta, G. A. Timco and R. E. P. Winpenny, *Chem. Commun.*, 2007.

17. G. A. Timco, T. B. Faust, F. Tuna and R. E. P. Winpenny, *Chem. Soc. Rev.*, 2011, **40**.

18. Y. Wang, W. Li, S. Zhou, D. Kong, H. Yang and L. Wu, *Chem. Commun.*, 2011, **47**, 3541-3543.

19. D. Jeanmaire, J. Laliturai, A. Almalik, P. Carampin, R. d'Arcy, E. Lallana, R. Evans, R. E. P. Winpenny and N. Tirelli, *Polym. Chem.*, 2014, **5**, 1393-1404.

20. V. V. Khutoryanskiy and N. Tirelli, *Pure Appl. Chem.*, 2008, **80**, 1703-1718.

21. D. Nordmeyer, P. Stumpf, D. Groeger, A. Hofmann, S. Enders, S. B. Riese, J. Dernedde, M. Taupitz, U. Rauch, R. Haag, E. Ruehl and C. Graf, *Nanoscale*, 2014, **6**, 9646-9654.

22. Y.-X. J. Wang, *Quant. Imaging Med. Surg.*, 2011, **1**, 35-40.

23. L. Buljubasich, B. Blümich and S. Stapf, *Phys. Chem. Chem. Phys.*, 2010, **12**, 13166-13173.

3.6 Supporting Information

All reagents and solvents were purchased from Sigma Aldrich (Gillingham, UK) and used without further purification.

Glucose and glucose oxidase from Aspergillus niger (EC 1.1.3.4, 156 U/mg) and type I peroxidase from horseradish (EC 1.11.1.7, 52 U/mg) were purchased form Sigma-Aldrich (Gillingham, UK). The substrate reagent B containing 3,3',5,5'-tetramethylbenzidine (TMB) was purchased from BD Biosciences (Oxford, UK).

3.6.1 Synthesis of low molecular weight compounds

1. The molecular magnet $[(C_3H_7)_2NH_2][Cr_7NiF_8(CH_3(CH_2)_3CHCO_2H)_{16}]$ (**1**) was prepared according to a literature procedure developed in the group of Winpenny [1]. The protected bifunctional initiator used to start the episulfide

emulsion polymerization, S,S'-[ethane-1,2-diylbis(ozyethane-1,1-diyl)] diethanethioate, was prepared according to a literature procedure developed in the group of Tirelli [2]

Preparation of cross-linked nanoparticles. 80 mg of Pluronic F127 were dissolved in 10 mL of degassed MilliQ water in a 25 mL Radley's Carousel parallel reactor tube. The system was continuously stirred at 1,000 rpm for 10 min under an argon atmosphere. In a separate vial, under argon atmosphere, the protected bifunctional initiator (0.013 g, 0.061 mmol) was mixed with 0.5 M CH_3ONa in methanol (245 μL) for 10 minutes, to deprotect it. The deprotected initiator and propylene sulphide (PS, 0.4 g, 5.48 mmol, corresponding to 45 PS equivalents per thiol group; overall DP = 90) were then added to the reaction flask, the reaction mixture was further stirred for 10 min, and 2 equivalents of DBU (0.018 g, 0.112 mmol) were finally added to initiate the polymerization. The reaction mixture was stirred under inert conditions for 2 h; the pH was lowered to 9.5 by the addition of acetic acid, and 0.5 equivalents of tetra-functional cross-linker pentaerythritol tetraacrylate (0.03 mmol, 0.010 g) dissolved in dichloromethane (0.3 mL) were then added to the reaction mixture. After 1 minute the pH was brought to 7.4 by adding 5 mL of PBS (50 mM, pH 7.4), in order to minimize the hydrolysis of the cross-linkers. The suspension was additionally stirred for 16 h before purification by ultrafiltration (Amicon Ultrafiltration Cell Model 8200, Millipore, UK) against MilliQ water through 300 kDa MWCO regenerated cellulose membranes (Spectrum Laboratories, UK). For any further use, the concentration of nanoparticles was determined gravimetrically after freeze drying samples of their dispersions. ATR FT-IR (thin film): 2956 (ν_{as} CH_3), 2920 (ν_{as} CH_2), 2856 (δ_s CH_2), 1740 (ν C=O), 1450 (δ_{as} CH_3), 1372 (δ_s CH_3), 1170 (ν_{as} C-O-C, ester), 1100 (ν_{as} C-O-C in Pluronic F-127), 800-600 cm^{-1} (ν C-S in PPS).

Loading of $[(C_3H_7)_2NH_2][Cr_7NiF_8(CH_3(CH_2)_3CHCO_2H)_{16}]$ (1) in PPS nanoparticles. The above preparative procedure was modified by adjusting the pH of the reaction mixture to 7.4 after polymerisation, dissolving $[(C_3H_7)_2NH_2][Cr_7NiF_8(CH_3(CH_2)_3CHCO_2H)_{16}]$ (0.006 g, 0.002 mmol) in THF (0.8 mL)

and adding it to the reaction mixture. The dispersion was then left to stir for 10 minutes. The pH was then brought to 9.5 and the tetra-functional cross-linker added. The molecular magnet loading was measured by UV-Vis spectroscopy: an aliquot (typically 3 mL) of the nanoparticle dispersion was freeze-dried and then redispersed in 1 mL THF. The solution was sonicated for 5 minutes and then filtered through a 0.22 μm PTFE filter to remove any colloidal object and its absorption at 615 nm was measured with a UV/Vis spectrophotometer Perkin Elmer Lambda 25 (Perkin Elmer, UK) using the calibration below. EPR spectra were recorded at 5 K on a Bruker EMX spectrometer at Q-band (approximately 34 GHz).

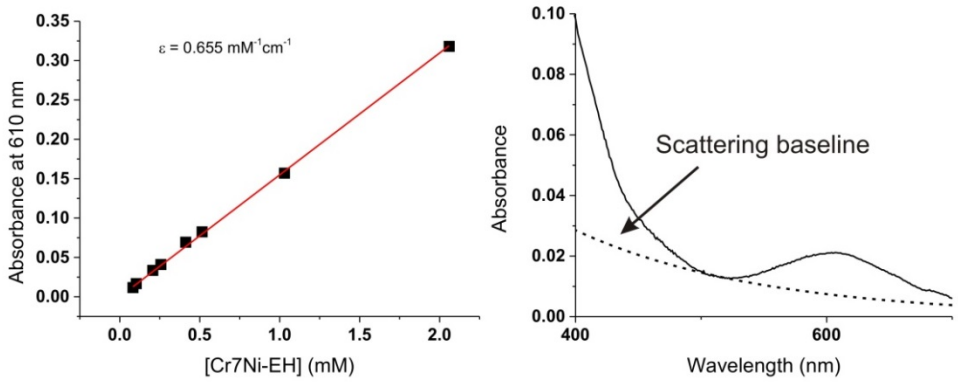

Figure 3.6-SI-3 *Left:* Calibration curve for the absorbance of 1 in THF solution. The calculated extinction coefficient; ε = 0.655 $mM^{-1}cm^{-1}$. *Right:* Vis spectrum of loaded nanoparticles (solid line) and scattering baseline used to correct the absorbance values of 1.

3.6.2 T_1/T_2 relaxivity measurements

Relaxivity measurements of water protons were performed on a Bruker Advance II 400MHz NMR spectrometer. T_1 measurements were performed using the t1ir, inversion recovery, pulse sequence. T_2 measurements were performed using the Car-Purcel-Meilboom-Gill (CPMG) inversion-recovery pulse sequence. The water peak intensities were then fit to a monoexponential function using Wolfram Mathematica.

3.6.3 Oxidation experiments with direct H_2O_2 addition

900 μL of PPS nanoparticles (loaded or unloaded at a concentration of 2.2 mg/mL - solutions contained 10% D_2O for NMR experiments) were introduced into a 1.5 mL Eppendorf tube. 100 μL of a H_2O_2 solution (5, 1 or 0.5% in PBS (x5) at pH 7.4) was added, for a final concentration of 0.5, 0.1 or 0.05 respectively (final nanoparticle concentration: 2 mg/mL). The system was left to react for 15, 30, 45, 60 or 120 min. KI (0.013 g, 0.078 mmol) was then added to neutralise the H_2O_2. Measurements were then performed on the sample.

3.6.4 Oxidation experiments with enzymatic production of H_2O_2

The reaction between oxygen and glucose mediated by glucose oxidase (EC 1.1.3.4) allows the *in situ* generation of hydrogen peroxide. Four vials containing 400 μL of a 2.5 mg/mL dispersion of nanoparticles and four with the same volume of plain buffer as a control were prepared. 50 μL of glucose 10, 5, 1 and 0.5 mM respectively were added followed by 50 μL of a 2.69 mg/mL solution of glucose oxidase (final nanoparticle concentration: 2 mg/mL). All the solutions were prepared in PBS (x5). The samples were incubated 1.5 hours at 37 °C and then analysed. The conversion of glucose was quantitative in all cases, as confirmed by the analysis of the hydrogen peroxide produced in the control samples (1, 0.5, 0.1 and 0.05 mM). Specifically, 100 μL of each solution (both the samples to be tested and the standards prepared for the calibration curve) were pipette in a 96-well plate, 50 μL of a freshly prepared 1 mg/mL solution of type I horseradish peroxidase and 50 μL of Substrate reagent B containing 3,3′,5,5′-tetramethylbenzidine were then added and the absorbance values at 420 and 650 nm were recorded on a BIOTek® Synergy 2 multi-mode microplate reader (NorthStar Scientific Ltd., Leeds, UK). If necessary, the samples were subsequently diluted with PBS in order to ensure the readings to be in the linear range of the calibration curve.

Table 3.6-SI-1 T_2 values as a function of the exposure to H_2O_2 [a].

	T_2 (msec)			T_1 (msec)	
	PBS	in H_2O_2 (0.5% wt.)	after H_2O_2 (KI treated[b])	PBS	after H_2O_2 (KI treated[b])
Control	3400 ± 93	54 ± 2	2242 ± 28		
Nanop.s	2840 ± 32	54 ± 3	2333 ± 17		
Nanop.s + **1**	659 ± 9	56 ± 3	333 ± 4	3100 ± 80	3280 ± 83

[a] 30 minutes incubation in the presence of 0.5% wt. H_2O_2.
[b] T_2 of water protons 90 minutes after the addition of KI, which allows for the complete degradation of residual H_2O_2 (see Figure 3.6-SI-4).

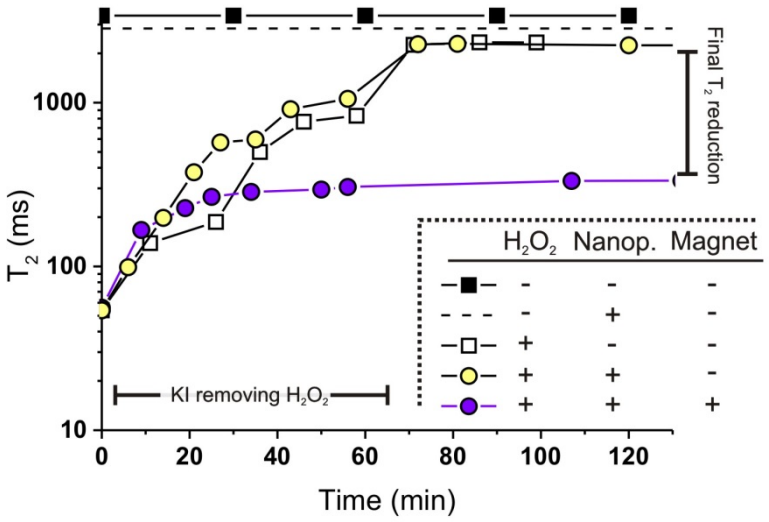

Figure 3.6-SI-4 The presence of unloaded particles has a negligible effect on T_2 (dashed line). On the contrary, the presence of H_2O_2 (0.5%)lowers the water T_2 to values in the region of 50-60 ms, irrespective of the presence of loaded or unloaded particles (empty and colored symbols at time zero). The removal of hydrogen peroxide by KI brings T_2 back to values comparable to those of pure water in the absence of particles (empty squares) or in the presence of unloaded particles (yellow circles). However, when magnet-loaded (8.42 nmol of 1/mg) particles where exposed to H_2O_2 and then treated with KI (purple circles) a clear effect of final T_2 reduction was apparent.

3.6.5 Supporting Information references

1. A. McRobbie, A. R. Sarwar, S. Yeninas, H. Nowell, M. L. Baker, D. Allan, M. Luban, C. A. Muryn, R. G. Pritchard, R. Prozorov, G. A. Timco, F. Tuna, G. F. S. Whitehead and R. E. P. Winpenny, *Chemical Communications*, 2011, **47**, 6251-6253.
2. L. Wang, G. Kilcher and N. Tirelli, *Macromolecular Bioscience*, 2007, **7**, 987-998.

4 A study on the molecular magnet composition and functionalization for their use in an oxidation responsive T_2 MRI contrast agent

Damien Jeanmaire,[a] Grigore Timco,[b] Jason Burke,[c] James P. S. Walsh,[b] Kaye J. Williams,[a] Richard E.P. Winpenny [b] and Nicola Tirelli*[c,d4]

[a]Manchester School of Pharmacy, University of Manchester, Oxford Road, Manchester M13 9PT, United Kingdom.

[b]School of Chemistry, University of Manchester, Brunswick Street, Manchester, M13 9PL, UK.
[c]School of Materials, University of Manchester, Grosvenor Street, Manchester, M1 7HS, UK.

[d]Institute of Inflammation & Repair, University of Manchester, Oxford Road, Manchester M13 9PT, United Kingdom.

* to whom correspondence should be addressed :

Prof. Nicola Tirelli, School of Materials and Institute of Inflammation and Repair / School of Medicine, University of Manchester, Oxford Road, Manchester, M13 9PT, United Kingdom

Tel.: +44 161 275 24 80.

Fax: +44 161 275 23 96

Email: nicola.tirelli@manchester.ac.uk

[4] **Author Contributions**: Grigore Timco – heterometallic wheel synthesis, Jason Burke – cell studies, James Walsh – EPR measurements, Kaye Williams/Richard Winpenny/Nicola Tirelli - Supervisors

Abstract

Here, we have combined an oxidation-sensitive material with molecular magnets in order to obtain an oxidation responsive T_2 MRI contrast agent. In particular, we have studied the effect of Cr/Ni and Cr/Gd heterometallic ring composition on their loading in poly(propylene sulfide) (PPS) nanoparticles as well as their effect on water T_2 relaxation before and after exposure to oxidants. The loaded nanoparticles were exposed to different concentrations of hydrogen peroxide (H_2O_2), a Reactive Oxygen Species (ROS) typically found in inflammatory reactions in the body.

It was found that the loading of the molecular magnets has no significant effect on the properties of the nanoparticles or the molecular magnets. The difference in magnet composition did however, have an effect on both the loading efficiency of the molecular magnets as well as the final nanoparticles' relaxivity in both a reduced and oxidised state. Using a 'bulky' ligand on the outside of the molecular magnet protects it from hydrolysis during loading however reduces its effect on T_2 relaxation. On the contrary, smaller ligands cause a greater initial uptake of water molecules during synthesis and therefore a reduced response upon oxidation; however have an increased overall relaxivity.

This compromise can be seen as a powerful tool in contrast agent development using these compounds as the system can be finely tuned depending on the final application.

4.1 Introduction

The primary physical parameters that must be taken into consideration when developing an MRI contrast agent are relaxivity and stability. Typically, the biocompatible chelate or carrier that is used is designed around the relaxation mechanism of the contrast agent. In 1984, the first gadolinium contrast agent was developed , gadolinium(III) diethylene-triaminepentaacetate (Gd-DTPA; Magnevist)[1]. The chelate DTPA was used as it left one coordination site on the Gd ion free to allow for magnetic exchange between itself and surrounding water molecules. In addition, the chelate prevented the highly toxic Gd ion to interact with the body. To this date, all MRI contrast agents used for diagnostics are gadolinium based[2]. However it was discovered that the common chelating molecules used with Gd were in fact thermodynamically instable and could undergo ligand exchange and transmetallisation[3-5]. In 2006, the first cases of nephrogenic systemic fibrosis (NSF) were reported in patients who had renal dysfunction and had been administered gadolinium contrast agents[6]. Despite these issues, gadolinium contrast agents are still being used. It is therefore of utmost importance that a safe replacement be found.

Cellular microenvironments are regulated by strict physico-chemical properties such as the presence of specific enzymes and signalling markers as well as a regulated pH and REDOX potential. These can be destabilised in the presence of pathological conditions. The ability to detect these changes is a powerful tool in monitoring healthy and diseased areas in the body. Current trends in contrast agent research are focused on MRI contrast agents that can target and respond to these conditions. The majority of responsive CAs that have been developed are T_1 (negative) based, this is due to their contrast mechanism. Due to the necessity of a water binding site on the complex, the development of systems where the free coordination site can be protected and deprotected based on environmental factors provides an effective switch between a low signal protected state and a high signal de-protected state. On the other hand, T_2 (positive) CAs, acting solely by dipole interactions, are more difficult to 'switch-

off'. Typically, T_2 CAs are based on either passive targeting via the enhanced permeability and retention effect (EPR) or use targeting ligands on the surface of the nanoparticles. The EPR effect allows for the nanoparticles to spontaneously accumulate in areas where there are abnormal blood vessels, such as in tumours. One such example of the application of this effect is from Lee et al., using iron oxide nanoparticles, coated in an antibiofouling polymer; their reduced uptake via the RES allows them to circulate long enough to exploit the EPR effect[7].

There exist many different triggers to which a contrast agent can be designed to respond to[8-10]. Kim et al. have incorporated Gd-DTPA into a pH responsive PEGy-lated micelle. In cancerous environments, where the pH drops from a physiological 7.4 to 6.5, the micelles disassemble and allow for the Gd chelates to diffuse through the tumour[8]. Duimstra et al. have shown a CA activated by β-glucuronidase, an oncologically significant enzyme[10].

Here we will be focusing on REDOX responsive MRI contrast agents. Two recently published reviews covering the state of REDOX- and hypoxia-responsive MRI contrast agents provide a comprehensive overview of the different targeting mechanisms associated to REDOX/hypoxic environments[11, 12]. One such mechanism is to use selective binding to reduced thiol groups by attaching a pendant thiol on a Gd chelate. This allows for binding to Human Serum Albumin (HSA) via a dithiol link between the free thiol on the CA and the thiol of cysteine-34 on HSA[13]. This link increases the molecular weight of the complex hence reducing its rotational correlation time which in turn increases its relaxivity. Martinelli et al. have encapsulated Gd chelates into cleavable β-cyclodextrin nanocapsules cross-linked via disulfide bridges. This encapsulation increases the rotational correlation time of the Gd complexes increasing their relaxivity. In the presence of reducing agents, the nanocapsules are degraded and the Gd chelates are released. The resulting decrease in rotational correlation time of the Gd complexes causes a drop in relaxivity[14].

Much work has been done on CA responsive to reducing conditions, however oxidising conditions in the body are just as important to detect. Inflammatory reactions, ranging from rheumatoid arthritis to Alzheimer's Disease, are subject to oxidative conditions; in particular the presence of inflammation-related oxidants, Reactive Oxidant Species (ROS), the most common of which are superoxide anion (O_2^-), hydrogen peroxide (H_2O_2) and hypochlorite (ClO^-)[15-18].

Here, we will be discussing the synthesis and characterisation of an oxidant sensitive T_2 MRI contrast agent. An oxidation responsive nanoparticle based on the hydrophobic organic polysulfide poly(propylene sulfide) (PPS), will provide the responsive base to the contrast. Encapsulated in the nanoparticles, molecular nano-magnets will provide the contrast enhancement.

The molecular nano-magnets presented in this chapter have been previously reported in literature. Hetero-metallic structures in which there are antiferromagnetic interactions between neighbouring metal ions were first reported by Larsen et al. in 2003[19]. Larsen showed that if one of the metal ions in a homometallic ring structure was changed to induce an imbalance in spins, it could lead to a structure with a non-zero ground state spin.

We have previously reported the synthesis of PEGy-lated/cross-linked PPS nanoparticles as oxidation sensitive nano-carriers[20, 21]. In the presence of ROS (H_2O_2 or ClO^-), the polysulfides are oxidised to poly-sulfoxides/sulfones altering the polarity of the core from hydrophobic to hydrophilic[22, 23]. This change in polarity allows for water to slowly ingress into the core of the nanoparticles and increases its interaction with the encapsulated molecular nano-magnets.

In this chapter we study the effect of the molecular nanomagnet's composition on its loading efficiency and contrast enhancement. The PPS nanoparticles used all have a z-average size of around 50 nm and a degree of polymerisation of 90. Four different nanomagnets with different external ligands (pivalic acid, 2-ethylhexanoic acid and 3,5-diisopropylsalicylic acid) as well as different metallic cores have been studied. They have a chemical formula of:

(**1**;Cr_7Ni-*piv*): $[(C_3H_7)_2NH_2][Cr_7NiF_8((CH_3)_3CCO_2H)_{16}]$,

(**2**;Cr_7Ni-*eth*): $[(C_3H_7)_2NH_2][Cr_7NiF_8(CH_3(CH_2)_3CHCO_2H)_{16}]$,

(**3**;Cr_7Ni-*sal*): $[C_3H_7NH3][Cr_7NiF_8(C_{13}H_{18}O_3)_{16}]$,

(**4**; $Cr_{12}Gd_4$): $[((C_2H_5)_2NH_2)_2(Cr_{12}Gd_4F_{21}((CH_3)_3CCO_2H)_{29}]$ [19, 24-26].

4.2 Experimental section

4.2.1 Materials

All reagents and solvents were purchased from Sigma Aldrich (Gillingham, UK) and used without further purification.

4.2.2 Physico-chemical characterization

1H NMR spectra were recorded on 1% wt. solutions in deuterated chloroform using a 400 MHz Bruker spectrometer (Bruker UK Limited, UK). FT-IR spectra were recorded in ATR mode (Golden Gate) on a Tensor 27 Bruker spectrometer (Bruker UK Limited, UK) equipped with a 3000 Series TM High Stability Temperature Controller with RS232 Control (Specac, UK). The spectra of nanoparticles upon oxidation with H_2O_2 were recorded by allowing a drop of the oxidation mixture (typically 20-50 μL) to dry at 50 °C for ca. 3 min on the bottom plate of the Golden Gate ATR accessory. *Loading measurements*. Nanoparticle loading was measured by UV-Vis spectroscopy. 3 mL of nanoparticle dispersion was freeze-dried then redispersed in 1mL THF. The solution was sonicated for 5 minutes to break up the nanoparticles and release the molecular nanomagnets. The solution was then filtered through a 0.22μm syringe PTFE filter to remove any suspended polymer and its absorption at 615 nm was measured with a UV/Vis spectrophotometer Perkin Elmer Lambda 25 (Perkin Elmer, UK). *Dynamic light scattering (DLS)*. Size distributions and scattering intensity of nanoparticles were measured with the help of a Zetasizer Nano ZS Instrument (Model ZEN3500, Malvern Instruments Ltd, UK). All the samples were analyzed at an angle of 173° and a temperature of 25°C. *Electron paramagnetic resonance*

(EPR). EPR measurements on the molecular magnets and the loaded nanoparticles was performed on a Bruker spectrometer. Compounds **1**, **2** and **4** were measured at 5 K at Q-band (approximately 34 GHz). Compound **3** was measured at 294 K with X-band (approximately 9.4 GHz).

4.2.3 Preparative operations

Preparation of low molecular weight compounds. The molecular magnets were prepared according to literature procedures developed in the group of Winpenny. Compound **1** was prepared according to Larsen et al.[19]. Compound **2** was prepared according to A. McRobbie et al.[24]. Compound **3** is isostructural with $[PrNH_3][Cr_7CoF_8(O_2C^tBu)_{16}]$, Sanudo et al.[25]. Compound **4** was prepared according to Ghirri et al.[26]. The protected bifunctional initiator used to start the episulfide emulsion polymerization, S,S'-[ethane-1,2-diylbis(ozyethane-1,1-diyl)] diethanethioate, was prepared according to a literature procedure developed in the group of Tirelli[27].

Preparation of cross-linked nanoparticles. 80 mg of Pluronic F127 were dissolved in 10 mL of degassed MilliQ water in a 25 mL Radley's Carousel parallel reactor tube (for a target particle size of ~50 nm; the targeted *overall DP* was set at 90). The system was continuously stirred at 1,000 rpm for 10 min under an argon atmosphere. In a separate vial, under argon atmosphere, the protected initiator (0.013 g, 0.061 mmol) was mixed with 0.5 M CH3ONa in methanol (245 μL) for 10 minutes, to deprotect it. The deprotected initiator and PS (0.4 g, 5.48 mmol, corresponding to 45 PS equivalents per thiol group; overall DP = 90) were then added to the reaction flask, the reaction mixture was further stirred for 10 min, and 2 equivalents of DBU (0.018 g, 0.112 mmol) were finally added to initiate the polymerization. The reaction mixture was stirred under inert conditions for 2 h; the pH was lowered to 9.5 by the addition of acetic acid, and 0.5 equivalents of tetra-functional cross-linker pentaerythritol tetraacrylate (0.03 mmol, 0.010 g) dissolved in dichloromethane (0.3 mL) were then added to the reaction mixture. After 1 minute the pH was brought to 7.4 by adding 5 mL of PBS (50 mM, pH 7.4), in order to minimize the hydrolysis of the cross-linkers. The suspension was additionally stirred for 16 h before purification by ultrafiltration (Amicon

Ultrafiltration Cell Model 8200, Millipore, UK) against MilliQ water through 300 kDa MWCO regenerated cellulose membranes (Spectrum Laboratories, UK). For any further use, the concentration of nanoparticles was determined gravimetrically after freeze drying samples of their dispersions. ATR FT-IR (thin film): 2956 (ν_{as} CH_3), 2920 (ν_{as} CH_2), 2856 (ν_s CH_2), 1740 (ν C=O), 1450 (δ_{as} CH_3), 1372 (δ_s CH_3), 1170 (ν_{as} C-O-C, ester), 1100 (ν_{as} C-O-C in Pluronic F-127), 800-600 cm^{-1} (ν C-S in PPS).

Loading of the molecular magnets in PPS nanoparticles. The above preparative procedure was modified by adjusting the pH of the reaction mixture to 7.4 after polymerisation, dissolving the molecular nanomagnets (**1** (0.006 g, 0.0026 mmol); **2** (0.006 g, 0.002 mmol); **3** (0.006 g, 0.0014 mmol); **4** (0.006 g, 0.0013 mmol) in THF (0.8 mL) and adding it to the reaction mixture. The dispersion was then left to stir for 10 minutes. The pH was then brought to 9.5 and the tetra-functional cross-linker added.

4.2.4 Experimental procedures

Oxidation of nanoparticles. 900 μL of PPS nanoparticles (loaded or unloaded at a concentration of 2.2 mg/mL - solutions contained 10% D2O for NMR experiments) were introduced into a 1.5 mL Eppendorf tube. 100 μL of a H_2O_2 solution (5, 1 or 0.5% in PBS (x5) at pH 7.4) was added, for a final concentration of 0.5, 0.1 or 0.05 respectively (final nanoparticle concentration: 2 mg/mL). The system was left to react for 15 min. KI (0.013 g, 0.078 mmol) was then added to neutralise the residual H_2O_2. It is well reported in literature that the presence of H_2O_2 in solution has a large effect on the T_2 relaxivity of water, it is therefore necessary to remove excess hydrogen peroxide prior to T_2 measurements[28]. Measurements were then performed on the sample.

T_2 relaxivity measurements. T_2 relaxivity measurements of water protons were performed on a Bruker Advance II 400MHz NMR spectrometer using the Car-Purcel-Meilboom-Gill (CPMG) inversion-recovery pulse sequence. The water

peak intensities were then fit to a monoexponential function using Wolfram Mathematica.

Cell Viability Studies. Raw264.7 macrophage cells (Sigma Aldrich) were seeded at a density of 25,000 cells/well in a 96-well format (Corning® Costar®) and allowed to adhere overnight in normal cell culture media (DMEM containing; 10% FBS, 1% Pen/Stryp and 2mM Glutamine). Thereafter, cells were treated for 8 hours in media containing various concentrations of nanoparticles; 0.5, 1, 2 and 4 mg/mL. Following treatment, a one-step MTS solution (CellTiter 96® AQueous Assay – Promega) was used to assess cell metabolic activity, followed by treatment with a bicinchoninic acid (BCA) assay (Sigma Aldrich) to normalise results against the total protein content. Cells were treated with 100 ng/mL of LPS as a control.

Inflammatory Response – Nitrite Production. Raw264.7 macrophage cells (Sigma Aldrich) were seeded at a density of 25,000 cells/well in a 96-well format (Nunc™ MicroWell™ 96-Optical Bottom Plates – Black) and allowed to adhere overnight in normal cell culture media (DMEM containing; 10% FBS, 1% Pen/Stryp and 2mM Glutamine). Thereafter, cells were treated for 8hrs in media containing various concentrations of nanoparticles; 0.5, 1, 2 and 4 mg/ml. Following treatment, a Griess assay system (Promega) was used to quantify the levels of nitrite within culture supernatants. Results were normalised against total protein content with the use of a BCA assay (Sigma Aldrich).

4.3 Results and Discussion

4.3.1 Synthesis and loading of nanoparticles

We have previously shown that PPS nanoparticles can be synthesised with a controlled size distribution as well as a uniform degree of polymerisation (DP)[20]. In this study we decided to use nanoparticles with a hydrodynamic size of about 50 nm, the smallest size attainable with the emulsion polymerisation process, for two specific reasons. First, 50 nm particles will have a more controlled bio-distribution when compared to ultra-small nanoparticles (< 10 nm) or larger, sub-micron particles, preventing uptake by macrophages or rapid renal

clearance, as in the case with small molecular weight Gd complexes[29]. Second, the larger surface to volume ratio increases the exchange area between the nanoparticles and the water environment. This increase in surface area is expected to increase the response to oxidants, allowing for the rapid detection of small quantities of oxidant.

The choice of solvent used to load the nanomagnets into the core of the nanoparticles is crucial. It must satisfy a selection of requirements: the solvent must be non-polar enough to solubilise the nanomagnets, be miscible with water to allow for it to fully mix with the dispersion, however still be able to diffuse into the hydrophobic core of the nanoparticles. In addition, the solvent must be easily removed after synthesis. The loading was initially performed with dichloromethane (DCM) as the solvent. This was chosen as it solubilises the magnets well, has a low polarity index (3.1), and a very low boiling point (39°C) allowing for easy evaporation from the solution. However when the magnets were added to the dispersions using DCM, a green precipitate was quickly formed. This is probably due to the rapid evaporation of the DCM before the magnets are able to diffuse into the core of the nanoparticles, exposing the hydrophobic nanomagnets to a water environment, hydrolysing them and forming chromium-oxide.

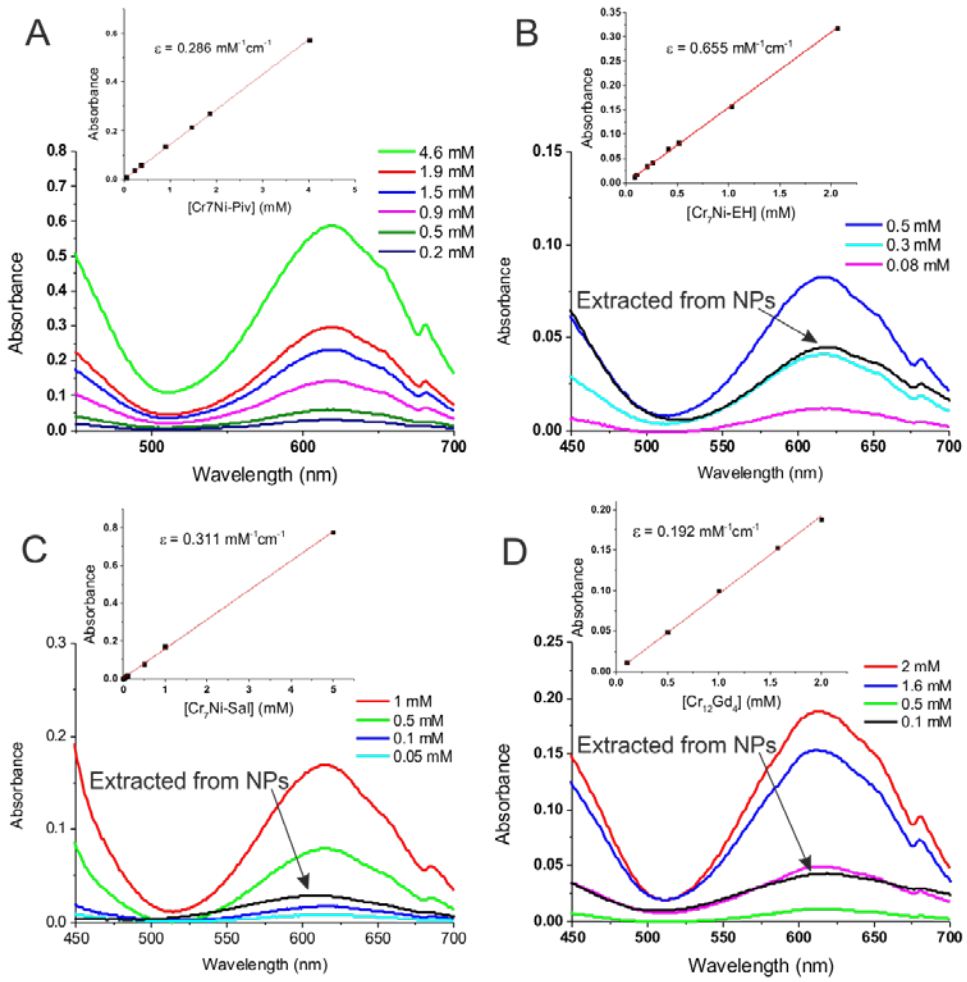

Figure 4.3-1 Vis spectra of 1(A), 2(B), 3(C) and 4(D) in THF at different concentrations in reference solutions (coloured lines) and after swelling and sonication of freeze dried nanoparticles (for compounds 2, 3 and 4, black line, corrected of a scattering baseline). Inset, corresponding UV-Vis calibration curves with extinction coefficient.

When tetrahydrofuran (THF) was used to load the nanomagnets, no precipitate was formed for compounds **2**, **3** and **4**; instead the dispersion acquired a uniform green tinge. The integrity of the magnets following this process was confirmed by both visible absorption and EPR. Figure 4.3-1 shows that the visible absorption of the nanomagnets, after having been extracted from the loaded nanoparticles, is unchanged. In addition, the EPR spectrum of the loaded nanoparticles shows the characteristic signal from intact molecular nanomagnets, further showing the successful loading of the nanoparticles (Figure 4.3-2).

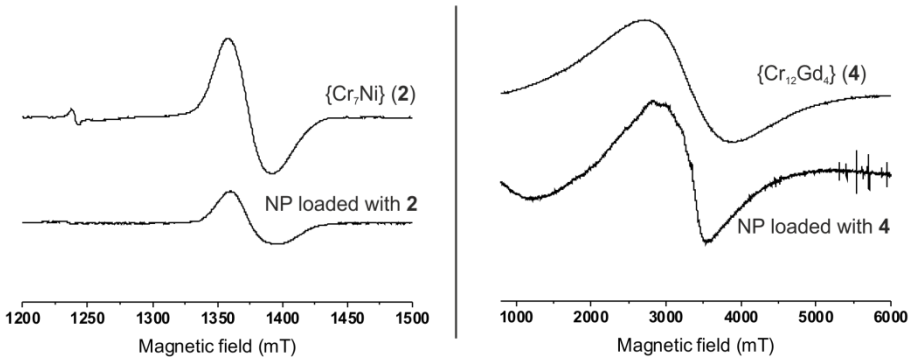

Figure 4.3-2 EPR spectra of 2 (left) and 4 (right) in pure form (top) and in freeze dried nanoparticles (bottom). Spectra of 1 and 3 are superimposable with 2 due to the common Cr_7Ni backbone.

The visible spectrum was also used to assess the loading of the nanoparticles. The absorption peak at 615 nm was used (common to all the molecular magnets) and compared to the respective calibration curve. The saturation loading for magnets **2**, **3** and **4** was found to be 2.5 wt% (8.42 nmol/mg of NPs), 2.7 wt% (6.4 nmol/mg of NPs) and 3.94 wt% (8.54 nmol/mg of NPs) respectively.

Dynamic light scattering (DLS) measurements show that the loading step does not affect the size distribution of the nanoparticles, resulting in a z-average size of about 50 nm (Figure 4.3-4 C). It can therefore be assumed that the solvent used to load the magnets into the nanoparticles has been completely removed by the end of the synthesis.

In the case of compound **1**, green precipitate was still observed after changing to THF as the loading solvent. Both the visible absorption measurements and EPR measurements resulted in negative readings. We believe this to be due to the choice of ligands used. In the case of the Cr_7Ni heterometallic wheels, using bulkier ligands, such as ethylhexanoic acid and diisopropylsalicylic acid, forms a barrier that “protects” the internal structure of the rings from hydrolysis during the loading. However, using pivalic acid as a ligand for the rings does not provide enough protection between the aqueous environment and the sensitive internal structure of the rings.

It is worth mentioning that compound **4** also uses pivalic acid as a ligand however it can be loaded into the nanoparticles without precipitation. It is believed that this is due to the presence of the gadolinium tetrahedron bridged by fluoride atoms. This forms a very stable complex more favourable than complexation with water[30]. In contrary, the Ni-F bond in compound **1** is less stable, especially in slightly basic conditions, when the pH is increased prior to cross-linking, the ring breaks apart forming nickel(II) hydroxide, a green coloured compound.

4.3.2 T2 characterisation

T_2 relaxivity measurements of the loaded nanoparticles show that, prior to oxidation, they already have an effect on the relaxation rate of water protons. Nanoparticles loaded with compounds **2** and **4** have r_2 values of 102 and 179 $mM^{-1}s^{-1}$ respectively. Whereas compound **3** has a relaxivity of only 15 $mM^{-1}s^{-1}$ (calculations based on the molar concentration of rings, Figure 4.3-3). This inherent relaxivity of the nanoparticles would allow them to be traced through the body.

The difference in relaxivities between the three compounds can be attributed to both the metal ions that are used as well as the ligands. As expected, the gadolinium containing compound (**4**) has the highest relaxivity due to the high spin of Gd. Compounds **2** and **3** however have the same inner structure (Cr_7Ni), their sole difference is the carboxylate that is used. Due to the lack of binding sites, the Cr_7Ni rings interact with water solely via dipolar (outer-sphere) interactions. The efficiency of this interaction is governed by a $1/r^6$ term, where r is the metal-proton distance. As diisopropylsalicyclic acid is bulkier than ethylhexanoic acid, it is reasonable to suggest that it creates a larger protection zone between the metal ions and the water protons. This slight increase results in a large effect on the final relaxivity of the compound. This can clearly be seen in the un-oxidised r_2 values for both systems.

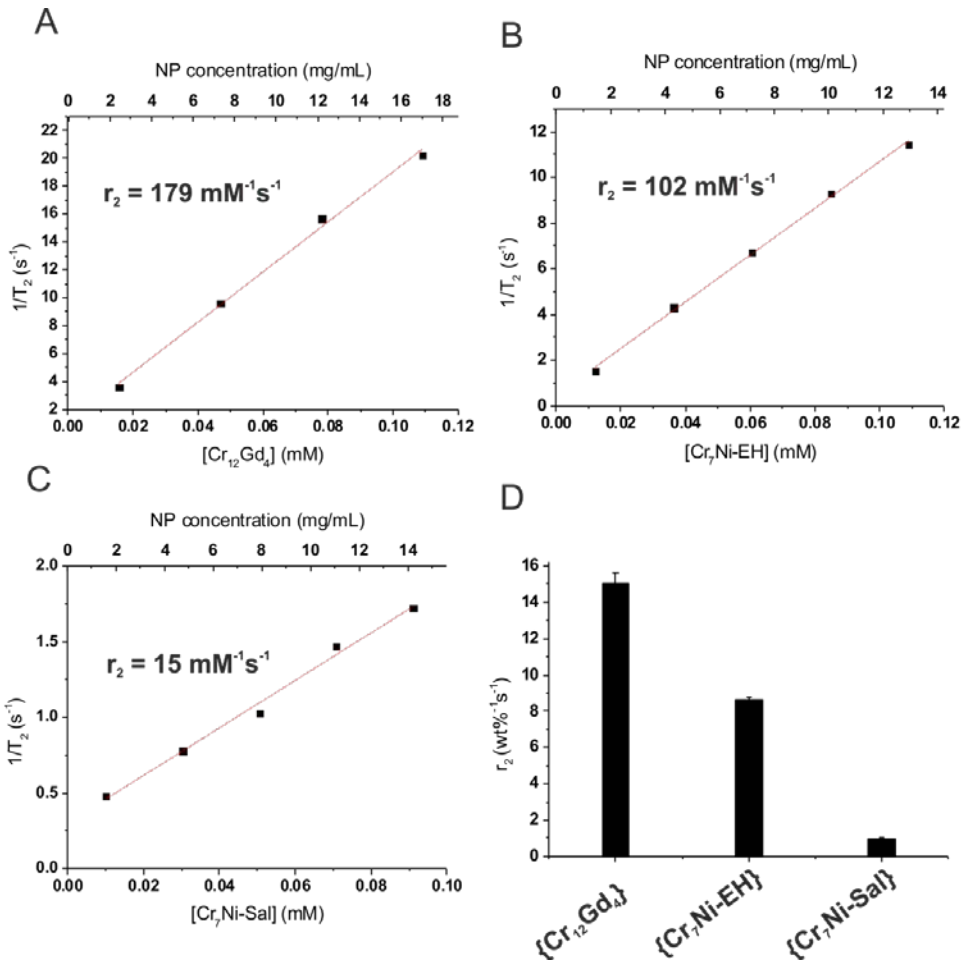

Figure 4.3-3 A, B, C: Concentration of molecular magnet plotted against $1/T_2$ fit with a linear function in order to obtain the r_2 relaxivity of the loaded nanoparticles in a reduced state (4, A; 2, B; 3, C). Corresponding nanoparticle concentrations also indicated (top axis). D: r_2 relaxivities of loaded nanoparticles displayed in terms of wt% of molecular magnets. (n=3)

Due to their inherently high r_2 in a reduced state, it is therefore feasible to say that the nanoparticles loaded with compounds **2** and **4** could be used as CAs in their own right – current commercially available T_2 contrast agents, Feridex and Resovist have relaxivities of 98.3 $mM^{-1}s^{-1}$ and 82 $mM^{-1}s^{-1}$ respectively[31, 32].

4.3.3 Hydrogen peroxide oxidation

Upon oxidation with hydrogen peroxide, a significant decrease in T_2 was observed for nanoparticles loaded with **2** and **3** (up to 50% decrease in T_2), however very little decrease was seen with compound **4** (Figure 4.3-4 A). This difference in change in relaxivity can be attributed to the difference in

composition of the nanomagnets. During the synthesis of PPS nanoparticles, despite the hydrophobicity of the core, there is still some water ingress into the core due to the nature of the emulsion synthesis. When loading the nanoparticles with molecular magnets with THF, a water miscible solvent, it is possible that a small number of water molecules diffuse into the core as well. When comparing pivalic acid with ethylhexanoic acid and diisopropylsalicyclic acid, its smaller size would allow more water molecules to diffuse into the nanoparticle within the same volume of solvent. This would explain both the initial relaxivities in the reduced state (r_2(**4**) > r_2(**2**) > r_2(**3**)) as well as the change in relaxivity upon oxidation, being directly related to the steric hindrance of the outer ligand.

It is worth noting that the nanoparticles' response to oxidation is non-linear. Figure 4.3-4 A clearly shows that the drop in T_2 following oxidation is independent of oxidant concentration. This demonstrates that upon exposure to small quantities of hydrogen peroxide, the matrix quickly become permeable to water. However only negligible swelling was observed for all three nanoparticles; this was confirmed via dynamic light scattering (Figure 4.3-4 C). We have previously shown that to obtain complete oxidation of the polymer network, it is necessary to expose the nanoparticles to high concentrations of oxidant (> 5% wt) for extended periods of time (2-3 hrs). It is therefore possible to assume that, in this case, the polymer network is only minimally oxidised. FT-IR was used to show that only a negligible increase in the S=O stretching peak was observed, confirming the lack of extended oxidation of the network (Figure 4.3-4 B).

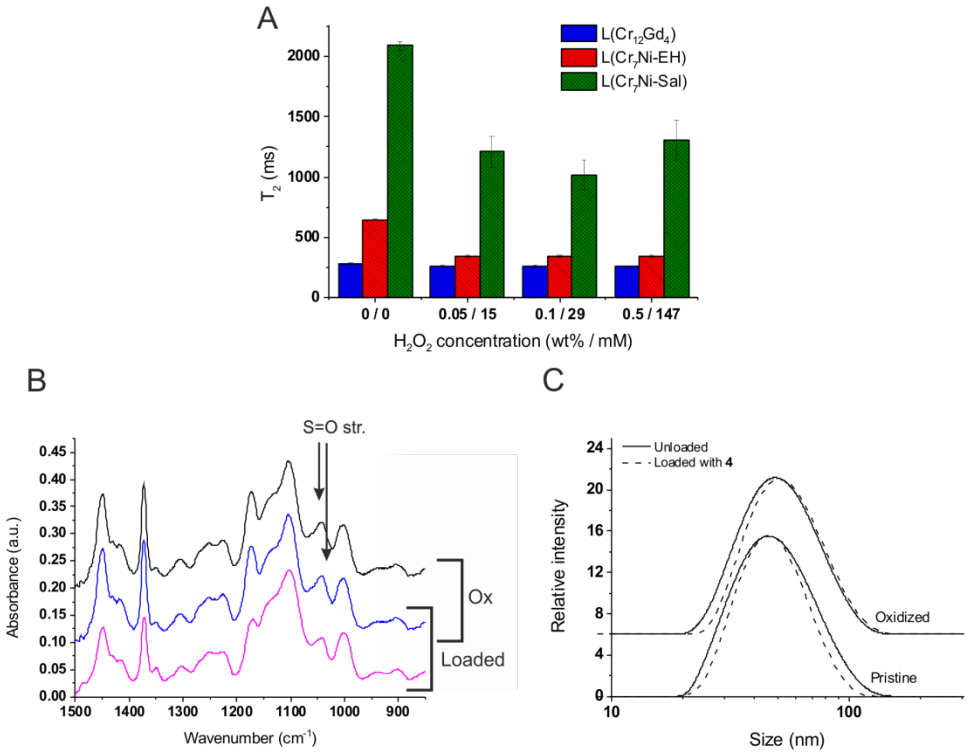

Figure 4.3-4 A: T_2 of water protons in the presence of loaded nanoparticles as a function of H_2O_2 concentration (0% wt – 0.5% wt). Nanoparticles at a concentration of 2 mg/mL exposed to H_2O_2 for 15 min followed by addition of KI to quench remaining H_2O_2. B: Exposure to 0.5% H2O2 for 30 minutes is known to introduce only small amounts of sulfoxide groups, as it can be seen from the very moderate increase of the band at 1050 cm^{-1} due to a component associated to S=O stretching. The presence of 4 introduces no appreciable difference in the IR spectra (compare black and blue spectra). Identical results were obtained for nanoparticles loaded with 2 and 3. C: The loading of the polysulfide nanoparticles with 4 (8.54 nM/mg of particle) did not change their size distribution. In addition, oxidation with 0.5% H_2O_2 for 30 min negligibly shifted the size distribution up independent of the loading.

4.3.4 Cell viability studies

We have previously shown that unloaded PPS nanoparticles are non-cytotoxic. Cytotoxicity studies were performed with PPS nanoparticles loaded with 2. Figure 4.3-5 shows that the loaded nanoparticles show no effect on cell viability over a range of concentrations (0.5 – 4.0 mg/mL). In addition, cell nitrile production was measured to assess any inflammatory response of the cells to the presence of the nanoparticles. A small amount was produced at the highest

nanoparticle concentration of 4 mg/mL, however still negligible compared to the LPS control.

The non-cytotoxicity of the loaded nanoparticles demonstrates that the molecular magnets are completely encapsulated in the nanoparticles and there is no leaching of the magnets into the surrounding medium.

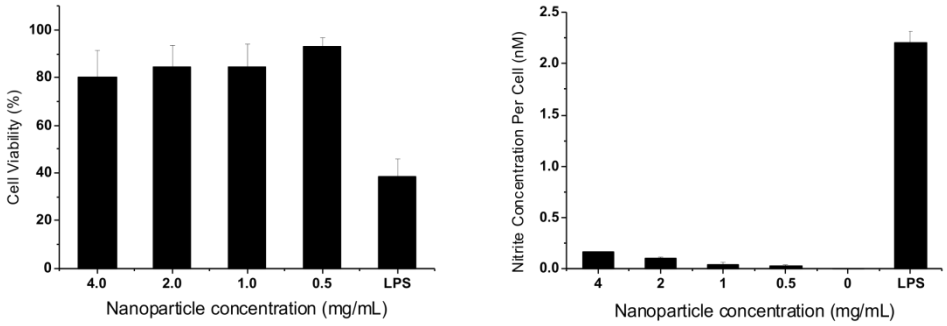

Figure 4.3-5 It is known that unloaded polysulfide nanoparticles are non-cytotoxic at low concentrations[20], it can be seen that the presence of 2 in the core of the nanoparticles does not affect detrimentally the cell viability (left). In addition, the lack of nitrite production in the presence of the loaded nanoparticles shows that there is no inflammatory response from the cellular environment (right). LPS was used as a positive control at a concentration of 100 ng/mL.

4.4 Conclusions

We have shown that molecular magnets with different outer ligands can be successfully loaded into polysulfide nanoparticles without significantly changing either of their properties. Upon oxidation with small quantities of hydrogen peroxide, a drop in T_2 is observed in all systems. This drop is independent of oxidant concentration resulting in an off/on switch.

The carboxylate that is used on the magnet has a dramatic impact on both the loading and the system's response to oxidation. Using a bulky ligand such as 3,5-diisopropylsalicylic acid results in a very low relaxivity in the reduced state however due to the increased metal-proton distance, it still has a low relaxivity

after oxidation. On the contrary, a small carboxylate such as pivalic acid allows for a high loading capacity and initial relaxivity however due to its small size, more water molecules are able to diffuse into the core with it during synthesis. The presence of water in the core prior to oxidation minimizes the drop in T_2 observed after oxidation. Cr_7Ni-EH demonstrates the best of both situations. Prior to oxidation, the T_2 of water protons is low enough for it to be useful as a contrast agent in its own right. Following oxidation and independent of oxidant concentration, a drop in T_2 (about 50%) is observed. It is therefore possible to tune the contrast agent's magnetic properties before and after oxidation by changing the carboxylate that is used.

4.5 References

1. H. J. Weinmann, R. C. Brasch, W. R. Press and G. E. Wesbey, *American Journal of Roentgenology*, 1984, **142**, 619-624.
2. V. C. Pierre, M. J. Allen and P. Caravan, *J Biol Inorg Chem*, 2014, **19**, 127-131.
3. W. P. Cacheris, S. C. Quay and S. M. Rocklage, *Magnetic Resonance Imaging*, 1990, **8**, 467-481.
4. J.-M. Idée, M. Port, I. Raynal, M. Schaefer, S. Le Greneur and C. Corot, *Fundamental & Clinical Pharmacology*, 2006, **20**, 563-576.
5. A. D. Sherry, P. Caravan and R. E. Lenkinski, *Journal of Magnetic Resonance Imaging*, 2009, **30**, 1240-1248.
6. T. Grobner, *Nephrol. Dial. Transplant.*, 2006, **21**, 1104-1108.
7. H. Lee, E. Lee, D. K. Kim, N. K. Jang, Y. Y. Jeong and S. Jon, *Journal of the American Chemical Society*, 2006, **128**, 7383-7389.
8. K. S. Kim, W. Park, J. Hu, Y. H. Bae and K. Na, *Biomaterials*, 2014, **35**, 337-343.
9. A. Y. Louie, M. M. Hüber, E. T. Ahrens, U. Rothbächer, R. Moats, R. E. Jacobs, S. E. Fraser and T. J. Meade, *Nat Biotech*, 2000, **18**, 321-325.
10. J. A. Duimstra, F. J. Femia and T. J. Meade, *Journal of the American Chemical Society*, 2005, **127**, 12847-12855.
11. Q. N. Do, J. S. Ratnakar, Z. Kovacs and A. D. Sherry, *ChemMedChem*, 2014, **9**, 1116-1129.
12. P. B. Tsitovich, P. J. Burns, A. M. McKay and J. R. Morrow, *Journal of Inorganic Biochemistry*, 2014, **133**, 143-154.
13. B. Jagadish, G. P. Guntle, D. Zhao, V. Gokhale, T. J. Ozumerzifon, A. M. Ahad, E. A. Mash and N. Raghunand, *J. Med. Chem.*, 2012, **55**, 10378-10386.
14. J. Martinelli, M. Fekete, L. Tei and M. Botta, *Chemical Communications*, 2011, **47**, 3144-3146.

15. V. Adler, Z. Yin, K. D. Tew, Z. Ronai, *Oncogene*, 1999, **18**, 6104-6111.
16. I. Rahman and W. MacNee, *European Respiratory Journal*, 2000, **16**, 534-554.
17. V. V. Khutoryanskiy and N. Tirelli, *Pure and Applied Chemistry*, 2008, **80**, 1703-1718.
18. C. D. Lux, S. Joshi-Barr, T. Nguyen, E. Mahmoud, E. Schopf, N. Fomina and A. Almutairi, *Journal of the American Chemical Society*, 2012, **134**, 15758-15764.
19. F. K. Larsen, E. J. L. McInnes, H. E. Mkami, J. Overgaard, S. Piligkos, G. Rajaraman, E. Rentschler, A. A. Smith, G. M. Smith, V. Boote, M. Jennings, G. A. Timco and R. E. P. Winpenny, *Angewandte Chemie International Edition*, 2003, **42**, 101-105.
20. D. Jeanmaire, J. Laliturai, A. Almalik, P. Carampin, R. d'Arcy, E. Lallana, R. Evans, R. E. P. Winpenny and N. Tirelli, *Polymer Chemistry*, 2014, **5**, 1393-1404.
21. G. Kilcher, C. Duckham and N. Tirelli, *Langmuir*, 2007, **23**, 12309-12317.
22. P. Carampin, E. Lallana, J. Laliturai, S. C. Carroccio, C. Puglisi and N. Tirelli, *Macromolecular Chemistry and Physics*, 2012, **213**, 2052-2061.
23. A. Napoli, M. Valentini, N. Tirelli, M. Muller and J. A. Hubbell, *Nature Materials*, 2004, **3**, 183-189.
24. A. McRobbie, A. R. Sarwar, S. Yeninas, H. Nowell, M. L. Baker, D. Allan, M. Luban, C. A. Muryn, R. G. Pritchard, R. Prozorov, G. A. Timco, F. Tuna, G. F. S. Whitehead and R. E. P. Winpenny, *Chemical Communications*, 2011, **47**, 6251-6253.
25. E. C. Sañudo, T. B. Faust, C. A. Muryn, R. G. Pritchard, G. A. Timco and R. E. P. Winpenny, *Inorganic Chemistry*, 2009, **48**, 9811-9818.
26. A. Ghirri, V. Corradini, C. Cervetti, A. Candini, U. del Pennino, G. Timco, R. J. Pritchard, C. A. Muryn, R. E. P. Winpenny and M. Affronte, *Advanced Functional Materials*, 2010, **20**, 1552-1560.
27. L. Wang, G. Kilcher and N. Tirelli, *Macromolecular Bioscience*, 2007, **7**, 987-998.
28. L. Buljubasich, B. Blümich and S. Stapf, *Chemical Engineering Science*, 2010, **65**, 1394-1399.
29. S. Aime and P. Caravan, *Journal of Magnetic Resonance Imaging*, 2009, **30**, 1259-1267.
30. N. K. Chaudhuri, R. M. Sawant and K. L. Ramakumar, *Rev. Inorg. Chem.*, 2001, **21**, 331-368.
31. Y.-X. J. Wang, *Quant. Imaging Med. Surg.*, 2011, **1**, 35-40.
32. D. Nordmeyer, P. Stumpf, D. Groeger, A. Hofmann, S. Enders, S. B. Riese, J. Dernedde, M. Taupitz, U. Rauch, R. Haag, E. Ruehl and C. Graf, *Nanoscale*, 2014, **6**, 9646-9654.

11 Conclusion

The development of responsive and targeted MRI contrast agents is an active field however the majority of systems that have been developed have not strayed far from the classically used gadolinium complexes for T_1 CAs, or iron oxide nanoparticles for T_2 CAs. It is therefore of scientific interest to broaden horizons and explore the use of unique magnetic compounds for use as contrast agents such as molecular magnets, as has been demonstrated in this thesis. In combining a highly tuneable molecular magnet with an oxidation sensitive nanocarrier, a highly customisable system has been developed that can be used in many imaging applications.

In chapter 2, we have explored the synthesis of PPS nanoparticles, showing that the improved synthesis method allows for a controlled size distribution ranging from 50 nm up to 160 nm. This was achieved by using a protected initiator reducing the formation of disulfides in the emulsion there by limiting chain transfer process, the factor that is believed to cause particle instability. Their oxidation upon exposure to both H_2O_2 and OCl^- has also been studied using various experimental techniques, in particular dynamic light scattering and diffusion ordered spectroscopy. It was found that exposure to high concentrations of H_2O_2 caused nanoparticle swelling after a long period of exposure (2-3 hrs) however exposure to OCl^- caused almost immediate swelling of the nanoparticles. The use of DOSY allowed us to understand the dynamics behind the oxidation process, showing that exposure to H_2O_2 caused the surfactant, Pluronic F-127, to desorb from the surface of the nanoparticles where as OCl^- oxidation induced the depolymerisation of the nanoparticles resulting in polymer fragments.

In chapter 3 we demonstrate that the PPS nanoparticles can be successfully loaded with Cr_7Ni heterometallic rings. The loading process showed to have little to no effect on the nanoparticles' or molecular magnets' chemical or physical properties. It was found that the loaded nanoparticles have an inherent relaxivity allowing them to be used in their own right as a T_2 contrast agent; however upon oxidation with small amounts of hydrogen peroxide, their effect on the transverse relaxivity of water protons is increased. The change in

relaxivity is independent of H_2O_2 concentration or exposure time and an effect was found at concentrations as low as 0.05 mM. This non-linear mechanism can be described as a binary 'off-on' switch with the ability to convert small quantities in H_2O_2 into a significant change in MR signal.

In chapter 4, we explore the effect of the molecular magnets' composition and carboxylate functionalization on their loading efficiency and effect on relaxivity. Molecular magnets with different functionalization (pivalic acid, 2-ethylhexanoic acid and 3,5-diisopropylsalicylic acid) as well as different metallic centres (Cr_7Ni and $Cr_{12}Gd_4$) were used. It was found that as the ligand increased in size, the molecular magnet's core was more protected against hydrolysis during loading however efficiency in changing relaxivity decreased. On the contrary, smaller ligands cause a greater initial uptake of water molecules during synthesis and therefore a reduced response upon oxidation however have an increased overall relaxivity. The presence of Gd, in the $Cr_{12}Gd_4$ compound clearly has a large effect on the particle's magnetic moment increasing its effect on the transverse relaxivity of water protons when compared to Cr_7Ni compounds.

There are many possible routes through which this project may be brought forward. Given the 'modular' nature of the project, one or more of the multiple components can be further studied in order to improve the performance or the functionality of the contrast agent.

In terms of the molecular magnet design and composition, it could be of interest to continue the study of alternative ligands that could improve the loading efficacy or water interaction. Although not mentioned in the scope of this thesis. An attempt was performed to use the diisopropylsalicylic acid functionalised molecular magnet as a T1 contrast agent. Due to the lack of complete water solubility of the compound, it was necessary to use a co-solvent mixture of THF and water, clearly not viable in clinical applications; however under these conditions the compound did have a large effect on T1 relaxivity. A measured r1 of 12 mM-1s-1 was obtained via NMR relaxivity measurements. This shows that if a ligand was designed with which the molecular magnets are soluble in water, they could be used in their own right as very effective contrast agents.

With regards to the nanocarrier, there are multiple ways in which it can be improved on. In a first instance, its oxidation response, although short (a few min), may not be viable in

clinical applications where a response in seconds would be needed. This is due to the circulation time and retention time, within a few minutes the oxidised particles could be somewhere else in the body and provide a false signal to the operator. In addition, the use of Pluronic F127 as a surfactant for the nanoparticles can enable surface functionalisation of said particles. Using specific targeting ligands such as peptides or antibodies, these can be linked on to the surface of the nanoparticles to allow for active targeting, instead of the current passive targeting. This could also avoid any issues with oxidation response, as the retention of the particles would be greater, hence a few minutes to provide a signal would be viable.

Finally, the next obvious step for this project is to perform some phantom imaging. Although not reported in this thesis, phantom imaging has been performed with more or less success. A clear signal was seen using the unoxidised nanoparticles, with a variation in signal with particle concentration. However, upon oxidation, almost no signal change was observed contrary to what was seen in the NMR experiments. Due to lack of time, this was not explored further, however some ideas as to why this was not seen could be: signal normalisation during image processing, different sensitivities between the MRI and NMR systems or maybe the difference in magnetic field used (NMR-9T/MRI-3T).

As a final note, although this system could not be used in clinical applications, it is a good starting point for an oxidation sensitive contrast agent. Demonstrating a relatively quick binary response to oxidative conditions as well as showing that the heterometallic wheels can be used to effectively alter contrast, both sides can be brought further together or independently.

6 Appendix – Polysulfide polymerisation

During the initial phase of this project, it was found that the synthesis of the polysulfide nanoparitcles was not uniform or reproducible. The synthesis regularly resulted in nanoparticles with broad or multimodal distributions proving that the size control was not at all present. In addition, the nanoparticle stability was almost non-existent. After a few weeks, the nanoaprticles would fall out of dispersion and aggregate at the bottom of the tubes. Due to the nature of the synthesis, there were only three possible 'failure' points of the process: the mechanical linking of the surfactant to the polymer chains, the episulfide polymerisation or the cross-linking step.

The mechanical entangling of the surfactant to the polymer chains is under kinetic control and starts almost immediately before the polymerisation begins. The hydrophobic polypropylene glycol groups orient themselves 'inside' the droplets and surround the monomer. Under mechanical stirring, these droplets collide and reform keeping a relatively uniform size. Once the polymerisation begins inside the droplets, the polymer chains will entangle with the hydrophobic PPG linking the surfactant to the surface of the particle. There is very little that could prevent this from happening.

The episulfide polymerisation is a robust process as it can be performed in an emulsion, however its weak point is the presence of oxygen. When oxygen is introduced into the system, it causes the formation of disulfides. These sulfur-sulfur bonds are able to easily exchange in a process called chain transfer. They are therefore very unstable and can compromise the integrity of the polymer matrix. In the case where disulfides are created during the initial steps of the polymerisation, this can lead to early termination of the polymer chains in the best of cases, or they can link multiple complete chains into long, unstable polymers. If, following the end of the polymerisation and after cross-linking, these long chains break apart in chain transfer, the once rigid nanoparticle is now a droplet. With the lack of mechanical stirring, the droplets can aggregate and eventually fall out of suspension. This is what we believed to be the root cause of the unstable dispersions.

During the polymerisation, care is taken to de-gas the water and work under inert conditions, however the problems still occurred. It was found that the case was a two part problem. The first step was to use a protected initiator; it was found that the dithiol initiator that was bought gradually formed disulfides in situ as it was being used and exposed to air. This introduced disulfides into the reaction. The solution was to use a protected initiator for storage and deprotect it under inert conditions immediately prior to use. It was also found that the deionised water that was being used had a very high conductivity caused by metallic impurities that were being released from a valve. Correcting these two issues resulted in the synthesis of nanoparticles with a uniform size distribution and an acceptable PDI.

The final failure point of the synthesis could have been in the cross-linking step. Had the polymerisation proceeded without the formation of disulfides and the particles were still unstable, a link could have been made to a non-uniform cross-linking. This however was ruled out. Although it is impossible to understand what is happening on the molecular level with the cross-linking and change in micro-viscosity, the cross-linking will start from the outside in. This will create a cross-linked corona around the nanoparticles preventing them from breaking apart. Although the centre of the nanoparticles will probably not be immediately cross-linked, this will occur over a period of time as the cross-linker diffuses further into the core. In addition, as the particles are not stored in inert conditions, disulfides could form in the core aiding in the cross-linking. The presence of these disulfides would not cause stability issues as discussed previously as the particles have already been partially cross-linked and have a rigid corona.